Summer 2017

Instrument Design Optimization with Computational Methods

Michael H. Moore
Old Dominion University

INSTRUMENT DESIGN OPTIMIZATION WITH COMPUTATIONAL

METHODS

by

Michael H. Moore
B.S. June 2010, Old Dominion University
M.S. June 2012, Old Dominion University

A Dissertation Submitted to the Faculty of
Old Dominion University in Partial Fulfillment of the
Requirements for the Degree of

DOCTOR OF PHILOSOPHY

PHYSICS

OLD DOMINION UNIVERSITY
August 2017

Approved by:

Silviu Covrig Dusa(Director)

Lawrence Weinstein (Member)

Rocco Schiavilla (Member)

Charles Hyde (Member)

Colin Britcher (Member)

ABSTRACT

INSTRUMENT DESIGN OPTIMIZATION WITH COMPUTATIONAL
METHODS

Michael H. Moore
Old Dominion University, 2017
Director: Dr. Silviu Covrig Dusa

Using Finite Element Analysis to approximate the solution of differential equations, two different instruments in experimental Hall C at the Thomas Jefferson National Accelerator Facility are analyzed. The time dependence of density fluctuations from the liquid hydrogen (LH2) target used in the Q_{weak} experiment (2011-2012) are studied with Computational Fluid Dynamics (CFD) and the simulation results compared to data from the experiment. The 2.5 kW liquid hydrogen target was the highest power LH2 target in the world and the first to be designed with CFD at Jefferson Lab. The first complete magnetic field simulation of the Super High Momentum Spectrometer (SHMS) is presented with a focus on primary electron beam deflection downstream of the target. The SHMS consists of a superconducting horizontal bending magnet (HB) and three superconducting quadrupole magnets. The HB allows particles scattered at an angle of 5.5° to the beam line to be steered into the quadrupole magnets which make up the optics of the spectrometer. Without mitigation, remnant fields from the SHMS may steer the unscattered beam outside of the acceptable envelope on the beam dump and limit beam operations at small scattering angles. A solution is proposed using optimal placement of a minimal amount of shielding iron around the beam line.

ACKNOWLEDGMENTS

I would like to thank Silviu Covrig Dusa for giving me the opportunity to work on these projects and mentoring me through my research. The Physics Department at ODU has been wonderful to work with and I would especially like to thank Lisa Okun, Charles Sukenik, and Lepsha Vuskovich for all their help with the formalities. From the beginning of my education here, Larry Weinstein has been both an inspiration and mentor and has my profound gratitude. Many people at JLab have been kind and helpful to me including Roger Carlini, Dave Mack, and Steve Wood. Scott Pilzer deserves many thanks for stoking my passion for physics when I barley knew what it was. Lastly and most importantly I would like to thank my wife, Katie Moore for unwavering support through this graduate school experience. I couldn't have done it without you.

TABLE OF CONTENTS

LIST OF TABLES

LIST OF FIGURES

CHAPTER 1

INTRODUCTION

Experimental nuclear physics is a field of study that requires sophisticated machinery. The theoretical underpinnings go back at least to the ancient Greeks. The dual ideas of analysis and synthesis led to the atomism philosophy of Leucippus and his pupil Democritus. According to atomism as defined by the ancients, nature consisted of only atoms and a void. They believed that if any matter could be divided enough times one would encounter the smallest building block which cannot be divided further. Nuclear physics in the modern sense began with Rutherford's scattering experiments in 1910 which led to his paper, "The Scattering of α and β rays by Matter and the Structure of the Atom" [1]. This experiment not only discovered the presence of a nucleus in atoms but also formed the template for future nuclear research. Scattering experiments of this sort are still employed to investigate the interior of atoms, nucleons and the Standard Model in general. Rutherford's experiment employed α particle energies of around 6 MeV and were used to make the first measurement of the sizes of nuclei. Today's scattering experiments can have much higher beam energies and are able to probe the quark and gluon distributions inside hadrons. These beam energies require multi-million dollar machines and extremely sensitive detectors.

The Thomas Jefferson National Accelerator Facility (JLab) is a U.S. Department of Energy (DOE) funded laboratory located in Newport News, VA. JLab's primary mission is to probe the nucleus of atoms using the Continuous Electron Beam Accelerator Facility (CEBAF). DOE provided funding for research, development and design of CEBAF in 1984, and construction began in February 1987. The first physics experiment using CEBAF began in 1995 using a 4 GeV electron beam. In 2000 CEBAF reached a milestone when the first 6 GeV beam was delivered to the three existing

experimental halls (A, B and C) [2]. Figure 1 shows an aerial view of JLab taken in 2016.

FIG. 1: Thomas Jefferson National Accelerator Facility (JLab) in 2016

The experimental equipment used at JLab can be broken down into three basic categories. First is CEBAF which accelerates electrons to the necessary energy. The primary component in the accelerator are superconducting niobium radio frequency cavities. Next is the fixed target where the electron beam is scattered. The targets can be liquid, solid or gas and are located in three experimental halls (Halls A, B, and C). Lastly, various detectors and spectrometers along with their electronics and data acquisition are used to determine the properties of out-coming particles from the collisions with the target.

As the experimental apparatus' become more complex and costly the design process becomes more important. The tools used in these experiments and their expected performance must be as well understood as possible before the expensive process of

building and commissioning can begin. Analytical methods are tedious or impossible with most of the machines needed for experimental nuclear physics. Simulations using numerical techniques are well suited to analyze proposed designs and can be used to improve them. Finite element analysis (FEA) is the tool of choice to simulate all three parts of JLab's nuclear experiment facility and will be discussed further in the next section. This dissertation is organized in two parts dealing with two of the three basic components in experimental Hall C. Part one is an analysis of the noise produced by a cryogenic target in Hall C in an effort to improve future target designs. Part two looks at the electron beam dynamics downstream of the target and the unintentional deflection caused by external magnetic fields produced by a new spectrometer and a mitigation proposal.

1.1 FINITE ELEMENT ANALYSIS

When confronting complicated geometries many analytical methods in physics become cumbersome or impossible to calculate. Numerical methods can be employed for these type of problems to achieve an approximation for physical parameters of interest. FEA is typically used in boundary value problems for partial differential equations when the number of equations is large and/or unsolvable using analytic methods. The basic idea is to take a continuous domain and break it up into smaller sub-domains or finite elements in which the governing equations are easier to solve individually. The governing equations in these finite elements are then discretized to create a series of simultaneous algebraic equations which can be represented as matrices to be solved using the techniques of linear algebra. Computers are excellent at solving systems of this sort and for this reason the growth of FEA has mirrored the growth in scientific computing.

Sub-dividing a domain into finite elements in modern FEA is called meshing. The meshing process is usually a part of the FEA solver application and is fine-tuned for whatever physical situation the solver was designed for. There are many parameters for the user to choose including the shape and size of the elements, the growth in size as a function of distance from boundaries, etc. The work contained in this dissertation

was done using two different commercially available software applications and further information on their meshing components will be found in sections 4.1 and 6.3.

The three most popular discretization methods in FEA are 1) Finite Element Method (FEM) 2) Finite Difference Method (FDM) and 3) Finite Volume Method (FVM) [3]. FEM and FVM will be discussed in detail in sections 4.1 and 6.3.

The history of FEA can be traced back to Lord Rayleigh and Walter Ritz at the end of the nineteenth century who pioneered work in numerical analysis and approximations for boundary value problems [4]. In the early twentieth century, Lewis Fry Richardson introduced point iterative schemes for numerically solving Laplace's equation to find the stress distribution in a masonry dam. Fifteen years later in an attempt to retroactively forecast the weather of a single day, Richardson approached meteorology by dividing the Earth's atmosphere into several layers of grid points and using initial conditions to solve for horizontal momentum, pressure, humidity and temperature. It took him two years to calculate the equations for a section of central Europe and the endeavor was a failure [5].

Numerical analysis began in the modern sense in 1928 with a paper by Courant, Friedrichs, and Lewy (giving us the acronym CFL) [6]. Uniqueness and existence questions were addressed in this paper as well as being the source of the CFL stability requirement for the numerical solution of hyperbolic partial differential equations.

1.2 COMPUTATIONAL FLUID DYNAMICS (CFD)

In 1940, Allen and Southwell's paper, "Relaxation Methods Applied To Determine The Motion, In Two Dimensions, Of A Viscous Fluid Past A Fixed Cylinder" introduced a relaxation scheme for iterative solving of systems of equations that has been extensively used in fluid dynamics as well as in structural problems [7]. The relaxation method was tailored to hand calculations and added to the growing list of solved viscous flow solutions which had begun in the 1930's.

The birth of modern CFD occurred in 1965 when an article in Scientific American by F. Harlow and J. Fromm proposed "in-silico" (computer) experiments. They stated, "The fundamental behavior of fluids has traditionally been studied in tanks

and wind tunnels. The capacities of the modern computer make it possible to do subtler experiments on the computer alone" [8].

An important step in the story of CFD occurred in the early seventies, when Brian Spalding and Suhas Patankar developed the Semi-Implicit Method for Pressure Linked Equations (SIMPLE) [9]. This algorithm is still being used today and will be discussed in greater detail in section 4.2.

Brian Spalding went on to found Concentration Heat And Momentum Limited, (CHAM) in 1974 and developed the first commercially-available general-purpose CFD code in 1981. The software was called the Parabolic Hyperbolic or Elliptic Numerical Integration Code Series (PHOENICS) [10]. The company is still operating and is being led by its founder in London, England. The availability of these codes removed the need of writing specific programs for each CFD calculation. In the 2000's two of the leading software developers for CFD code, CFX and Fluent, were bought out by Ansys, Inc [11]. The addition of CFX and Fluent made Ansys the biggest player in the CFD market.

1.2.1 DISCRETIZATION EXAMPLE

For any numerical approximation using finite element analysis, the governing equations must be solved in many small control volumes. There are three expectations of this discretization for fluid dynamics. The first is conservation. If the physical problem involves the conservation of a quantity, the discretized form of the governing equations should reflect this conservation. This is true for the individual control volumes as well as the entire domain. The second expectation is that the problem is bounded. For a given physical problem the initial conditions and boundary conditions place bounds on the possible solutions. This should be reflected in the discretized form of the governing equations. The third expectation for discretization in CFD is transportation of fluid properties in the direction of fluid flow [12].

The finite volume method is the method of choice over FEA and FDM in CFD because it includes conservation in the discretization process. The three basic steps in FVM are [13]

- Divide domain into a number of finite sized control volumes (sub-domains). Also called meshing.

- Integrate governing differential equation(s) over each sub-domain.

- Use a profile assumption (interpolation function) for the dependent variable(s) for evaluating integrals.

As a simple example a one dimensional steady state heat conduction problem will be discretized using these steps. The governing equation for the temperature(T) in a rod of material of length L, thermal conductivity k, and heat source S is

$$\frac{d}{dx}\left(k\frac{dT}{dx}\right) + S = 0 \tag{1}$$

A diagram of the problem is shown in Figure 2. The domain will be divided up
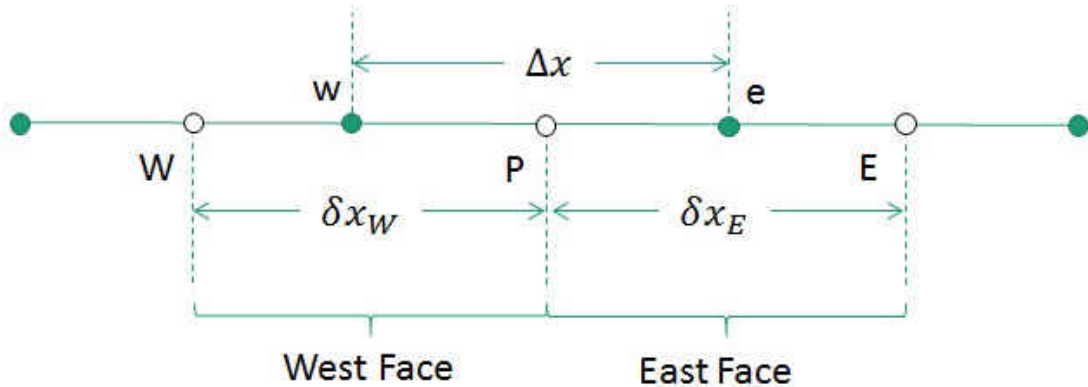
FIG. 2: One dimensional rod discretized into three equal segments

into three sub-domains. The first step in meshing is defining the control volumes by picking grid points (W, P and E). P is the grid point of interest in this example. W and E stand for points that lie west and east of our control point P. In a two dimensional problem there would also be N (north) and S (south) points neighboring P as well. By making the grid points equally spaced this mesh is called a structured mesh. In general this will not be the case and the mesh is then called unstructured. Defining the control volumes in a one dimensional case is carried out by picking points between the grid points and calling them faces. Faces are denoted by lowercase w

and e. In the three dimensional case these would be true faces of volume elements (see Figure 3). In two dimensions faces are defined as the sides of the cell. The next
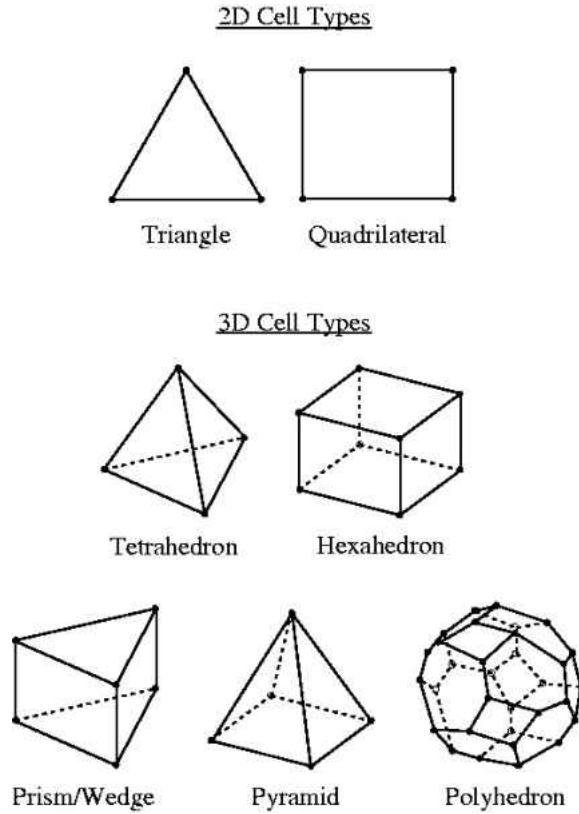
FIG. 3: Cell types in two and three dimensions

step is to integrate the governing equations over each control volume. For control volume P,

$$\int_w^e \frac{d}{dx}\left(k\frac{dT}{dx}\right) dx + \int_w^e Sdx = 0 \tag{2}$$

$$k\frac{dT}{dx}\bigg|_e - k\frac{dT}{dx}\bigg|_w + S\Delta x = 0 \tag{3}$$

In the third step a profile assumption is used to find the solutions to the governing DE at the faces. Since the solutions from one control volume will be matched to its nearest neighbors, the profile assumption must be continuous on the faces. First and second order functions are the standard choices. If a higher order interpolation is needed, it means that the control volumes are too large and the mesh needs to

be redrawn with smaller control volumes. In this example only a first order approximation (Figure 4) is possible. This is because a second order profile assumption requires the values at two adjacent cells on either side of cell P. Five cells would be necessary for this [13] (see Figure 5). For a first order interpolation, the solutions
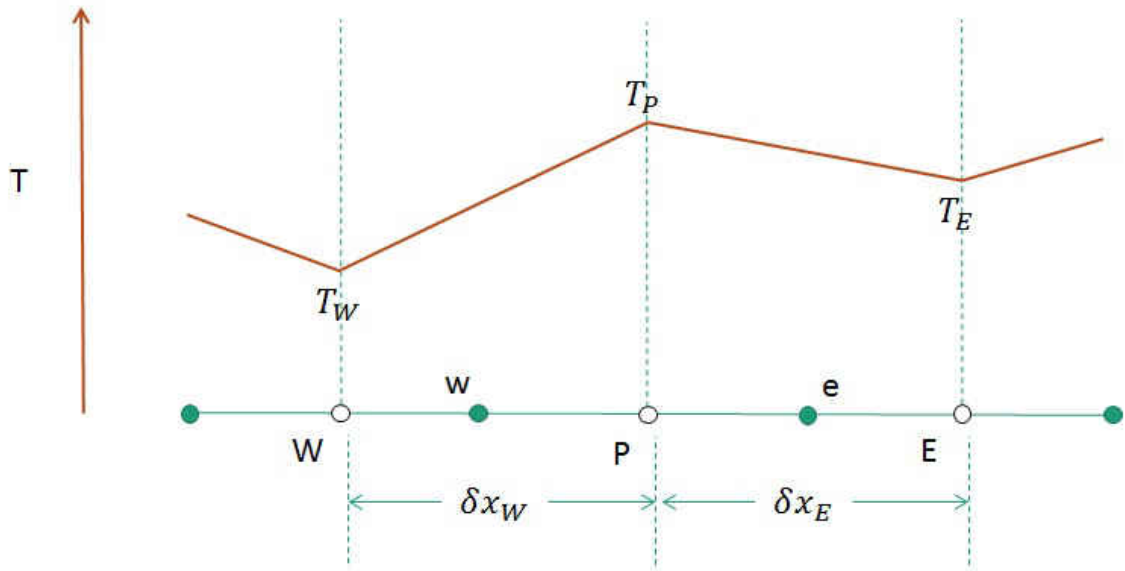
FIG. 4: First order profile assumption. Temperature (T) is represented in red and varies linearly between control element centroids.

at each control volume centroid are assumed to vary linearly to the nearest neighbor. For the sake of generality, the thermal conductivity will be allowed to vary between control volumes. From Figure 2 it can be seen that Equation 3 can be rewritten as

$$k_e \frac{T_E - T_P}{\delta x_e} - k_w \frac{T_P - T_W}{\delta x_w} + S\Delta x = 0 \tag{4}$$

$$\left(\frac{k_e}{\delta x_e} + \frac{k_w}{\delta x_w} \right) T_P = \frac{k_e}{\delta x_e} T_E + \frac{k_w}{\delta x_w} T_W + S\Delta x \tag{5}$$

By taking

$$a_E = \frac{k_e}{\delta x_e}, a_W = +\frac{k_w}{\delta x_w}, a_P = \frac{k_e}{\delta x_e} + \frac{k_w}{\delta x_w}, b = S\Delta x \tag{6}$$

the discretized form of the governing DE is then

$$a_P T_p = a_E T_E + a_W T_W + b \tag{7}$$
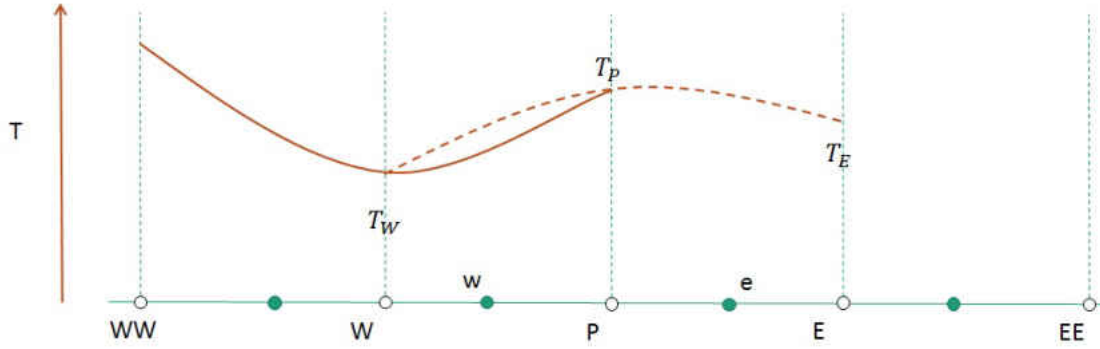
FIG. 5: Second order profile assumption. The temperature (in red) has a second order profile requiring the use of four cells adjacent to the cell of interest.

If the point P is labeled i with i being consecutive numbering of control volumes, then

$$a_i T_i = a_{i+1} T_{1+1} + a_{i-1} T_{i-1} + b \tag{8}$$

At this point the governing DE is an algebraic equation and the values of T at each element can be solved iteratively depending on its adjacent cells values.

CHAPTER 2

THE QWEAK EXPERIMENT AND LH2 DENSITY

FLUCTUATIONS

The Q_{weak} experiment sought, for the first time, to measure the weak charge of the proton using parity-violating electron scattering from protons at low four momentum transfer squared $(Q^2 = 0.025\,\mathrm{GeV}^2/\mathrm{c}^2)$. This was accomplished by scattering longitudinally polarized electrons of opposite helicity states off an unpolarized liquid hydrogen (LH2) target and measuring the asymmetries of elastically scattered electrons. The parity-violating asymmetry in cross sections is defined as

$$A_{PV} = \frac{\sigma_+ - \sigma_-}{\sigma_+ + \sigma_-} \tag{9}$$

where the subscripts $+(-)$ correspond to positive and negative helicity states of the electrons. A_{PV} is linear with respect to the weak charge of the proton. In the forward angle limit, [14]

$$\frac{A_{pv}}{A_0} = Q_W^p + Q^2 F^p(Q^2, \theta) \tag{10}$$

where $A_0 = -G_F Q^2/4\pi\alpha\sqrt{2}$, G_F is the Fermi constant, and α is the fine structure constant. $Q^2 F^p$ carries the nucleon structure in terms of electromagnetic, neutral-weak, and axial form factors. By measuring the $\vec{e}p$ asymmetry at small Q^2, Qweak sought to find Q_W^p, the weak charge of the proton [15]. The expected asymmetry from the standard model is only 230 ppb and the proposed goal of a 2.5% measurement meant that the overall uncertainty for the experiment needed to be on the order of 6 ppb. The precision necessary for this measurement required many improvements to JLab's CEBAF and Hall C. These improvements will be discussed in later sections.

In order to suppress systematic effects due to density changes in the LH2, the electron beam was helicity flipped at a rate of 960 Hz. The beam spent ≈ 1 ms in

each helicity state. Each of these time periods (minus the "dead-time"; see section 3.1) was delineated by the Macro Pulse Signal (MPS) which coordinated the timing of the electronics in the experiment to the helicity flipping rate. The term MPS is used to define one helicity window and each MPS is assigned a plus or minus sign to indicate the helicity state of the beam in that window [16].

Quantity	Value
Beam energy	1.16 GeV
Beam polarization	89%
Beam current	180 μA
Luminosity	$1.7 \times 10^{39} \, \text{cm}^{-2} \, \text{s}^{-1}$
θ acceptance	$5.8° - 11.6°$
ϕ acceptance	49% of 2π
Q^2	0.025 GeV^2
Helicity reversal frequency	960 Hz
Detector rate	7 Ghz

TABLE 1: A summary of typical parameters for Run 2 of the Qweak experiment

Commissioning of the Qweak experiment started in 2010. After a commissioning run, there were two data taking runs. Run 1 was from February to May 2011 and Run 2 was from November 2011 to May 2012. The six months between them were a scheduled accelerator down period. Fortunately for the Qweak experiment, some improvements were then made from the experience with Run 1. Some of these will be discussed in the following sections.

Density changes in the LH2 produce two systematic effects in the Qweak experiment. One is a change in the average density of the fluid ($\Delta\rho/\rho_0$) in the interaction region. This has the effect of reducing the effective target length by decreasing the number of LH2 molecules that interact with the electron beam. The other effect is a time dependent fluctuation in the density of the target [17]. These are particularly important for parity violation experiments such as Qweak where the helicity of the beam is flipped at 960 Hz (every 1.04 ms) [16]. The scattering rate over each one of these helicity cycles is sensitive to changes in density on this timescale. The cause of these fluctuations is thus far unknown. There is speculation about the LH2 boiling at the windows being the cause. This could be either bubbles forming on the aluminum

windows or a thin film of gaseous LH2 existing between the aluminum and the LH2. The motivation for the following analysis was to see if the LH2 density fluctuations at various timescales can be predicted with CFD simulations. If CFD can predict the density fluctuations, then the future designing of cryogenic liquid targets can take this into account and minimize the noise due to density fluctuations through simulations.

2.1 CONTINUOUS ELECTRON BEAM ACCELERATOR FACILITY(CEBAF)

CEBAF is a re-circulating linear accelerator which uses 330 superconducting radio frequency (SRF) niobium cavities to accelerate electrons. These cavities are submersed in a 2 K liquid helium bath and operate at a frequency of 1497 MHz. The SRF cavities are located in two parallel LINACs (Linear Accelerators) connected by two recirculating arcs which allow the beam to make one to five passes through the LINACS. Polarized electrons are produced by photo production and then travel through superconducting niobium cavities that accelerate them to the desired energy. At the time of the Qweak experiment the maximum obtainable energy was 6 GeV. Qweak had a nominal energy of 1.165 GeV which was acquired by one pass through the LINACs [18].

The source of polarized electrons in CEBAF is the photo production of electrons on strained-superlattice gallium arsenide (GaAs) by a circularly polarized laser. GaAS normally has a positive electron affinity. By treating the surface with cesium and oxygen, the surface has a negative electron affinity. By growing a layer of GaAsP, which has a different lattice constant, between two layers of GaAs mechanical strain is put on the GaAs layers because of lattice mismatch. The strained-superlattice GaAs increased electron polarization by more than 10% from the typical strained GaAs (from 75% to > 85%) and resulted in a quantum efficiency (the probability of electron emission per photon) of 0.8%.

A resistive copper cavity then accelerates the beam from 130 keV to 500 keV and SRF cavities further accelerate the beam to 62 MeV. The beam is then injected into
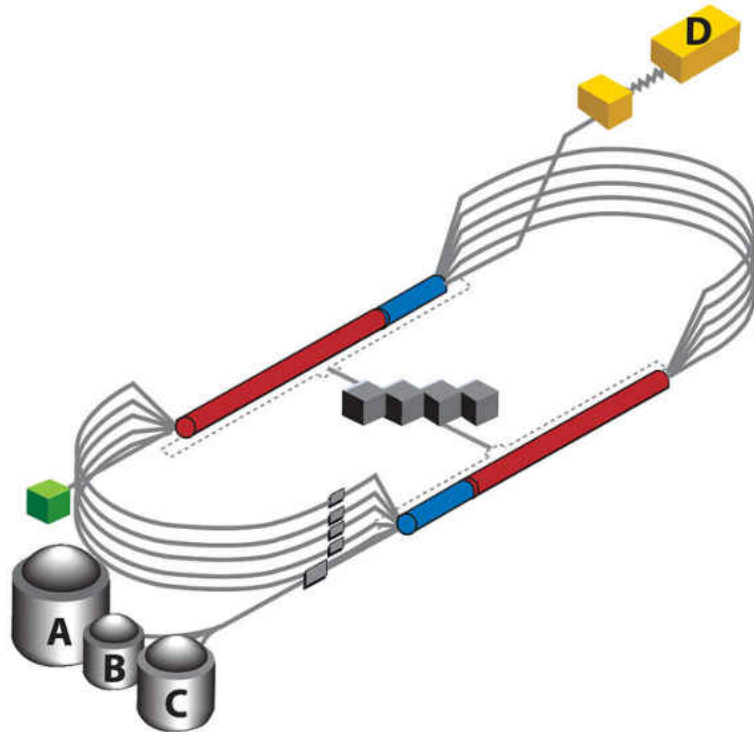
FIG. 6: Diagram of the Continuous Electron Beam Accelerator Facility (CEBAF) in its 12 GeV configuration. Visible are the four experimental halls – A, B, C and the newly added D – and the 10 new cryomodules (blue) added to the existing 40 modules (red). The gray blocks in the center represent the accelerator's refrigeration plant, and the green block indicates the injector.

the North LINAC where it travels one pass and is then steered into Hall C. This is only a basic description of CEBAF. For a more details on CEBAF see [18].

FIG. 7: New cryomodules partially installed in one of the LINACS in CEBAF. Ten cryomodules have been added to CEBAF at Jefferson Lab as part of the 12 GeV Upgrade project. Combined with the existing linear accelerators, they will double the energy of CEBAF's electron beam – from 6 GeV to 12 GeV.

2.1.1 BEAM CURRENT MONITORS

Six cavity type BCMs were installed in the beamline to provide linear, precise, and low noise measurements of the beam charge incident at the target. The BCM's are cylindrical stainless steel cavities used in resonant TM 010 mode at 1497 MHz such that the signal output of the cavity is proportional to the beam current in the cavity. They were maintained at 110° F. BCM 1 & 2 used analog receivers while the other 4 BCMs utilized digital receivers which had improved digital signal processing utilizing 18-bit, 1 MHz DAC's to generate the output voltage. These were only used in run 2. The BCMs were calibrated against a Parametric Current Transformer

FIG. 8: Qweak apparatus before shielding

device [19] called the Unser monitor for the beam currents in the range of 1-180 μA. For low beam current measurements (10 nA - 1 μA) a Faraday cup was used. The Unser monitor offset is subject to slow drifts, and can not be used continuously for normalization whereas the Faraday cup can only be used invasively while stopping beam to the other Halls. The Unser monitor was calibrated for absolute current measurements before the experiment and the BCMs were calibrated periodically with the Unser during the experiment. During a BCM calibration, the beam was ramped up in steps of $20\mu A$ from zero with a beam off period in between. Each beam on and off period lasted about 1.5 minutes. The beam off periods provided the linear offset of the Unser monitor and the beam on periods gave the slope of the BCM response vs. the Unser response.

During the down time between Runs 1 and 2, upgrades were made to the BCM's. In Run 1, there were only six BCM's and the digital receivers for BCM's 5 and 6

sustained radiation damage. Between the runs, BCM's 7 and 8 were installed and new digital receivers for 5 and 6 were installed outside of the experimental hall [20].

2.2 BEAM RASTER

The final stage of beam transport and conditioning is a set of raster magnets. The purpose of the beam raster is to reduce the effects of target boiling and lower the maximum temperature of the aluminum target windows. This was accomplished by tracing the nominally $\approx 200\mu$m beam profile through a uniform square Lissajous pattern. Two air-core magnets were used for this, each driven by triangular waves with frequencies of $\nu_1 = 24.960$ and $\nu_2 = 25.920$ kHz. The difference between these two frequencies is the frequency of the entire raster pattern, $\nu_2 - \nu_1 = 960$ Hz to match the helicity flip rate and assure that nearly one complete Lissajous pattern was completed per MPS [21].
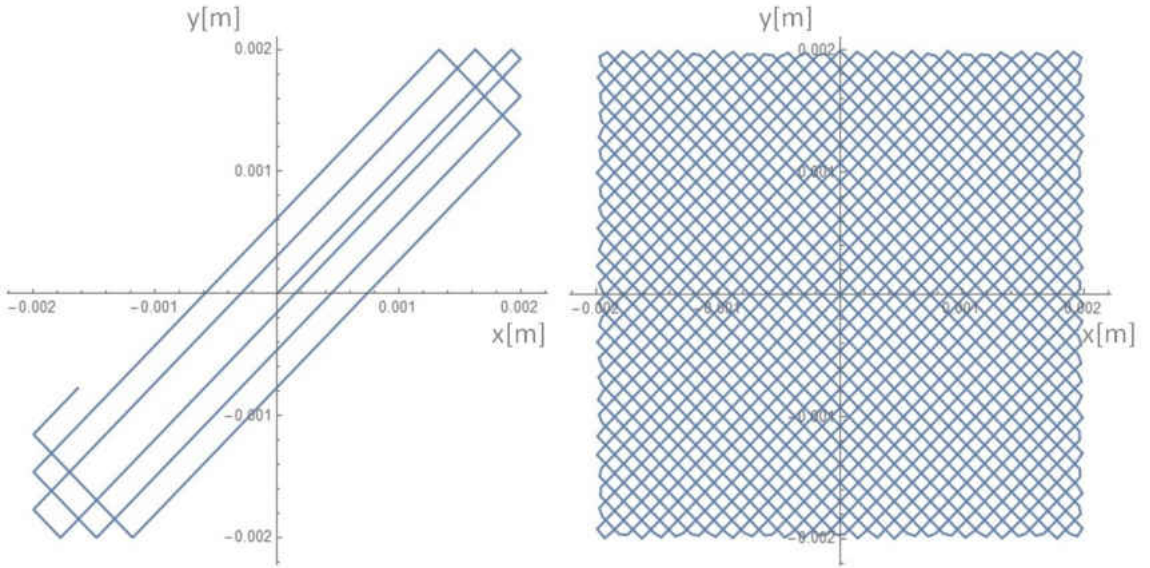
FIG. 9: The Lissajous pattern modeled with Mathematica. The left shows an incomplete pattern. The beam starts at the origin and traces the path indicated by the blue line. On the right is one complete pattern.

2.3 TARGET LOOP

The closed-loop liquid hydrogen (LH2) target used in Qweak had four main components which can be seen in Figure 10. These were a pump used to circulate the LH2, a heat exchanger to liquefy the H_2 and to remove the heat deposited by the electron beam, a heater to regulate the temperature and to replace the beam power when the beam was not on-target, and a target cell where the interactions with the beam took place. The volume of H_2 in the loop was $\sim$ 58 liters, and it was nominally at 20 K and 35 psia. It took about four seconds for the LH2 to make one circulation around the loop with a mass flow rate $\sim$ 1.1 kg/s. See Figure 2 for a list of LH2 properties in the Qweak target. Everything in the target loop except the cell was wrapped in twenty five layers of super-insulation to minimize radiative heat transfer. Temperature sensors were located at the inlet manifold, pump outlet, heater inlet, heater outlet and outlet manifold to monitor the LH2 temperature with an accuracy of 0.016 K. A remotely controlled two axis motion system was used to position the target relative to the electron beam. The target had a range of motion of 600 mm vertically and 86 mm horizontally [22].

Property	Nominal Conditions	Saturation liquid	Saturation Gas
Density,ρ [kg/m³]ρ	71.46	66.62	2.91
Thermal Conductivity, κ [W/m-K]	0.1043	0.1052	0.02121
Molecular Viscosity, ν [μPa-s]	13.925	10.63	1.30
Specific Heat, C_p [J/kg-K]	9527	12060	13810

TABLE 2: LH2 properties in Fluent at 35 psia sampled at the Qweak target inlet. The temperature of the LH2 at the inlet is 20 K. The saturation temperature of LH2 in these conditions is 23.7 K. If the density of the LH2 drops by $\sim$ 7% it may boil.

The total heat load in the LH2 was dominated by the beam deposited power. With a beam current of $I = 180\mu$A and a target length of $l = 34.5$ cm, the power transferred to the LH2 by the electron beam is

$$P = I \rho \, l \frac{dE}{dx} \tag{11}$$
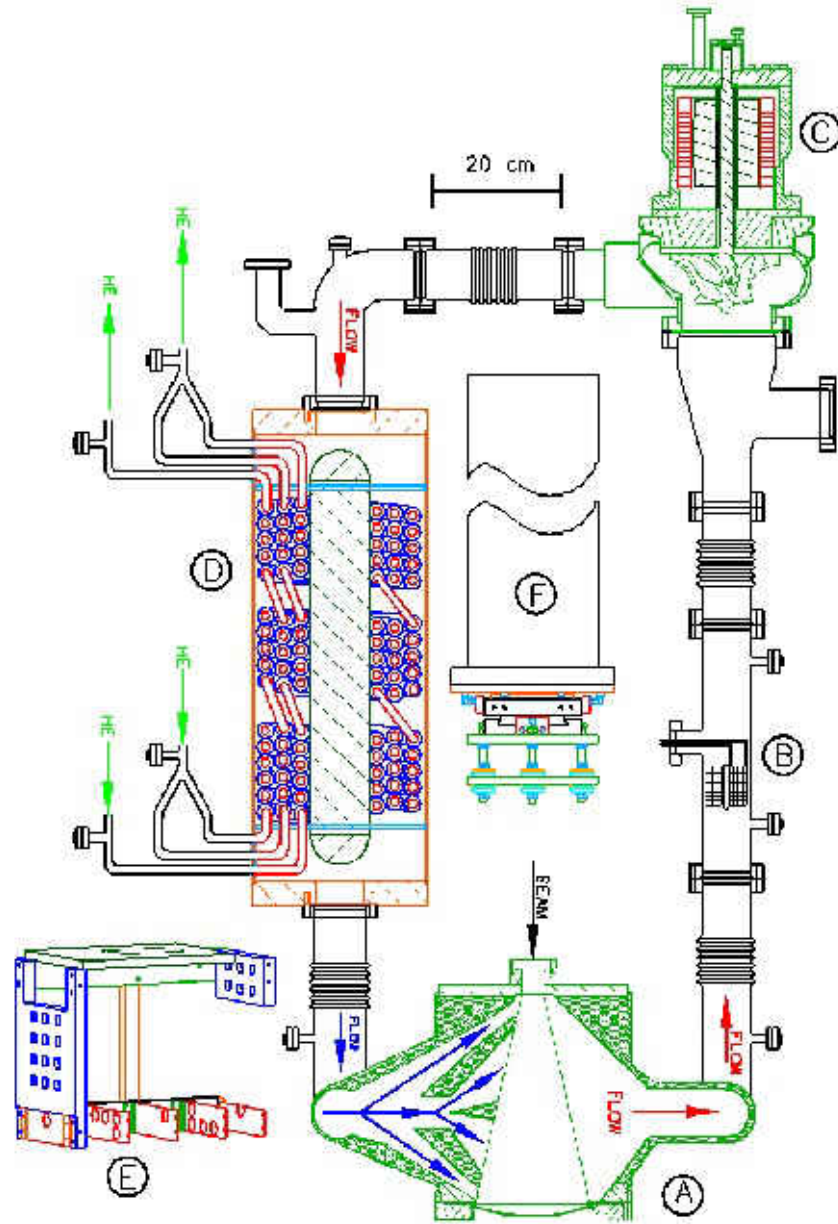
FIG. 10: Components of Qweak target. A: The target cell (pitched 90° to illustrate the flow pattern), B: the heater, C: the centrifugal re-circulation pump, D: the hybrid heat exchanger, E: the solid target ladder, which was mounted directly below the cell, and F: the long thin stainless steel pipe which mechanically supported the loop, as well as the manual cell adjustment mechanism at its lower end [23]

.

Length	34.5 cm
Al window thickness-beam in	0.1 mm
Al window thickness-beam out	0.127 mm
Temperature of LH2 at inlet	20 K
Mass flow of LH2	1 kg/s
Pressure	35 psia
Pressure drop through target cell	0.25 psid
Raster size	4×4 mm

TABLE 3: Qweak Target Nominal Parameters

For LH2, $\rho = 0.0723$ g/cm^3 and $dE/dx = 4.653$ MeV cm^2/g, and the power deposited into the LH2 by the beam is $P = 2140$ W. There is an additional energy loss from Bremsstrahlung radiation of 46 MeV but this does not contribute to heating the LH2. Several other heat loads in the LH2 are listed in Table 4. With a total heat load of ~ 3 kW, the Qweak target was the highest power cryotarget in the world at the time of this writing [23].

Heat Source	Power deposited (W)
e^- Beam in LH2	2140
e^- Beam in Cell Windows	25
Viscous Heating	177
Radiative Losses	150
Pump Motor	150
Reserve Heater Power	260
Total	2902

TABLE 4: Contributions to the heat load in the LH2 loop [23]. Only the first two are important for modeling and simulating the target and the values given here are for the nominal beam current (180 μA).

The cooling power required for the ~ 3 kW heat load on the LH2 was supplied by liquid helium from JLab's Central Helium Liquefier (CHL) and gaseous helium from the End Station Refrigerator (ESR). In the following sections, several components of the target loop will be described. A more detailed description of the target cell can be found in the next chapter (CFD with Fluent).

2.3.1 HYBRID HEAT EXCHANGER

The heat exchanger liquefied the gaseous hydrogen and maintained the loop temperature at 20 K at 31 to 35 psia by transferring heat from the LH2 to three separate liquid helium coolant circuits. The heat exchanger was designed at JLab and CFD was used to assure that the LH2 does not freeze. The flow rates of the coolants through the heat exchanger were optimized to take 1.2 kW of the total cooling power from helium at 15 K and 12 atm (from the ESR) while the rest of the cooling came from helium at 4 K and 3 atm (from the CHL). This allowed the heat exchanger to maintain the loop temperature without freezing the LH2 (at 13.8 K). A diagram can be seen in Figure 11.
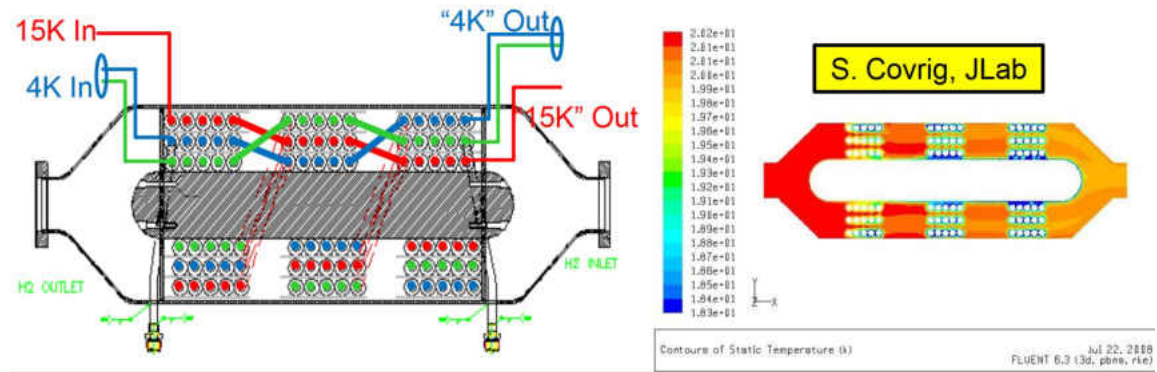
FIG. 11: Left: Diagram of the hybrid heat exchanger showing all three coolant lines. Right: CFD temperature map of the hybrid heat exchanger. The LH2 flow in both pictures is from right to left.

The heat exchanger consisted of three coolant circuits with three layers. Two of these circuits were 4 K (CHL) and one was 15 K (ESR). These finned copper tubes were wound on a cylindrical aluminum mandrel to force the hydrogen to flow through the coils. The differential pressure drop across the heat exchanger was 0.22 psi with a mass flow rate for 20 K LH2 of 1.08 kg/s [20].

2.3.2 HIGH POWER HEATER

In order to maintain the loop temperature of 20.00±0.02 K at all times even when the beam was not interacting with the LH2, a 3 kW capacity CFD designed resistive heater was added to the loop (see Figure 12). The heater used resistive

wire (13 AWG Nichrome) to provide up to 2500 W of power (Q) without boiling the LH2. This was very important for maintaining the loop temperature during beam trips [23].

FIG. 12: The high power heater before installation

2.4 TARGET CELL

The design of the Qweak target was led by Silviu Covrig Dusa. With nominal parameters, the required performance of the experiment required the smallest absolute precision ever achieved in a PVES measurement from a cryogenic target that had the highest beam current and power deposition to date. A unique design was called for and by using CFD the target achieved all the necessary milestones. The central LH2 volume was a flared conical section made of AL 2219 with the entrance window on the small end and the exit window on the large end (see Figure 13). The windows were made of AL 7075-T6 and machined as thin as structurally possible to minimize electron interaction with the aluminum. The entrance window was flat (normal to the beam axis) while the exit window was on the curved large end of the
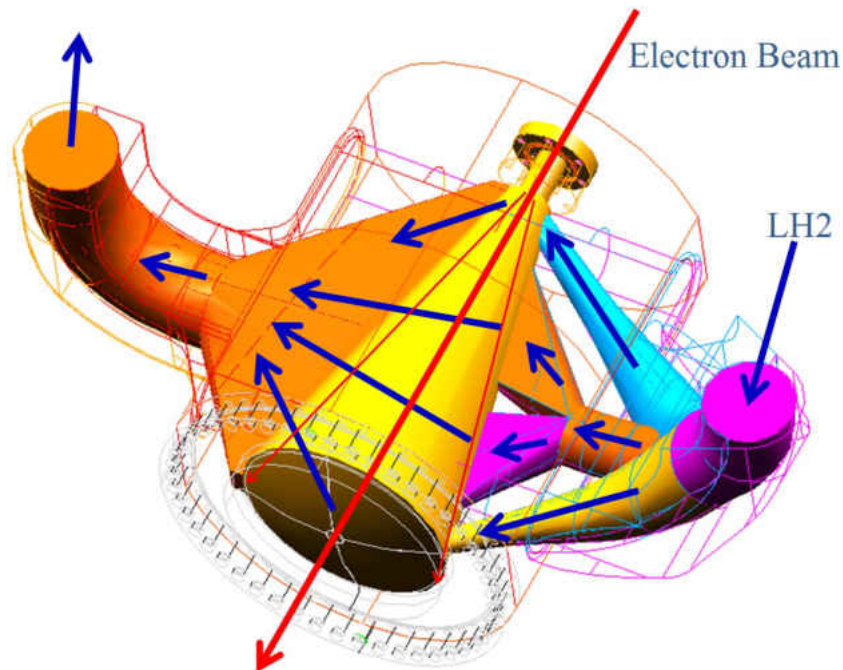
FIG. 13: Diagram of the Qweak target. The red line indicates the electron beam which travels through the center of the cell. The blue lines show roughly the flow of LH2. The cell block is shown in faint outline.

conical section. The entrance window was 22.2 mm diameter and 0.097 mm thick. The exit window had a larger diameter to admit all electrons scattered at or below 14°. This comfortably includes the experiment's $5.8° < \theta < 11.6°$ acceptance. The spherical exit window was 0.64 mm thick and 305 mm in diameter with a 254 mm radius of curvature (see Figure 14). The center of the exit window had a thin spot 15 mm in diameter and 0.125 mm thick to pass the unscattered beam. After correction for thermal contraction and pressure expansion the LH2 thickness between the aluminum entrance and exit windows was 343.6 mm.

The most unique feature of the Qweak target design was the segmented inlet and outlet manifolds. On the inlet side, the LH2 is diverted into three paths. The two outside paths are directed to the entrance and exit windows to impede boiling. The center path is further diverted into two and directed at the beam interaction region in the center of the target cell. The LH2 enters the cell with a mass flow rate of 1 kg/s. The inlet pipe just before the inlet manifold has a radius of 3.81 cm and an

Beam out Window
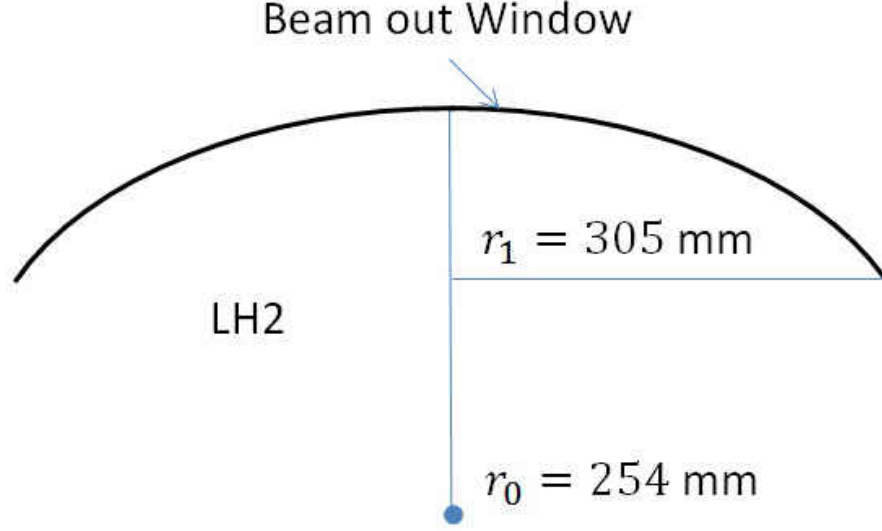
FIG. 14: The curvature of the beam exit window. This is not drawn to scale. The interior of the target is the bottom of the diagram, and the beam exits the target going upwards. r_o is the radius of window curvature and r_1 is the radius of the window.

area of 45.6 cm^2. This corresponds to an average flow velocity of 3 m/s at the inlet. The inlet manifold forces the LH2 across the windows at around 7.5 m/s.

An adiabatic approximation can be used to determine the temperature rise during the time it takes for the LH2 to traverse the beam and estimate $\Delta\rho/\rho_0$. Ignoring the beam motion, the beam is assumed to be stationary while the LH2 has a velocity perpendicular to the beam. The specific heat of LH2 is

$$C_p = \frac{Q}{\Delta T M} = 9.53 \left[\frac{\text{J}}{\text{gK}}\right] \tag{12}$$

where M is the total mass of LH2 inside the beam trajectory boundary and Q is the total energy deposited by the electron beam along the trajectory.

$$M = d^2 L \rho \tag{13}$$

$$Q = \Delta P \Delta t, \quad \Delta P = \rho \frac{dE}{dx} L I \tag{14}$$

where $d = 0.01$ cm is the beam transverse dimension, $L = 34.4$ cm is the length of
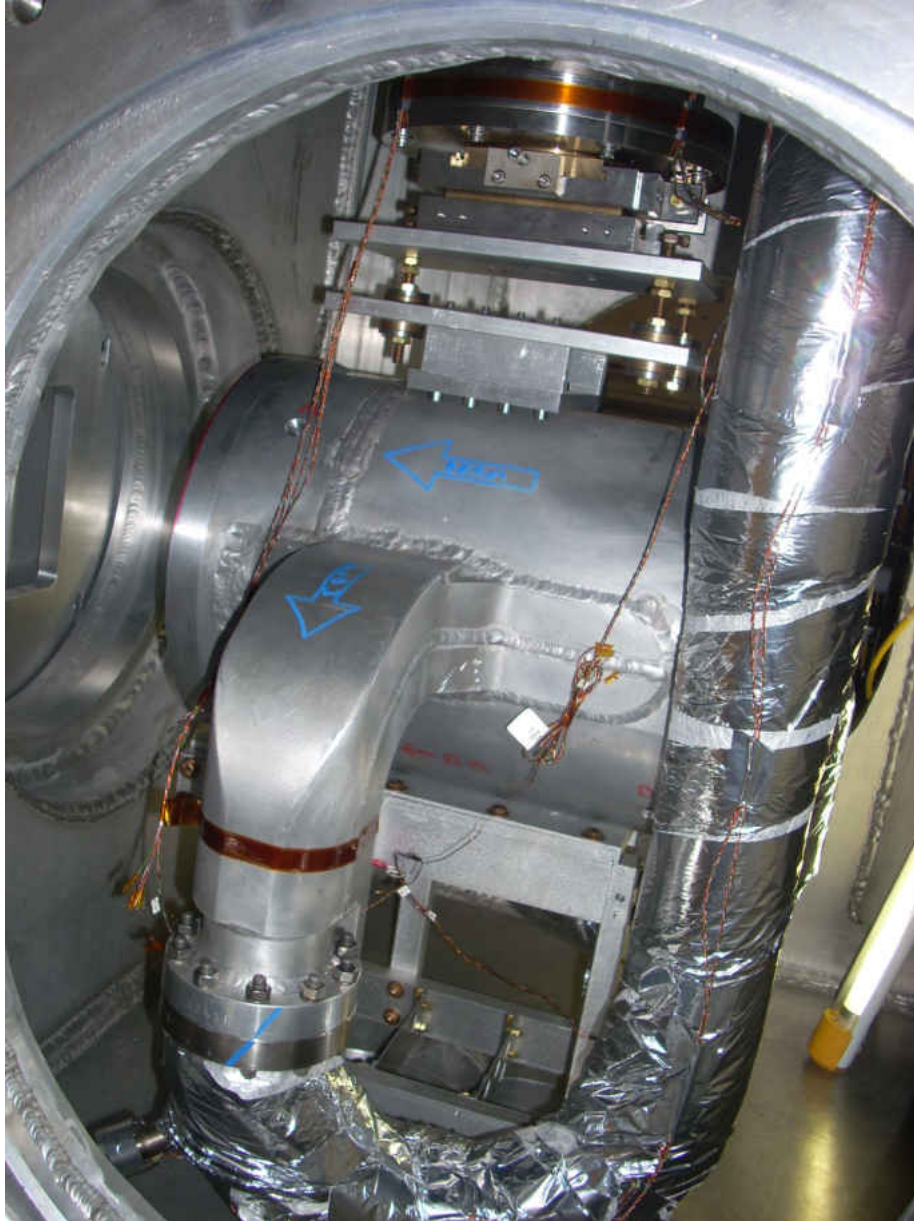
FIG. 15: Qweak LH2 target cell installed in the vacuum chamber. The solid target ladder can be seen directly underneath the LH2 target.

the target, and $\rho = 0.07 \,\frac{\text{g}}{\text{cm}^3}$ is the density of LH2. ΔP is the deposited beam power, $\frac{dE}{dz} = 4.63 \frac{\text{MeV}}{\text{g/cm}^2}$ is the beam energy loss in LH2 with a beam energy of 1.16 GeV [24]. $\Delta t = \frac{d}{v_l}$ is the time it takes for the LH2 to traverse the beam when the LH2 has a velocity v_l. The average velocity is calculated from the mass flow at the inlet of the Qweak target, $\dot{m} = 1 \,\text{kg/s}$ [25]. The inlet is circular with a radius of 3.81 cm which corresponds to an inlet area of $A_{inlet} = 45.6 \,\text{cm}^2$ (See section 2.4). The linear velocity of the fluid may be approximated as

$$v_l = \frac{\dot{m}}{\rho A_{inlet}} \approx 300 \,\frac{\text{cm}}{\text{s}} \tag{15}$$

$$\Delta T = \frac{\frac{dE}{dz} I}{d C_p v_l} \tag{16}$$

To express ΔT as a percent change in density we use

$$\rho = \frac{\rho_0}{1 + \alpha \Delta T} \tag{17}$$

$$\frac{\rho}{\rho_0} - 1 = \frac{1}{1 + \alpha \Delta T} - 1 \tag{18}$$

$$\frac{\Delta \rho}{\rho_0} = \frac{-\alpha \Delta T}{1 + \alpha \Delta T} \tag{19}$$

where $\alpha \approx 1/T$ is the thermal expansion coefficient of LH2 [26].

$$\frac{\Delta \rho}{\rho_0} \approx - \left(1 + \frac{T d C_p v_l}{\frac{dE}{dz} I} \right)^{-1} = 0.6\% \tag{20}$$

This is close to $\Delta \rho / \rho_0 \approx 0.8\%$, the value reported from Qweak. This model does not take into account two contributions to the average density change that surely have an effect. The first is the heating at the windows. As will be seen later, the temperature of the aluminum at the beam entrance and exit windows reached between 60 and 70 K [17]. Film boiling cannot be ruled out at these temperatures and the target was designed with this in mind. The inlet side of the target has a flow diverter that forces the velocity of the fluid to be higher at the windows. This will be discussed more in

section 2.4. The second contribution that was not taken into account in this model is the distribution of heat in the fluid volume. After passing through the beam spot in this model, no information about where the fluid goes is included. Neither is heating of the surrounding fluid included.

2.5 SOLID TARGETS

Solid targets were positioned in a three level two dimensional ladder array directly underneath the LH2 target cell mounted in such a way that good thermal contact is established between the ladder array and the bottom of the LH2 target. The targets in the two top layers were 2.5 cm^2 while the lower layer contained various combinations of foils at five positions along the beam axis (see Figure 16). The top row had an upstream and downstream section located directly underneath the LH2 target windows [20].
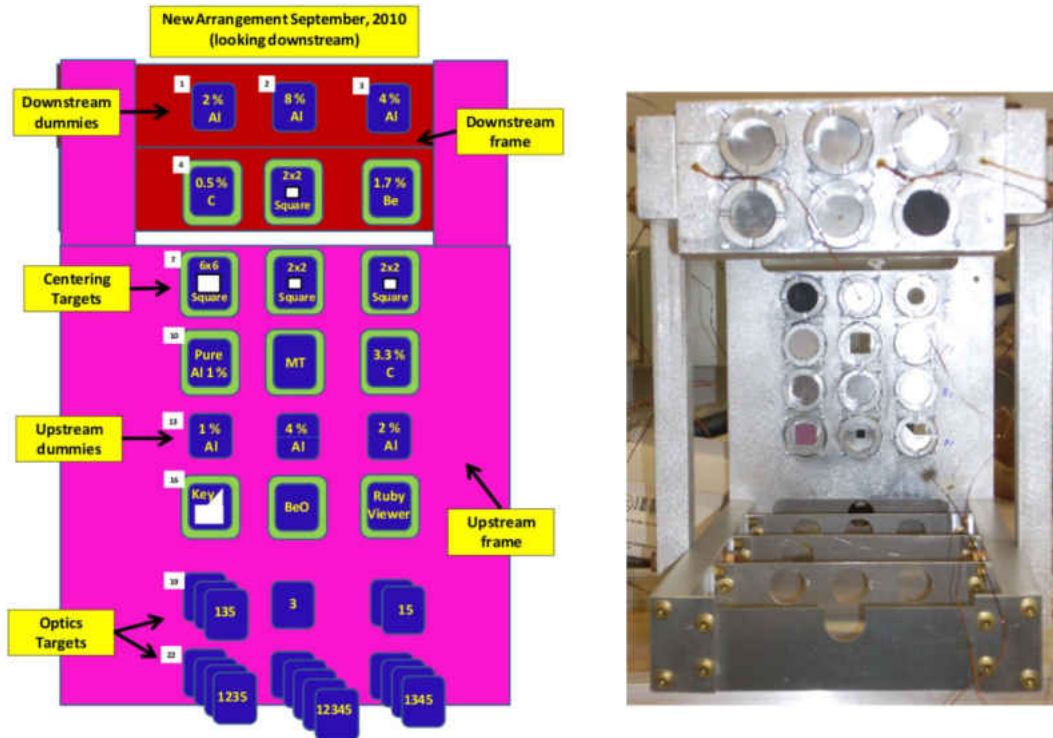
FIG. 16: Solid Target ladder during Qweak's Run I. The picture on the right is looking upstream.

2.6 SPECTROMETER AND DETECTORS

After interacting with the target, elastically scattered electrons are focused within the acceptance profile of the QTOR magnetic spectrometer by a collimator system. The QTOR magnetic spectrometer was an air-core, iron-free, water-cooled magnet that spatially separated elastic and inelastic events and along with the collimator system removed line of sight trajectories (photons and neutrons) from the acceptance. See Figure 17. The QTOR spectrometer was made of eight identical resistive coils
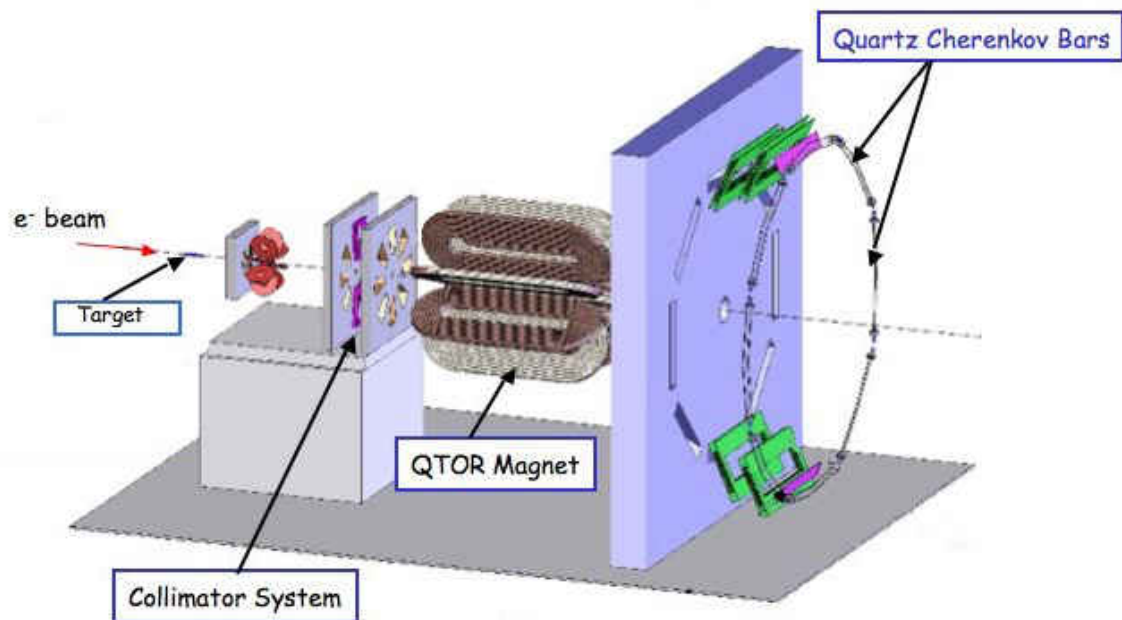
FIG. 17: Diagram of some of the key components downstream of the target. The electron beam is moving from left to right.

arranged azimuthally around the beam line. Each coil was a racetrack shaped double pancake of thirteen turns of copper wire with 2.2 meter long straight sections and semi-circular curved sections with inner (outer) radius of 0.235 m (0.75 m).

The main detector system for Qweak consisted of a set of eight Cerenkov detectors made of non-scintillating, low luminescent synthetic quartz bars. They were radiation hard and insensitive to neutral backgrounds. The quartz used in these detectors had an index of refraction of $n = 1.482$ at 280 nm wavelength, corresponding to a Cerenkov cone angle of 47.6^o and a threshold of $\beta = 0.67$. The quartz radiators were

$100 \, \text{cm} \times 18 \, \text{cm} \times 1.25 \, \text{cm}$ and were attached to two $18 \, \text{cm} \times 18 \, \text{cm} \times 1.25 \, \text{cm}$ light guides. Pairs of these bars and lightguides were glued together end-to-end to form 240 cm long bars.

Photo-multiplier-tubes (PMT's) were attached at the end of each of these bars. These had ten stages of high gain dynodes with a linear focus design. The PMTs were sensitive in the wavelength range of 200 to 900 nm and had a peak quantum efficiency of $\sim 23\%$ at 260 nm. The PMTs were magnetically shielded with mu-metal cases. Cerenkov light produced by scattered electrons was collected by the PMTs at each end of the bars. Approximately 98 photo electrons were generated from each incident electron. Two PMT bases were used. One was for high gain event mode calibration and was designed to run at low beam currents on the order of nano Amperes. The other was for low gain integrating mode production running at 180 μA. Soft neutral backgrounds were suppressed by the installation of 2 cm thick lead pre-radiators in front of each quartz bar. The light yield thereby was increased by a factor of seven and the signal-to-background ratio was improved by ~ 20. Shower fluctuations in these pre-radiators were the cause of an additional 10% excess noise in the total asymmetry width.

The eight detectors were mounted symmetrically about the beam axis with a minimum radius of 3.44 m. They were 5.78 m downstream of the center of the QTOR magnet and in the spectrometer focal plane [23].

2.7 SOFTWARE AND DATA ACQUISITION

The data acquisition (DAQ) system was built to operate in two distinct modes. Integrating mode was used in the main data taking part of the experiment and recorded the average detector and beamline instrumentation signals every MPS. Event mode was used to record trajectory data for individual particles based on detector based triggers. This mode was used for calibration of the detectors and electronics. In integrating mode low-noise pre-amplifiers converted the Cerenkov main quartz detector anode currents to voltage signals. The output had a range of ± 10 V to match the analog to digital converter (ADC). The data was written to

disks at a rate of 6.5 MB/s in data files that were 1.9 GB maximum. These files represented around five minutes of beam time and were called "runlets". For one hour of data taking, between ten and twelve runlets were created [16].

CHAPTER 3

ASYMMETRY AND NOISE IN THE QWEAK

EXPERIMENT

Qweak measured small asymmetries between detector yields when the electron beam is longitudinally polarized to either right handed(+) or left handed(-) helicity states. The mean of this asymmetry will be used to find the weak mixing angle and the weak charge of the proton. The width of the asymmetry distribution gives us a good indication of the noise and uncertainty in the experiment. Buried inside the asymmetry widths (called *sigma*, the standard deviation of the asymmetry distribution) is information on target density changes.

To find both the mean offset and the asymmetry widths, the Qweak asymmetries, A_{PV} from Equation 9, are used to fill histograms. These histograms are then fitted to the normal distribution and the values of interest calculated from the fit. The normal, or Gaussian, distribution is given by

$$P(x) = \frac{1}{\sigma\sqrt{2\pi}} \exp\left(-\frac{(x-\mu)^2}{2\sigma^2}\right) \tag{21}$$

where μ is the mean and σ^2 is the variance of the distribution. The square root of the variance, σ, is the standard deviation of the Gaussian fit that is used to characterize the uncertainty in the experiment. It corresponds to the half width of the peak at about sixty percent of the full height (See Figure 3). The value of the mean ($\mu \approx 230$ ppb compared to $\sigma \approx 230$ ppm) was small enough to be ignored in this study. The width of the asymmetry distribution from the Qweak measurements, σ_m, is due to the statistical uncertainty, σ_0, the uncertainty in current measurements from the beam current monitors (BCM's), σ_{bcm}, and the target boiling and density changes, σ_{tgt}. These contributions add in quadrature to produce the experimental uncertainty
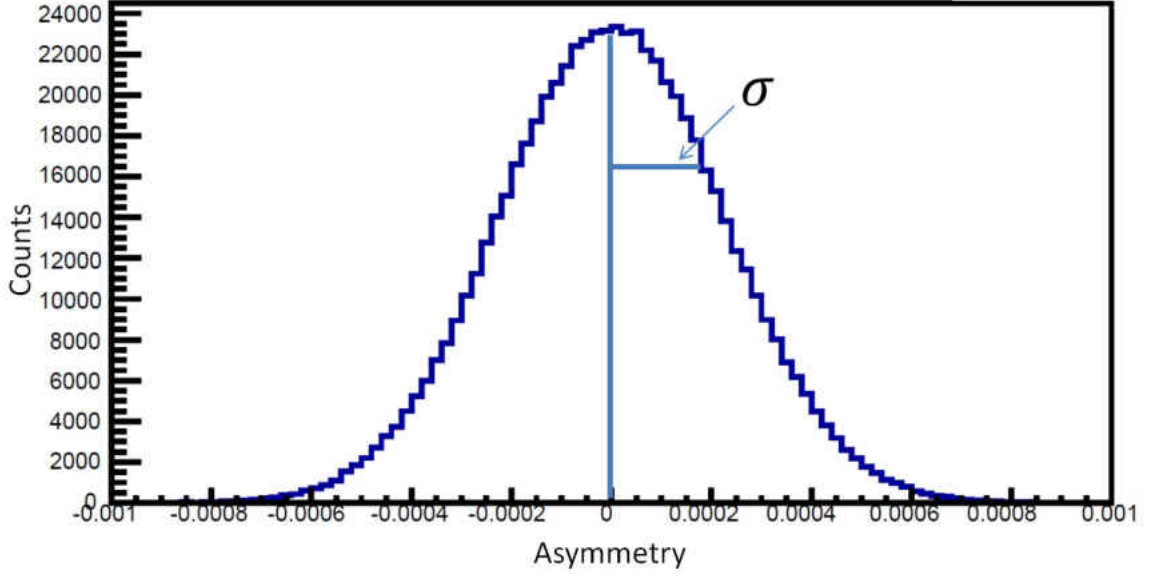
FIG. 18: σ_m, yield asymmetry histogram

Parameter	Nominal value	Range
Helicity reversal frequency [Hz]	960	30-960
Beam current [μA]	180	160-360
LH2 pump speed [Hz]	30	10-30

TABLE 5: Parameters varied in this study. As will be seen later, the helicity reversal frequency will be replaced with a mock helicity reversal frequency which corresponds to half the values given here.

in the asymmetry values.

$$\sigma_m^2 = \sigma_0^2 + \sigma_{bcm}^2 + \sigma_{tgt}^2 \tag{22}$$

The equation for the asymmetry calculation may be recast in terms of detector yields, Y

$$A = \frac{Y_+ - Y_-}{Y_+ + Y_-} \tag{23}$$

The beam was helicity flipped at a rate of 960 Hz, or once every 1042 μs (T_{hel}) and consisted of quartets of helicity states, $(+--+)$ or $(-++-)$. The first state was randomly determined and the corresponding quartet pattern then completed. In order to investigate the target noise at this and other timescales, "mock helicity

patterns" were formed (see Figure 19). These are patterns that tag MPS's with either plus or minus for the asymmetry calculations. The RMS width of the histograms is independent of the mean value and the actual helicity state does not have any bearing on the RMS from the mock helicity patterns. For this reason, actual beam helicity information was ignored in the formation of the "mock helicity patterns". All the following studies were done using the $(+--+)$ pattern alone. If we consider one quartet pattern as one period, the quartet pattern has a pattern frequency of 480 Hz. The possible frequencies that could be formed using the mock helicity
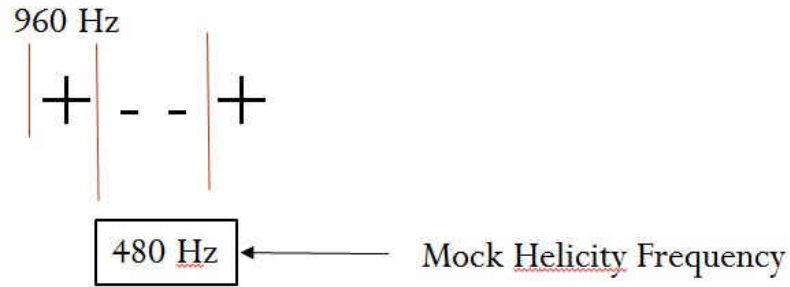
FIG. 19: Mock Helicity frequency for a quartet from the Qweak experiment. Each MPS is assigned a "+" or "−" for the asymmetry calculation. The MPS frequency was 960 Hz. Half of the time to complete a quartet is spent in each mock helicity state so the quartet, a pattern of 4 MPS's, is assigned a frequency of 480 Hz.

FIG. 20: Mock helicity states for 240 Hz. The green vertical line marks the end of one pattern and the beginning of another. A quartet has 4 MPS's per pattern (480 Hz). By making a similar pattern with 8 MPS's, a mock helicity pattern with an associated frequency of 240 Hz can be made. Instead of the two "+" states per pattern for quartets, these patterns have 4 "+" states each.

patterns is limited by the need for an equal number of "positive" and "negative" states. The frequencies chosen and the number of MPS's needed per pattern, N_{pat}, for each frequency can be seen in Table 6 and Figure 20. The relationship between

the N_{pat} and frequency is

$$f = \frac{2}{N_{pat} * T_{hel}} \tag{24}$$

Frequency (Hz)	480	240	120	96	80	60	48	40	30	15
N_{pat}	4	8	16	20	24	32	40	48	64	128

TABLE 6: Mock helicity patterns were formed by grouping MPS's into different sized patterns. The frequencies for each pattern size were found using Equation 24. Note that these frequencies correspond to a helicity reversal frequency of twice that mentioned in the table, ie. 480 Hz mock helicity pattern is the same as 960 Hz helicity reversal rate.

ROOT macro's were written to calculate the measured and BCM noise from the ROOT files which contain the Qweak data. ROOT is a software package developed at CERN (European Organization for Nuclear Research) that was designed to handle large data sets [27]. After importing the data from the main detectors, the mock helicity patterns were formed by calling the entries in the asymmetry equation in a way similar to Figure 20 for all ten pattern frequencies of interest. The results of the asymmetry calculations were then used to fill histograms and the standard deviation is extracted.

This resulted in σ_m for ten different mock helicity frequencies. The macro also computed σ_{bcm} and σ_0. The uncertainty from the BCM's was computed in a similar way to the experimental uncertainty, see Section 3.2, while the counting statistics were determined by counting events, see Section 3.1. The uncertainty due to target boiling is then found by subtracting in quadrature as in Equation 22. For more information on the coding, please see Appendix 2.
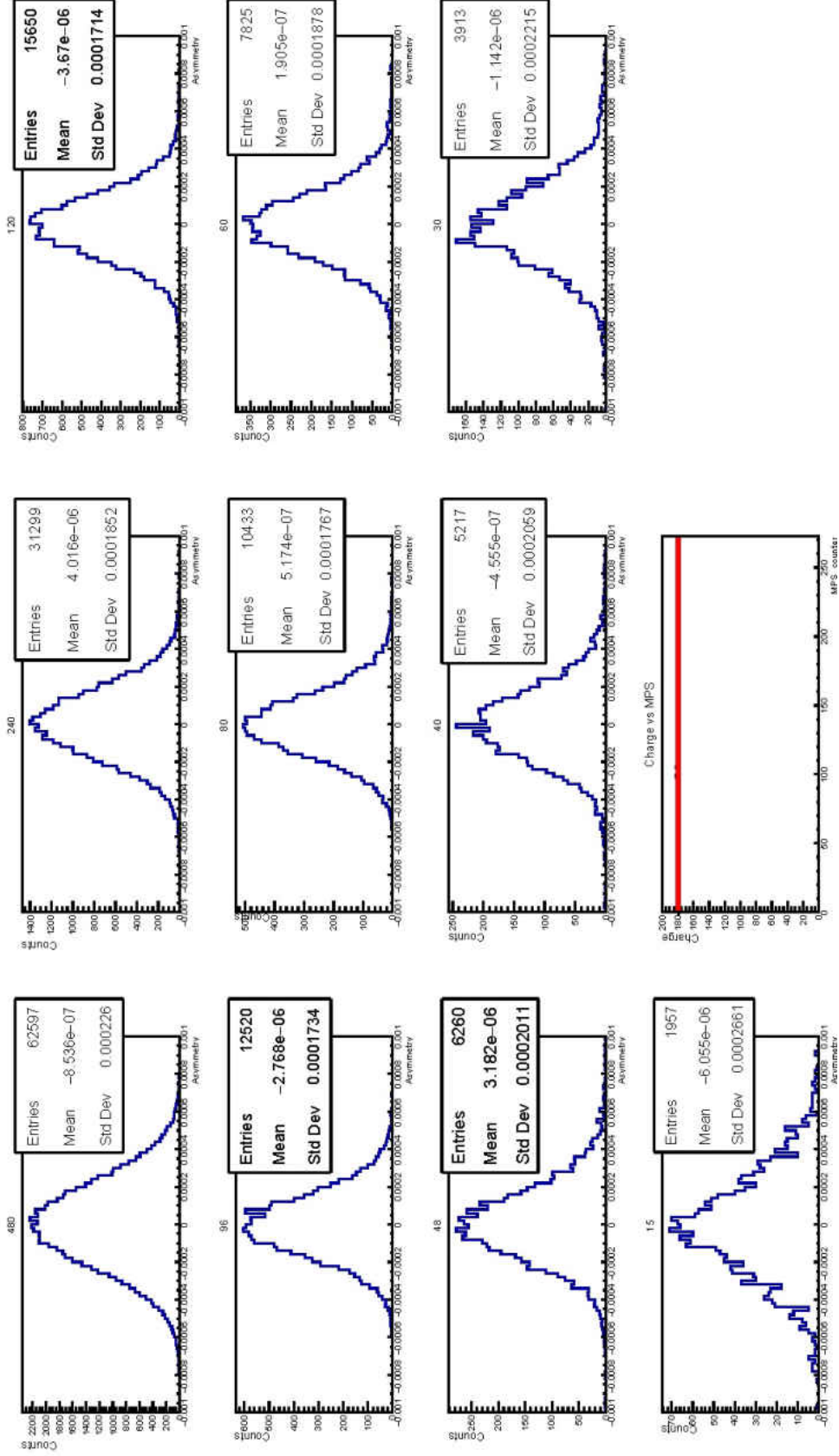
FIG. 21: Histograms produced by the ROOT macro for run 17250 (Run 2), with $I_{beam} = 179 \mu A$. The vertical axis' are counts and the horizontal axis' are asymmetry vales. The titles are pattern frequencies. The last plot is a plot of the current value during the run and the average value is in red.

In this way, three pages of plots were created with each run of the macro. One page contained ten histograms for the experimental uncertainty, σ_m, evaluated individually for the ten mock helicity frequencies (Figure 21). The second page contained the histograms for the BCM uncertainty for all ten frequencies. The third was a frequency plot which contained the RMS extracted from the histograms for the measured and BCM uncertainties as well as the counting statistics for each frequency. The BCM uncertainty and counting statistics are subtracted in quadrature to leave the target uncertainty (Figure 22).
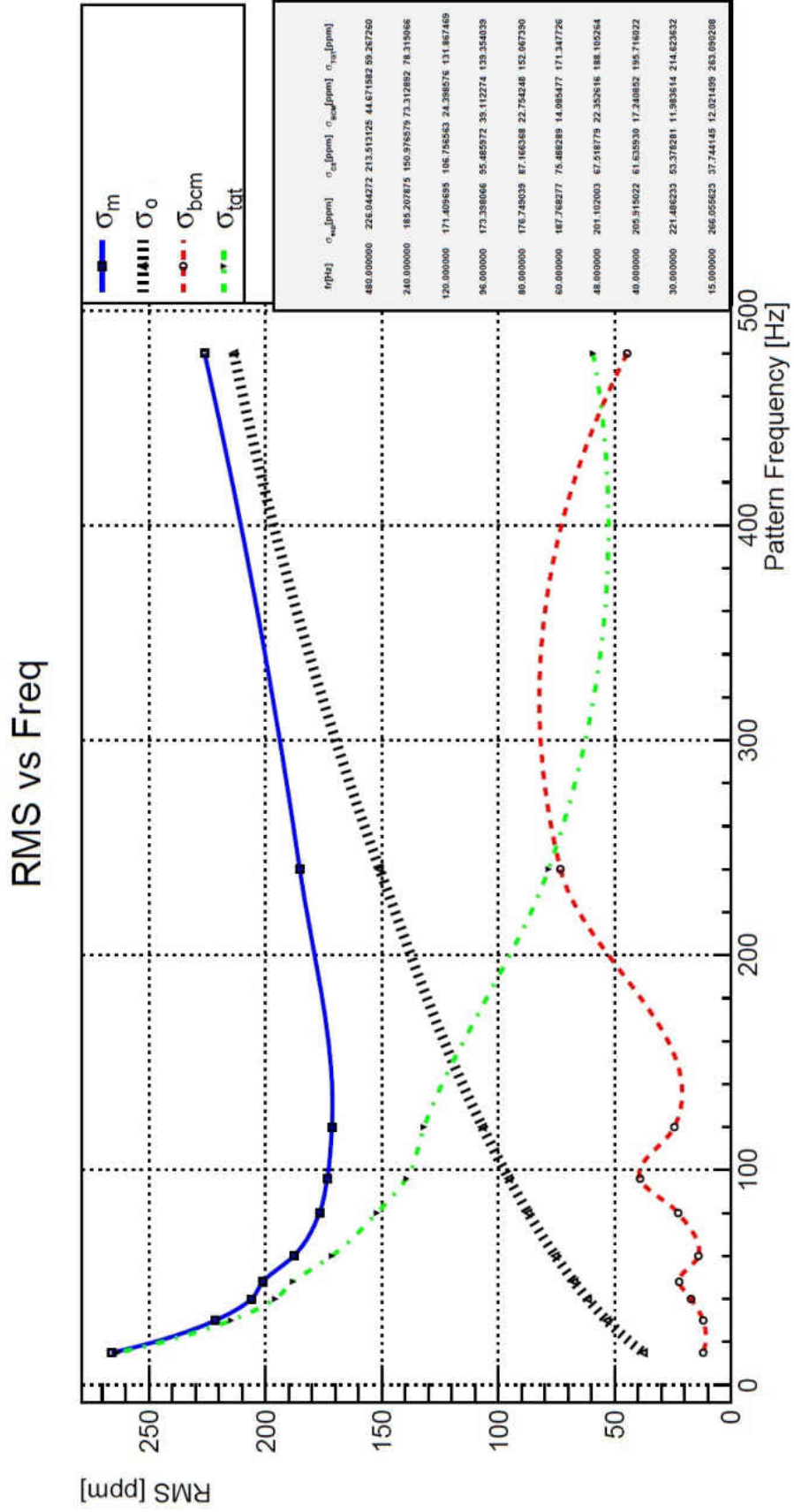
FIG. 22: Extracted RMS values from the ROOT macro on run 17250 (Run 2), with $I_{beam} = 179\mu A$. The lines are not physical and are there to help guide the eye.

The following analysis in this chapter were performed on thirteen data sets of the Qweak experiment. When the project started, 45 already replayed ROOT files were available. Nineteen of these were from the target boiling study done in May 2011 at the end of Run 1. These were meant to study the contribution of the raster size and shape, the pump speed, and the beam current on target boiling. The term target boiling is meant to be inclusive of all density fluctuations. For this study, the term density fluctuations will be used to include time-dependent changes in the LH2 and any boiling of the LH2. The other twenty-six Root files were about equally split between Run 1 and Run 2. As a representation of the process of target boiling noise extraction, a data set (run 17250) will be used. The parameters for run 17250 can be seen in Table 7 [28]. Before the actual asymmetries were found, the first step was

Date	Beam energy(MeV)	Beam current(μA)	Raster size(cm)	Pump frequency(Hz)
5-31-2012	1162.06	179	4×4	29

TABLE 7: Parameters for run 17250

identifying the runs and it's parameters that would be used. Since it was decided not to include the raster size in this study, only runs using the nominal raster size, 4×4 cm were used. The Qweak log book [28] was used exclusively for identifying the parameters of the runs. Once a run was determined to be a good candidate, a simple code to plot the current for each runlet of that run was used to look for beam trips and any other anomalies from the electron beam. An example can be seen in Figure 24. This particular run had five runlets which had good beam and these would be used for all of the calculations to follow. At first it was thought that the runlets with beam trips could be used by including code to exclude the parts where the beam dropped below a certain threshold. This method was to be used if more data points were needed to fill the histograms. This turned out to be unnecessary (see section 5.3).

3.1 STATISTICAL UNCERTAINTY

The RMS of the detector yield asymmetry in this experiment was dominated by
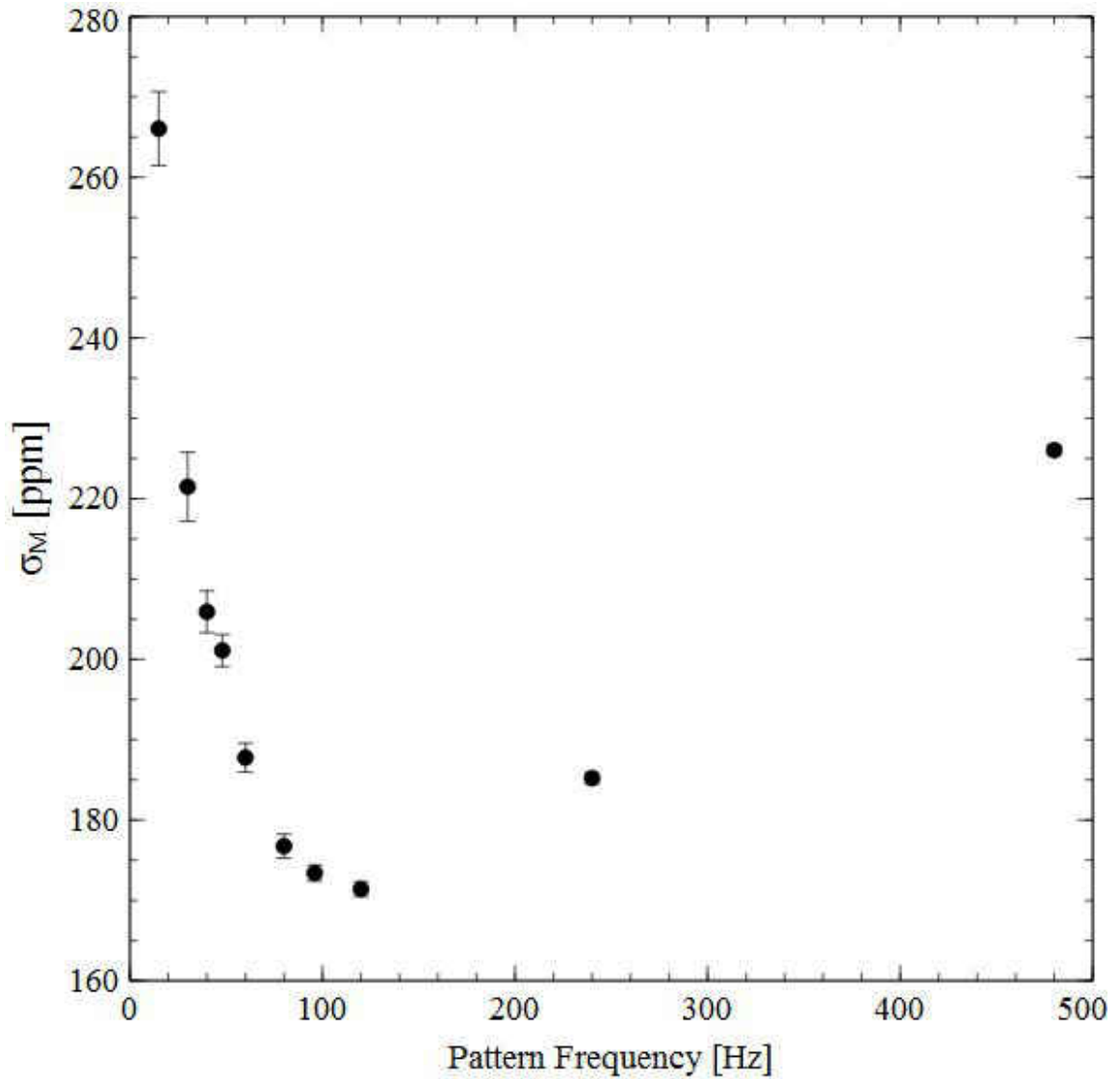
FIG. 23: The experimental uncertainty from the main detectors as a function of frequency for run 17250 (Run 2). In this case, $I_{beam} = 179\mu A$.
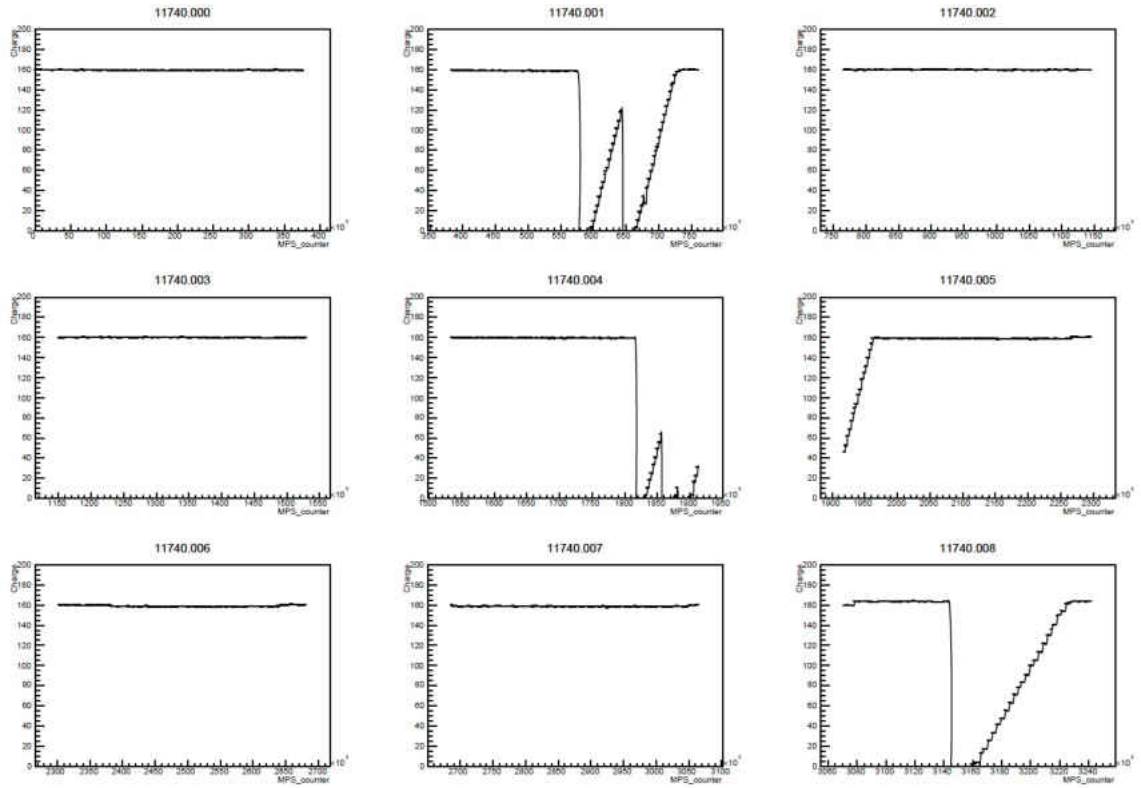
FIG. 24: The current, labeled Charge, as a function of MPS number for nine runlets comprising run 11740. The average current for this run was 160 μA. The beam trips can be seen in segments 001, 004, 005, and 008. These runlets were not included in the analysis.

counting statistics. To find the the contribution to the measured asymmetry, σ_m is recast again in terms of the number of events detected as

$$A = \frac{N^+ - N^-}{N^+ + N^-} = \frac{\Delta N}{N} \tag{25}$$

where A is a function of two variables, $A(N^+, N^-)$. $N^{\pm}$ is the number of particles detected when the beam is in either the $(+)$ or $(-)$ helicity state. $N = N^+ + N^-$ is the total number of particles detected. The variance is

$$\sigma_{CS}^2 = \left(\frac{\partial A}{\partial N^+}\right)^2 \sigma_{N^+}^2 + \left(\frac{\partial A}{\partial N^-}\right)^2 \sigma_{N^-}^2 + 2\operatorname{cov}(N^+, N^-)\frac{\partial A}{\partial N^+}\frac{\partial A}{\partial N^-} \tag{26}$$

where $\sigma_{N^+}^2 = N^+$ and $\sigma_{N^-}^2 = N^-$ are the variances of the two variables independently and are given by the Poisson distribution. The covariance in the third term will be zero since N^+, N^- are independent measurements. Taking the derivatives,

$$\frac{\partial A}{\partial N^+} = \frac{2N^-}{N^2} \tag{27}$$

$$\frac{\partial A}{\partial N^-} = -\frac{2N^+}{N^2} \tag{28}$$

and inserting them into Equation 26 we have

$$\sigma_{CS}^2 = \frac{4N^+ N^-}{N^3} \tag{29}$$

If N^+ and N^- are approximately equal, then ΔN is very small, $N^+ \approx N^- \approx \frac{N}{2}$ and the RMS due to counting statistics is

$$\sigma_{CS}^2 = \frac{1}{N} \tag{30}$$

To estimate N the "deadtime", T_{dead}, must be taken into account. T_{dead} is associated with the helicity reversal switching time (70 μs) and the gate delay (42.5 μs). During this time interval between MPS's the experiment is effectively shut off. In terms of individual helicity states, $T_{dead} = 112.5$ μs per state [16]. The "live-time" ratio, s, is

independent of the number of particles per pattern (quartets in this case), N_{pat}, and is

$$s = 1 - \frac{N_{pat}T_{dead}}{N_{pat}T_{hel}} = 1 - \frac{T_{dead}}{T_{hel}} = 89.2\% \tag{31}$$

By knowing the beam current and detector rate,

$$N = R_{det} \cdot I_{beam} \cdot N_{pat} \cdot T_{hel} \cdot s \tag{32}$$

where R_{det} is the detector rate in GHz/μA, I_{beam} is the beam current, N_{pat} is the number of helicity states in a pattern, and T_{hel} is the time spent in one helicity state (1042 μs). To study different timescales, patterns larger than quartets can be formed and N can be expressed as a function of I_{beam} and N_{pat} since for a LH2 target R_{det}, T_{dead}, and T_{hel} are constant.

$$N = \alpha I_{beam} N_{pat}, \quad \alpha = R_{det}(T_{hel} - T_{dead})[\text{A}^{-1}] \tag{33}$$

The detector rate for a LH2 target was determined by simulations to be $R_{det} \approx$ 7GHz/180μA [16], so

$$N = 3.61 \times 10^{10}[\text{A}^{-1}]I_{beam}N_{pat} \tag{34}$$

Note that α will be different for targets other than LH2. In addition to the counting statistics, the uncertainty also depends on the detector resolution or electron detection efficiency in the main detectors. The main detectors in Qweak are Cerenkov detectors and the resolution, R, was determined to be 47% sigma. The resolution is included in the statistical uncertainty, σ_0, by way of a fractional increase in the counting statistics [16].

$$\sigma_0^2 = \sigma_{CS}^2(1 + R^2) = 1.22\sigma_{CS}^2 \tag{35}$$

Combining this result with Equations 30 and 34 we have

$$\sigma_0^2 = \frac{3.38 \times 10^{-11}[\text{A}]}{I_{beam}N_{pat}} \tag{36}$$

As an example the nominal operating conditions of Qweak are with $I_{beam} = 180\ \mu$A and $N_{pat} = 4$ making $\sigma_0^2 = 46.9$ ppb or $\sigma_0 = 217$ ppm. The ROOT code used to extract the counting statistics from the Qweak data used this method and using N_{pat} instead of frequency was a matter of convenience. It is easier to visualize (see Figure 25) by combining Equations 24 and 36.

$$\sigma_0 = 1.33 \times 10^{-7} \sqrt{\frac{f}{I_{beam}}} \tag{37}$$

3.2 BCM NOISE

The current in the Qweak experiment was found using the average of two BCM's (BCM1 and BCM2) during run 1 and from only one BCM (BCM8) in run 2. BCM's 1 and 2 were analog in nature while BCM's 7 and 8 used new digital receivers which had improved digital signal processing utilizing 18-bit, 1 MHz DAC's to generate the output voltage. The noise in the experiment due to uncertainty in the BCM's were found using the double difference of a pair of BCM's (BCM's 1 and 2 for run 1 and BCM's 7 and 8 for run 2). The double difference (DD) for run 1 is defined as

$$DD = \frac{Q_1^+ - Q_1^-}{Q_1^+ + Q_1^-} - \frac{Q_2^+ - Q_2^-}{Q_2^+ + Q_2^-} \tag{38}$$

where Q_i^j represents the charge measured in BCM i for beam helicity j. By finding the width of the DD for many different patterns we can find σ_{dd} [16].

The resolution of an individual BCM is

$$\sigma_{bcm} = \frac{\sigma_{dd}}{\sqrt{2}} \tag{39}$$

An example analysis can be seen in Figure 26

3.3 TARGET NOISE
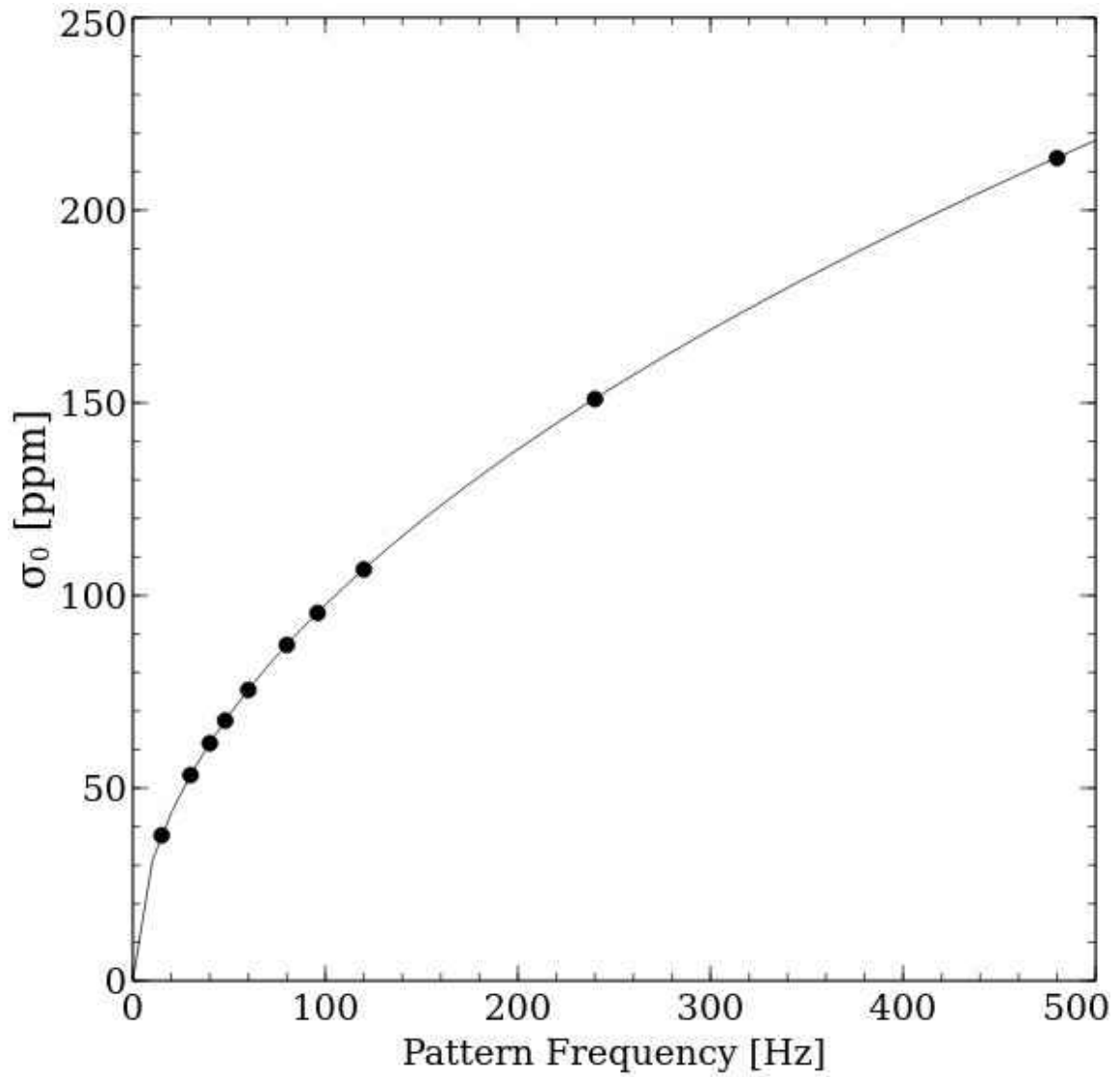
FIG. 25: The contribution to the experimental uncertainty from counting statistics as a function of frequency. To match run 17250, $I_{beam} = 179\mu A$. The frequencies of interest are shown as points and line is Equation 37.
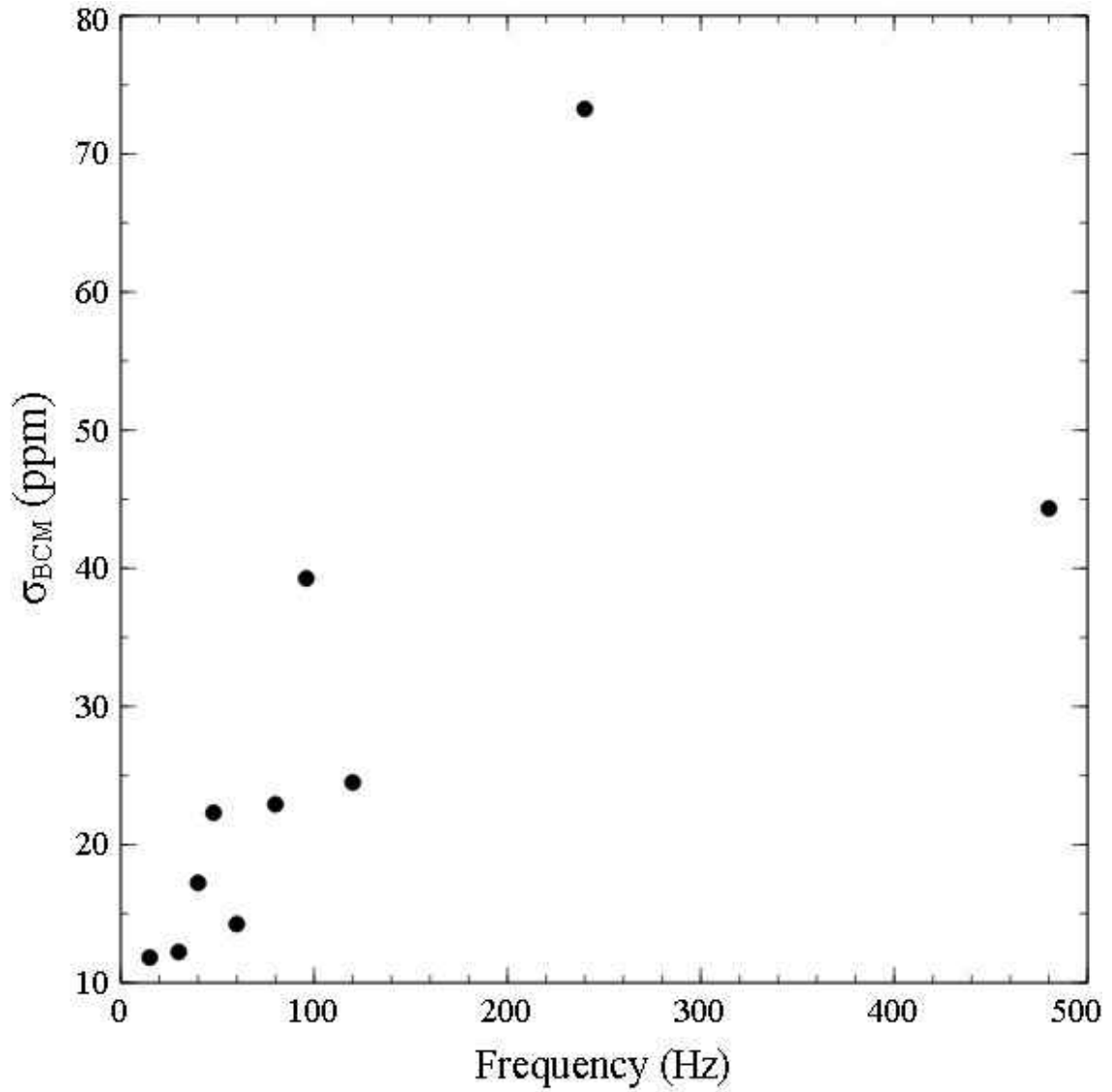
FIG. 26: The contribution to the experimental uncertainty due to the digital beam current monitors in run 17250 as a function of frequency.

Once the values for the statistical uncertainty (σ_0) and the BCM uncertainty (σ_{bcm}) are found they may be subtracted form the experimental uncertainty (σ_m) in quadrature. This ignores any other source of noise and this will be discussed in Section 5.3. From Equation 22,

$$\sigma_{tgt}^2 = \sigma_m^2 - \sigma_0^2 - \sigma_{bcm}^2 \tag{40}$$

Using Equations 36 and 39 this can be put in terms of known variables:

$$\sigma_{tgt}^2 = \sigma_m^2 - \frac{3.38 \times 10^{-11} [\mathrm{A}]}{I_{beam} N_{pat}} - \frac{\sigma_{dd}^2}{2} \tag{41}$$

As an example with run 17250 (run 2) only looking at 480 Hz, $\sigma_m = 226$ ppm, $\sigma_{bcm} = 44.33$ ppm, with $N_{pat} = 4$, and $I_{beam} = 179$ μA, $\sigma_0 = 213.5$. This results in $\sigma_{tgt} = 59.51$ ppm.
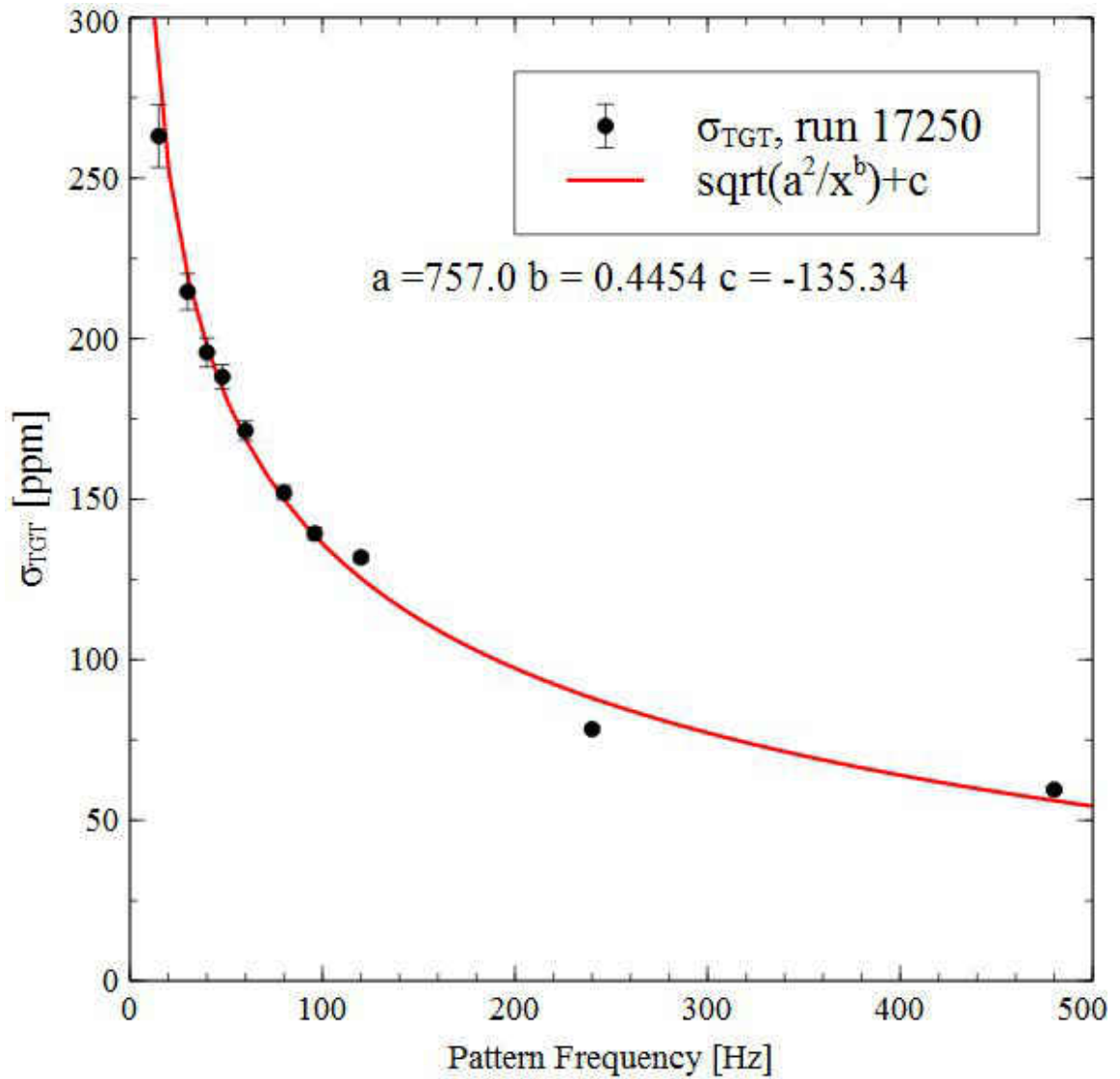
FIG. 27: The contribution to the experimental uncertainty due to target density changes as a function of frequency.

CHAPTER 4

THE QWEAK TARGET SIMULATION WITH CFD

Fluent is one of the many software packages offered by Ansys Inc. It uses the finite volume method to solve for liquid and gas flows for a wide range of incompressible and compressible, laminar and turbulent fluid flow problems. Ansys includes a computer aided drafting type module called Design Modeler and a meshing module. Both of these have CFD specific options and work flow that are easily interfaced with Fluent [29]. Similar to the finite difference method or finite element method, values are calculated at discrete places on a meshed geometry. "Finite volume" refers to the small volume surrounding each node point on a mesh. In the finite volume method, volume integrals in a partial differential equation that contain a divergence term are converted to surface integrals, using the divergence theorem. These terms are then evaluated as fluxes at the surfaces of each finite volume. Because the flux entering a given volume is identical to that leaving the adjacent volume, FVM is conservative by nature. Another advantage of the finite volume method is that it is easily formulated to allow for unstructured meshes, which are described in the next section. This method is used in many computational fluid dynamics packages including Fluent.

4.1 DISCRETIZATION AND THE FINITE VOLUME METHOD

Fluid (gas and liquid) flows are governed by partial differential equations for mass, momentum, and energy. In order to solve for fluid flows in complex geometries the flow space is broken into multiple finite sized control volumes (sub-domains or cells) and the differential equations are integrated over each sub-domain. This process begins with grid creation or meshing. The grid defines the control volumes by setting up a series of points and edges between. There are two main types of grids, structured and unstructured. A structured grid is one in which all the cells

are hexahedral. In three dimensions this translates as a grid made of topological parallelepipeds. In contrast, an unstructured grid is not made of topological parallelepipeds and the cells can be tetrahedral, hexahedral, etc. The finite volume method works with either structured or unstructured grids. The advantages of a structured grid is that neighbors of a given point may be directly found by increment of indices. Unstructured grids require specific procedures to identify neighbors but are better at adapting to complex geometries. The Qweak target was meshed using a combination of structured and unstructured grids. The majority of the target uses tetrahedrons to capture the complicated geometry of the flow space. The volume through the center of the target where the beam interacts with the LH2 (4x4x345 mm^3) was meshed with a structured grid since the only external frontier of this volume is at the beam nipples. The Fluent meshing module handles the tetrahedral grid formation very easily with only slight modifications to the default settings. The beam volume required more attention and will be discussed in Sections 4.5 to 4.8.

Once the grid and control volumes have been produced the flow space changes from a single domain to many sub-domains and the second step in the finite volume method begins. This step involves integration of the governing differential equations on each control volume to ensure conservativity at the discrete level.

4.2 ANSYS DESIGN MODELER

After importing a CAD (computer-aided drafting) model of the target into Ansys Design Modeler (Figure 28), the flow space had to be set up for the simulation. The walls of the target cell are only important for this study at the windows. These solid zones can either be imported in the Design Modeler and meshed with the rest of the flow space or defined later in Fluent using shell conduction. Meshing the aluminum slowed down the simulation and made the simulation more unstable so shell conduction was used. Shell conduction replaces the normally zero-thickness walls with cells extruded from the mesh boundaries on the wall. The windows were named in Design Modeler for easier access to them later in Fluent. The fluid space was checked for any errors and a separate cell zone set up to mimic the beam interaction
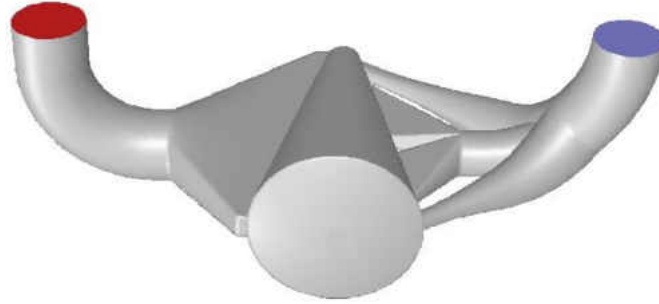
FIG. 28: The CAD model only contained zero-thickness walls defining the flow space and had no definition of interaction region or window thickness. The blue circle is the inlet and the red circle is the outlet.

volume. This $4 \times 4 \times 34.5$ cm^3 rectangular zone was capped at the ends with the shell conduction for the Aluminum windows and the external boundaries inside the cell represented the edge of the Lissajous raster pattern. The fluid flows freely through these interior boundaries between the interaction region and the rest of the cell. After this stage the Qweak model was ready for CFD and imported into the meshing module.

4.3 ANSYS MESH

The meshing program has many options and only the most important ones will be discussed. Through studying the literature on CFD, and trial and error, the vital parameters were determined. Without the beam interaction zone the meshing works fine with the default settings. This led to large (> 0.5 cm) mesh elements at the center of the target cell in the beam interaction region. Without defining a zone for the mesh elements at the interaction region, however, some of the elements have centroid's within the interaction region but the cells extend past the boundary of the interaction region. This results in a volume discrepancy and the power density must be adjusted to accommodate the volume of the mesh elements in the model. To avoid this problem the beam interaction region was meshed separately. While the rest of the target was meshed with an unstructured mesh (tetrahedrons), the beam volume used a structured (quadrilateral) mesh. The structured mesh forced
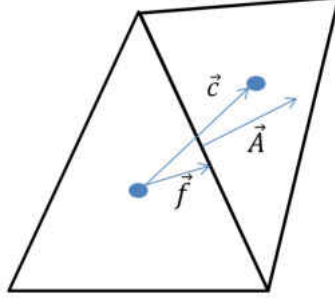
FIG. 29: Definitions of vectors used in calculating orthogonal mesh quality. $\vec{A}_i$ is area vector of the face between the two tetrahedral cells. $\vec{f}_i$ is the vector from the cell centroid (blue dots) to the same face. $\vec{c}_i$ is the vector connecting the centroid of the cell in question with the centroid of the adjacent cell

the mesh elements to have their edges lay along the beam volume boundaries and the volume difference between the model and the actual target minimized. The two most important parameters in the mesh was the number of elements and the quality of the mesh elements. Too many elements would slow down the calculation and poor quality would hamper convergence of the solution. The main parameter used to measure the quality of a mesh is called orthogonal quality. It ranges from zero to one, with one being the highest quality. A simplified diagram can be seen in Figure 29. The quantity is defined as the minimum value from two calculations per face. The first is the normalized dot product of the area vector of a face ($\vec{A}_i$) and the vector from the cell centroid to the same face ($\vec{f}_i$).

$$\frac{\vec{A}_i \cdot \vec{f}_i}{|\vec{A}_i||\vec{f}_i|} \tag{42}$$

The second is the normalized dot product of the same face area vector with the vector connecting the centroid of the cell in question with the centroid of the adjacent cell that shares the face ($\vec{c}_i$).

$$\frac{\vec{A}_i \cdot \vec{c}_i}{|\vec{A}_i||\vec{c}_i|} \tag{43}$$

These values are computed for every face in the cell and the minimum is reported
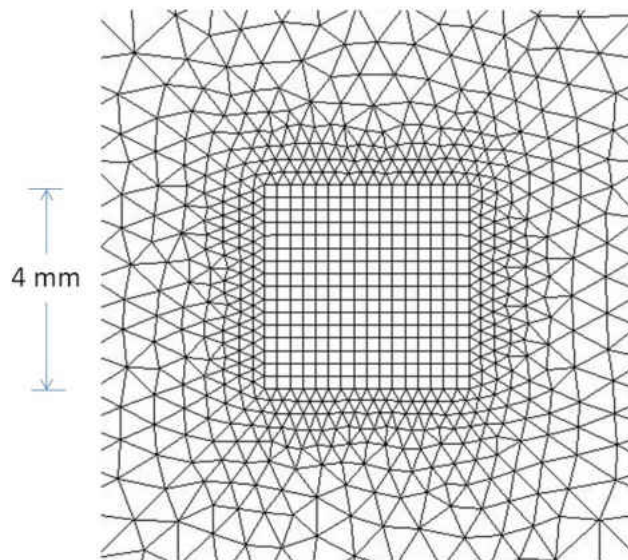
FIG. 30: Closeup of the beam exit window mesh. The square in the center is the 4×4 mm edges of the Lissajous raster pattern. Inside this square the mesh is structured and cubic while the rest of the cell is unstructured tetrahedrons.

as orthogonal mesh quality for that cell. For the entire model an average is taken. This proved valuable not only for judging overall quality, but also in finding areas of poor quality mesh to fix. Many meshing attempts were made and tested to quantify the effect on convergence and processing time. For the time dependent simulation using 1 μs timesteps (1000 steps for every MPS) a compromise was reached with 21 million elements and a minimum orthogonal quality of 0.15. The elements inside the beam volume were evenly spaced cubes of side length 150 μm. This structured mesh can be seen in Figures 30 and 31.

The size of the structured mesh was chosen to minimize volume error in power deposition as well as maximize the speed of calculations. The volume of the beam interaction region was critical. It is easily calculated for the entire raster volume as $0.4 \times 0.4 \times 34.5$=5.52 cm^3 (see Figure 32). This was the case for the steady state solution. For the beam spot with $r_{beam} = 0.01$ cm, $\pi r_{beam}^2 34.5 = 0.0108\,\mathrm{cm}^3$. The beam interaction volume was found with a User-Defined-Function (UDF) each time step by integrating the volume of every mesh element that was tagged for
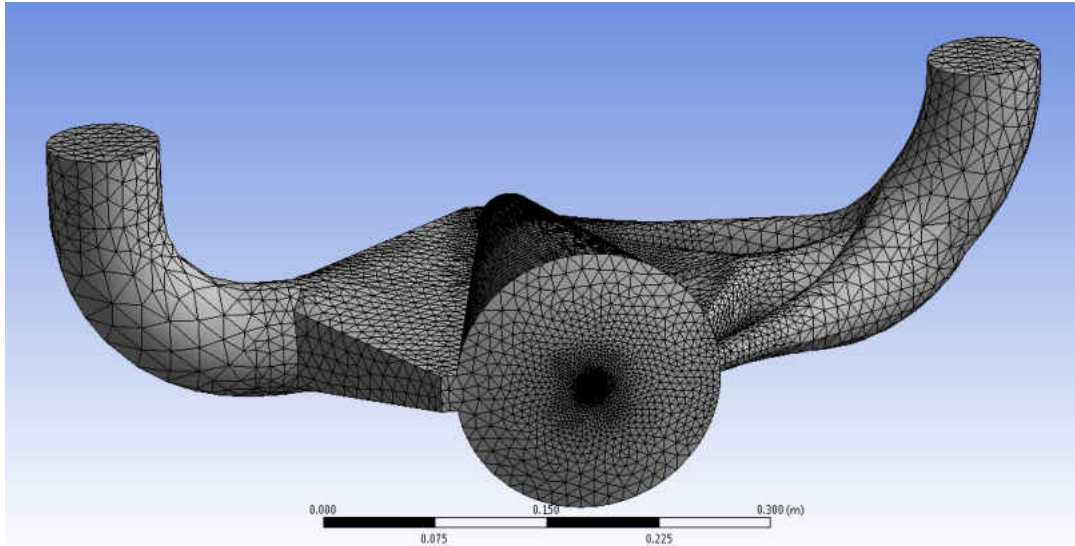
FIG. 31: The flow space in the Qweak target meshed with a combination of structured and unstructured grids. The structured part is through the raster volume at the center of the target. The growth of the cell size from the 250μm elements in this region to the larger cells can be seen.

energy deposition. A UDF is a function written in C++ that can be dynamically loaded within Fluent to enhance it's standard features. These functions can either be interpreted at each iteration or compiled into a library first and then called at each time step. Fine tuning of the numerical procedures in the UDF led to a $\Delta V/V_0 < 1\%$ at each timestep.

4.4 ANSYS FLUENT

A list of the basic Fluent options chosen for the Qweak target simulations can be seen in Table 8.

4.4.1 SOLVER

There are two types of solvers available in Fluent; density-based and pressure-based. All of the simulations for the Qweak target were done using the pressure-based solver. The pressure-based solver was used traditionally for low speed incompressible
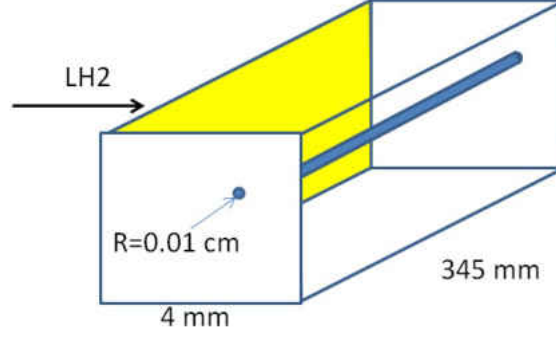
FIG. 32: The volume the beam spot makes through the interaction region of the target is the volume of the blue cylinder. The spot moves with the raster motion described in the text and completes one Lissajous pattern every MPS.

and mildly compressible flows and the density-based solver for high speed compressible flows. Both methods have been updated to handle a large range of flow regimes, but the pressure-based solver will be the focus of this explanation. Two options exist for the pressure-based algorithm: coupled and segregated. Both algorithms solve the governing integral equations for the conservation of mass and momentum. In this case there were also scalar equations such as energy and turbulence that are solved the same in either method. The difference between them can be seen in Figure 33. The coupled algorithm was used in this work. In the flow chart for the pressure-based segregated solver the equations are solved in multiple steps, while the coupled algorithm solves all the governing equations simultaneously. The equations for additional scalers like turbulence are solved sequentially afterwards. As will be described, the continuity equation is used to obtain the density field while the pressure field is determined from the equation of state. The momentum equation in integral form is

$$\oint \rho \vec{v} \vec{v} \cdot d\vec{A} = -\oint pI \cdot d\vec{A} + \oint \bar{\tau} \cdot d\vec{A} + \int_V \vec{F} dV \tag{44}$$

where I is the identity matrix, p is the static pressure, μ is the molecular viscosity, and $\bar{\tau} = \mu \left[(\nabla \vec{v} + \nabla \vec{v}^T) - 2/3 \nabla \cdot \vec{v} I \right]$ is the stress tensor.

The continuity equation is a statement of conservation of mass.
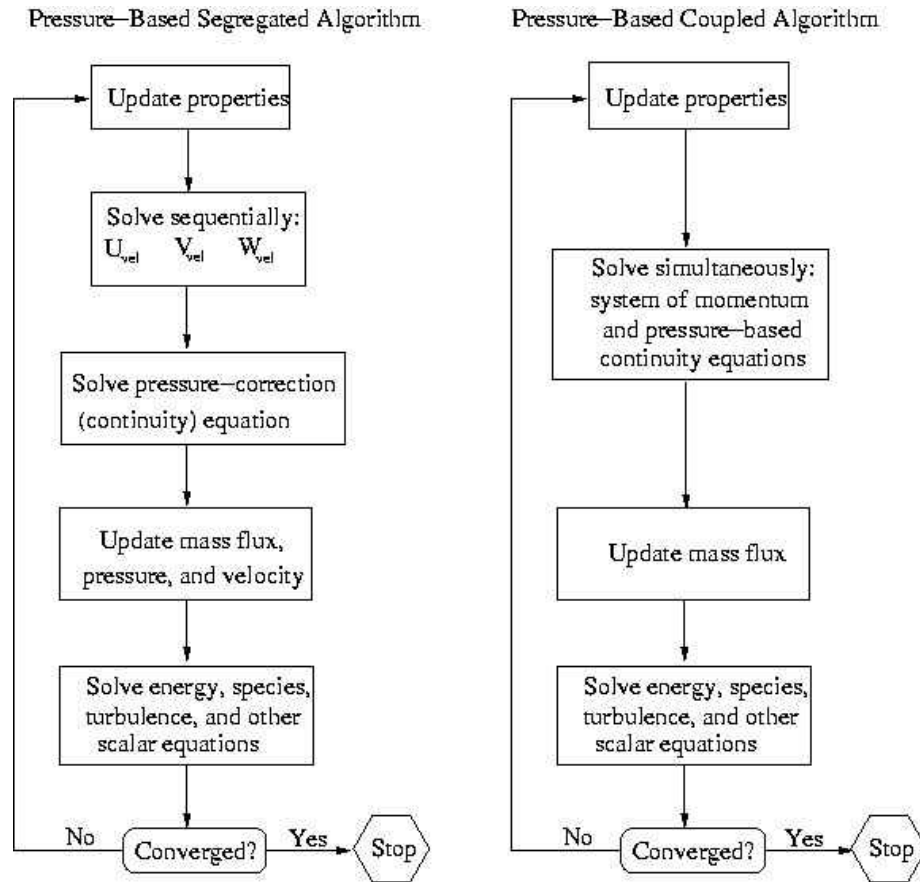
FIG. 33: Flow chart of the two algorithms available for the pressure-based solver in Fluent. The Qweak target simulation used the pressure-based coupled algorithm.

Solver Type	Pressure-Based
Velocity Formulation	Absolute
Multiphase Model	Mixture w/slip velocity
Drag Coefficient	universal-drag
Slip Velocity	manninen-et-al
Evaporation and Condensation frequency	Lee Model (0.5)
Saturation Temperature	23.705 K
Surface Tension Coefficient	constant (0.00193)
Viscous Model	Realizable k-epsilon w/enhanced wall treatment
Pressure-Velocity Coupling	Coupled
Spatial Discretion-Gradient	Least Squares Cell Based
Spatial Discretion-Pressure	PRESTO!
Spatial Discretion-Momentum	Second Order Upwind
Spatial Discretion-Volume Fraction	QUICK
Spatial Discretion-Turbulent Kinetic Energy	Second Order Upwind
Spatial Discretion-Turbulent Dissipation Rate	Second Order Upwind
Spatial Discretion-Energy	Second Order Upwind
Inlet boundary condition	$\dot{m} = 1$ kg/s, T=20 K

TABLE 8: Fluent options chosen for the simulation

$$\oint \rho \vec{v} \cdot d\vec{A} = 0 \tag{45}$$

The equation for energy is

$$\frac{\partial}{\partial t} \sum_{k=1}^{n} (\alpha_k \rho_k E_k) + \nabla \cdot \sum_{k=1}^{n} (\alpha_k \vec{v}_k (\rho_k E_k + p)) = \nabla \cdot (k_{eff} \nabla T) + S_E \tag{46}$$

Here, $k_{eff} = \sum \alpha_k (k_k + k_t)$, and k_t is the turbulent thermal conductivity. S_E is the inclusion of any other volumetric heat sources. This is where the heat deposition from the beam heating UDF is inserted into the solution process. For incompressible flows, $E_k = h_k$ and for compressible flows, $E_k = h_k - p/p_k + v_k^2/2$.

Velocity-pressure coupling is necessary to solve these equations since they are mutually dependent. Several methods are available in Fluent to implement this including coupled, SIMPLE (Semi-Implicit Method for Pressure Linked Equations),

SIMPLEC (SIMPLE Consistent) and PISO (Pressure Implicit with Splitting of Operators). SIMPLE is the standard option and works well with all flow regimes. SIMPLEC is mainly for uncomplicated flows, and PISO is geared towards transient flows with large timesteps. The coupled scheme, which was used for the simulations of the Qweak target, is more memory intensive but this ceased to be a problem when the fluent program and license were moved to a cluster (see Section 4.4). The other drawback of the coupled scheme is that it cannot be used with the Eulerian multiphase model (see Section 4.4.3). SIMPLE and coupled were both used in this study but the coupled method was used in all the following results [30].

4.4.2 VISCOUS MODEL

There are nine different models for turbulence in Fluent offered under the option "viscous model". Six of them use Reynolds averaging, where the solution variables in the instantaneous Navier-Stokes equations are put into a time averaged form. These can be seen in Figure 34. The RANS (Reynolds-averaged Navier-Stokes) models
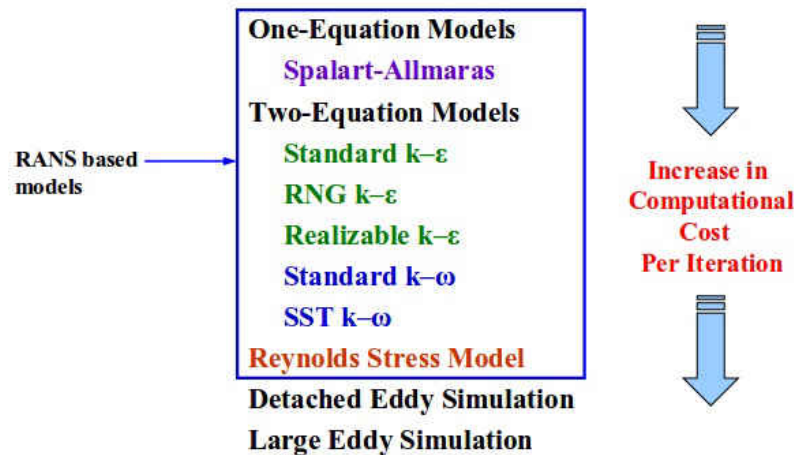
FIG. 34: The turbulence models available in Fluent. The Qweak target simulations used the Realizable $k - \epsilon$ model. RANS stands for Reynolds-averaged Navier-Stokes models

use the time-averaged Navier-Stokes equations. The other models solve the spatially averaged N-S equations. For the Qweak target, the $k - \epsilon$ model was used. It is the most widely used turbulence model. The only option turned on for the $k - \epsilon$ model

was enhanced wall treatment. This is a two layer wall model that divides the region adjacent to the wall into two layers: a viscosity affected region and a fully turbulent region.

4.4.3 MULTIPHASE MODELING

There are three main methods used to handle multiphase modeling in Fluent. The Volume of Fluid model is designed for slug flows and stratified or free surface flows. It was deemed inappropriate for the Qweak target model and will not be discussed here. The Eulerian model treats all phases as interacting continua with a single pressure shared by all the phases. The momentum and continuity equations are solved separately for each phase. The Eulerian model is mainly used for bubbly, droplet, slurry and particle-laden flows. It is perfect for sedimentation and fluidized beds. The Eulerian model is the preferred method for the Qweak simulation, but as of version 7.2 of Fluent, the model was too complicated and a working solution was not found [31].

The Mixture Method is the method used in the Qweak target simulations. It is a simplified version of the Eulerian model. It solves the momentum, continuity and energy equations for the mixture as a whole. The volume fraction equations for the secondary phases and expressions for the relative velocities are then solved separately. The momentum equation in the mixture model is obtained by summing the individual momentum equation for all phases.

$$\frac{\partial}{\partial t}(\rho_m \vec{v}_m) + \nabla \cdot (\rho_m \vec{v}_m \vec{v}_m) = -\nabla p + \nabla \cdot [\mu_m (\nabla \vec{v}_m + \nabla \vec{v}_m^T) + \rho_m \vec{g} + \vec{F} + \nabla \cdot \left(\sum_{k=1}^{n} \alpha_k \rho_k \vec{v}_{dr,k} \vec{v}_{dr,k} \right)$$

(47)

where $\mu_m = \sum_{k=1}^{n} \alpha_k \mu_k$ is the viscosity of the mixture and $\vec{v}_{dr,k} = \vec{v}_k - \vec{v}_m$ is the drift velocity for the secondary phase, k.

The energy equation expresses the energy as a sum of the energies of the mixture.

$$\frac{\partial}{\partial t}(\alpha_k \rho_k E_k) + \nabla \cdot \sum_{k=1}^{n}(\alpha_k \vec{v}_k(\rho_k E_k + p)) = \nabla \cdot (k_{(}eff)\nabla T) + S_E \qquad (48)$$

Where $k_{eff} = \sum_{k=1}^{n} h_k(k_k + k_t)$ is the effective conductivity and S_E is any other volumetric heat sources. For incompressible flows, $E_k = h_k$ and for incompressible flows, $E_k = h_k - p/p_k + v_k^2/2$. h_k is the sensible enthalpy for phase k.

The continuity equation uses a mass-averaged velocity,

$$\vec{v}_m = \frac{\sum_{k=1}^{n} \alpha_k \rho_k \vec{v}_k}{\rho_m} \tag{49}$$

$$\frac{\partial}{\partial t}(\rho_m) + \nabla \cdot (\rho_m \vec{v}_m) = 0 \tag{50}$$

where $\rho_m = \sum_{k=1}^{n} \alpha_k \rho_k$ is the mixture density.

There are three important options for interphase exchange coefficients. The universal method for calculating the drag coefficient was used since it handles bubbly, gas-liquid mixtures very well. Since the mixture model depends on relative velocities of the phases, the slip velocity and drift velocities are important. The slip velocity of a phase is the relative velocity between it and the other phases. The drift velocity is defined as the velocity of a phase relative to the mixture volume centered velocity. Slip velocity is defined for phase p relative to phase q by

$$\vec{v}_{pq} = \vec{v}_p - \vec{v}_q \tag{51}$$

The mass fraction for any phase k is

$$c_k = \frac{\alpha_k \rho_k}{\rho_m} \tag{52}$$

The drift velocity as a function of slip velocity is

$$\vec{v}_{dr,p} = \vec{v}_{pq} - \sum_{k=1}^{n} c_k \vec{v}_{qk} \tag{53}$$

The method chosen to find the interphase velocities was the Manninen method [32]. Liquid vapor mass transfer was handled by the Lee model which is governed by the

vapor transport equation

$$\frac{\partial}{\partial t}(\alpha_v \rho_v) + \Delta \cdot (\alpha_v \rho_v \vec{v}_v) = \dot{m}_{lv} - \dot{m}_{vl} \tag{54}$$

where $\dot{m}_{lv}$ is the mass transfer rate due to evaporation and $\dot{m}_{vl}$ is mass transfer rate due to condensation [30].

All of the options in Table 8 that were set to second order upwind were solved from the cell centers to the faces downstream of the flow. This forces the equations to be solved in the direction of fluid flow. The PREssure STaggering Option (PRESTO!) for pressure interpolation and the Quadratic Upstream Interpolation for Convective Kinematics (QUICK) options both work in most situations, but are particularly effective with structured meshes. They are both second order interpolation schemes.

4.5 QUADRILATERAL RASTER APPROXIMATION

An approximation of the raster motion was made later which greatly reduced the computation time needed for the solution. A close look at the raster motion shows that the beam almost closes a quadrilateral twenty eight times per MPS. The full raster UDF calculates beam heating 1042 times every MPS with 1μs time steps. By increasing the time steps to one twenty eighth of an MPS, 37.2 μs and approximating the beam motion through this time period as rectangles in the xy-plane the computational time can be greatly reduced at the expense of some precision (see Figure 35).

This UDF was more complicated because the beam would not have a circular cross section. The approximation was accomplished by setting x intercept points for one of the lines of the quadrilateral approximation. Because of the symmetry of the quadrilaterals, the equations for all four lines can be calculated for each of the 28 points on the x axis and the slopes of all fours lines was ± 1. These lines approximate the path that the center of the electron beam travels through one twenty-eighth of an MPS. Any element found within the electron beam radius (100 μm) of this
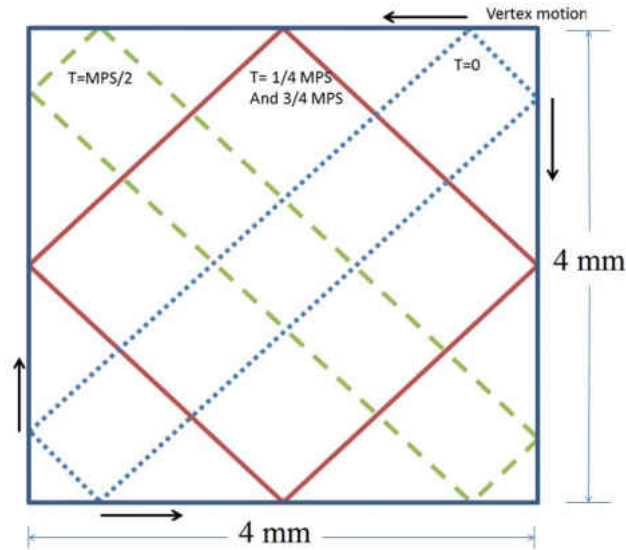
FIG. 35: Quadrilateral approximation of beam raster. The frame represents the 4×4 mm^2 raster area. The first one twenty-eighth of an MPS is represented by the dotted blue line labeled $T = 0$. The width of the lines is the diameter of the intrinsic beam spot. The top vertex then moves to the left while the vertex on the right moves down, effectively opening up the quadrilateral into a square at $T = 1/4MPS$ (red solid line). The top vertex continues to the left, collapsing the square into the green dashed line at $T = 1/2MPS$. the process then goes in reverse.

line is considered "in-beam" and becomes an energy source in the simulation. Each quadrilateral cross section has an area of 2.34×10^{-6} m^2 meaning a total volume of 8.073×10^{-7} m^3.

4.6 GAUSSIAN POWER DEPOSITION AND BEAM JITTER

For both raster UDF's two methods were used to deposit the energy around the beam center. The first was just an approximation of uniform energy deposition up to the "edge" of the beam. The second was a Gaussian heating code. This calculated the distance from the center of the beam to each mesh element to be used for energy deposition and adjusted the energy density so that it created a two dimensional Gaussian distribution around the center of the beam. This was much closer to the actual beam, but in the simulation it made very little difference to either the fluid properties or the noise. Since it increased the number of calculations per time step

without changing the results the first method was used.

One of the additions to the code to make the simulation more realistic was beam jitter. The electron beam current during the Qweak experiment was 180 μA. This value was not steady. Besides beam trips, ramping and other major changes the "steady" beam had current fluctuations on the order of 1%. To mimic this, a random number generator was used to set the current between $I_0(1 - 0.01) < I_{new} < I_0(1 + 0.01)$. To check the current distribution the UDF was set to report the current at each MPS. These values were plotted in histograms to assure an even distribution across the current range.

4.7 ASYMMETRY CALCULATION

An example of the file created by the data writing UDF can be seen in Table 9. The values are averages taken through the beam spot region. For the original model with 1 μs time steps, this meant a cylinder with a radius equal to the radius of the beam spot ($\sim 100\mu$m) and the length of the target. With the quadrilateral approximation the values were averaged over the four lines with beam spot width that make up each rectangle. The simulation results file containing all the values at every time step was analyzed using a ROOT code similar to that used for the Qweak data. The first step was to make averages of the results for every MPS. In both codes there is a variable which represents the fraction of an MPS that timestep represents. For example, in the rectangular approximation each time step is 1/28th of an MPS. This corresponds to 37.202 μs, so this fractional variable has the value 0.0357 at the first time step of each MPS and ~ 1 on the last time step. The ROOT code looked for this change in the fractional value to mark the beginning of each MPS. Once the MPS averages of the values were found, mock helicity patterns were formed and asymmetries calculated. The asymmetry results were then used to fill histograms and the RMS extracted. This resulted in plots of asymmetry widths versus frequency. A detailed description of the code can be found in Appendix 2.

4.8 SIMULATION TIME AND HPC

Flow Time (μs)	4865141	4865178
ρ (kg/m^3)	70.7537	70.7622
k (J/kg)	0.0141528	0.0141546
ϵ (J/kg s)	1.13355	1.13372
v_x (m/s)	0.267963	0.26793
v_y (m/s)	0.0058458	0.00584273
v_z (m/s)	0.00519674	0.00519048
$|v|$ (m/s)	0.268077	0.268044

TABLE 9: Some of the variables recorded with the Fluent UDF. The Table includes two consecutive 37 μs time steps at $\sim$4.8 s of flow time into the simulation.

Simulation time was a critical factor in this work. The goal for simulation time was to solve for one second of flow time in a week. After running several simulations it became clear that at least 3 seconds of flow time was needed to fill the histograms. When the first simulation was run there were six CPU's available. The time it took to solve one iteration was between five and ten seconds. Each time step consists of between five and twenty iterations. At this rate with the 1 μs time step it would take ~ 290 days to complete 1 second of fluid flow. In March 2014 the Computational Fluid Dynamics group at JLab purchased a license to use 128 cores and housed the license at the ODU High Performance Computing (HPC) cluster [33]. The 128 CPU's were supported by six GB of RAM per CPU. Figure 36 shows the first speed test done with the HPC cluster. The black points show the expected behavior inferred from the Ansys literature on parallel computing. It is essentially linear up to 50 CPU's and after that the gains are not as large for addition CPU's. The erratic behavior for greater than 50 CPU's led to much discussion with the HPC staff, and the problem was never completely solved. Each time a job is submitted it is assigned servers and CPU's and the combination is different every time, leading to different solver speeds. The seconds per iteration reported by Fluent can vary as much as 50%. Once a job was submitted and running on the cluster the solver speed could be checked in one of the log files written in the folder where the job resides. The speed would be checked soon after submission and if the speed was unacceptable, it could be stopped and resubmitted. This only needed to be done ten or so times out

of hundreds of simulations run. When jobs are submitted to the cluster, a journal file is used to issue commands to Fluent when it is running. The HPC cluster has worked very well, but there have still been crashes and loss of simulation results. To protect the simulation results, the journal file ran the simulation for ten thousand time steps and then saved the simulation to a backup file. The simulation would the continue for another ten thousand time steps and save again. Typically this would be done ten times corresponding to 3.7 seconds of flow time. This resulted in ten thousand time steps being the maximum amount of simulation results that could be lost.

4.9 CFD ERROR ANALYSIS

Uncertainty and error are terms which are often used interchangeably. There is a difference which is pointed out in the American Institute of Aeronautics and Astronautics (AIAA) Guide For The Verification And Validation of Computational Fluid Dynamics Simulations [34]. Uncertainty is defined as a potential deficiency in a simulation, while the error is defined as a recognizable deficiency. This wording implies that uncertainty is used for deficiencies introduced by a lack of knowledge. Turbulence modeling falls in this category. It was suggested that the model be run with multiple different turbulence models and comparisons made to determine the sensitivity of the simulation results to a change in model. This was not done, and all the results are from the Realizable $k - \epsilon$ turbulence model. Errors on the other hand are able to be identified when the results and model are studied. Errors can be categorized as either acknowledged or unacknowledged. Acknowledged errors have procedures available to identify and remove them from the final results, while unacknowledged errors do not have such procedures. Included in the acknowledged error category are modeling errors, computer round-off, spatial and temporal convergence error. Unacknowledged errors include computer programming and user errors. The most important error types for this simulation are spatial and temporal discretization errors. To examine the spatial convergence error it is necessary to perform the simulation on two or more successively finer grids. Excluding computer round-off
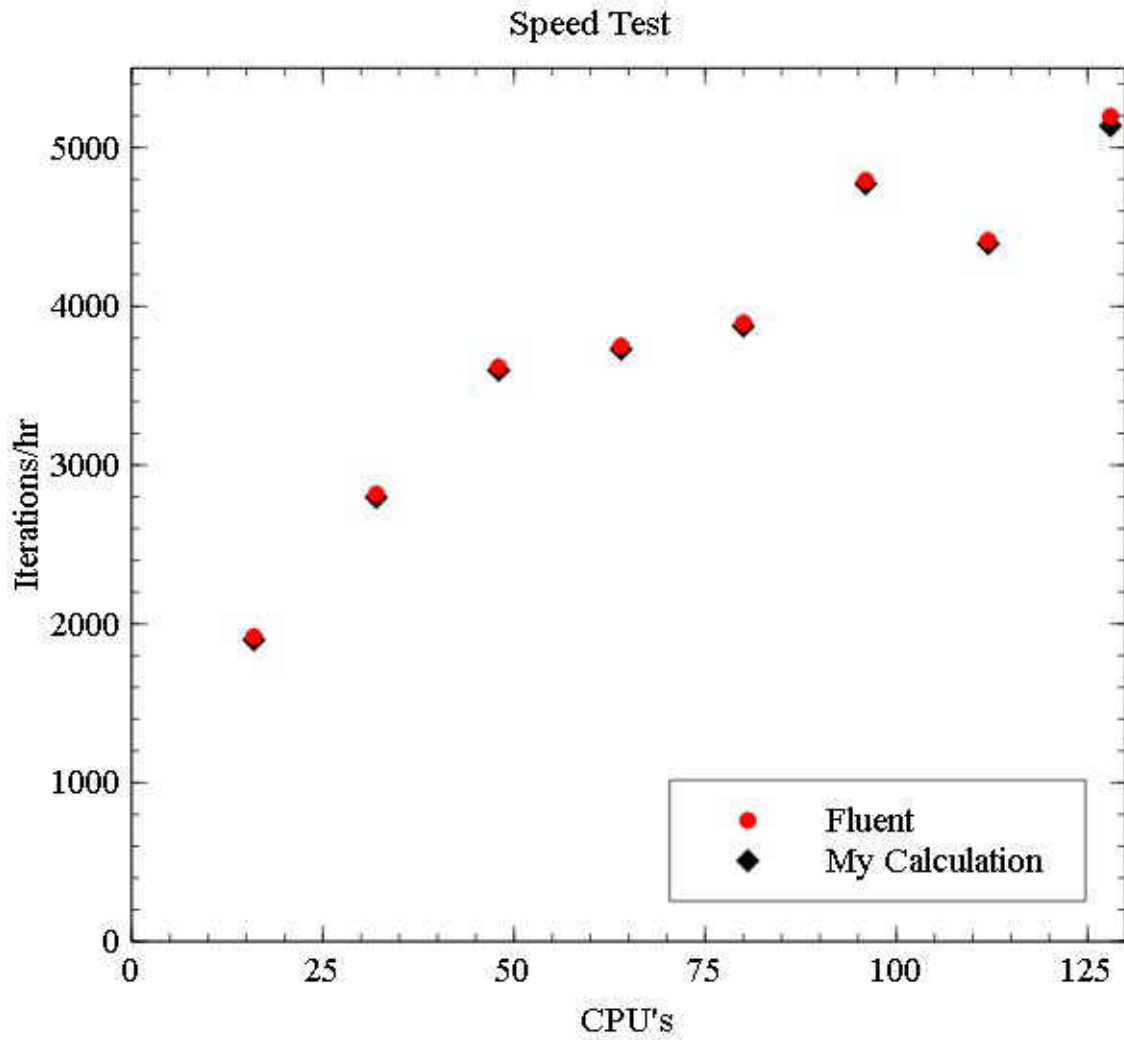
FIG. 36: The same simulation was run eight separate times with different numbers of CPU's for one hour. Fluent reported the speed in seconds per iteration, and a hand calculation was also performed to compare.

errors, smaller grid size should reduce the spatial convergence error asymptotically towards zero. Error of this type is defined as the difference between the exact solution and the simulated one. The method of choice to find the exact (continuum) value is called Richardson Extrapolation [13]. When varying grid sizes, it is not necessary to increase or decrease the number of cells by a factor of two. This is called non-integer grid refinement. It is important to keep the original mesh generation parameters while creating a coarser or finer grid. A simulation yields a quantity U which may be expressed in the series expansion

$$U_1 = U_{h=0} + C_1 h_1 + C_2 h_1^2 + C_3 h_1^3 + ... \tag{55}$$

where h_1 is the grid spacing and C_n are constants which are independent of grid spacing. The Richardson Extrapolation is meant to determine the value of the extrapolated exact solution, $U_{h=0}$. A second simulation with a different grid spacing, $h_1 > h_2$ yields

$$U_2 = U_{h=0} + C_1 h_2 + C_2 h_2^2 + C_3 h_2^3 + ... \tag{56}$$

To first order, the constant C_1 can be found by subtracting the two equations.

$$C_1 \approx \frac{U_1 - U_2}{h_1 - h_2} \tag{57}$$

Substituting this into the first equation and solving for $U_{h=0}$ yields

$$U_{h=0} \approx U_1 + \frac{U_1 - U_2}{r - 1} \tag{58}$$

where $r = h_2/h_1$ is the grid refinement ratio. This can be generalized for any nth order as

$$U_{h=0} \approx U_1 + \frac{U_1 - U_2}{r^n - 1} \tag{59}$$

In practice, the Richardson Extrapolation when used with CFD is performed with

grid refinement ratios of $r = 2$ and with second order, $n = 2$. In this case

$$U_{h=0} \approx \frac{4}{3}U_1 - \frac{1}{3}U_2 \qquad (60)$$

This can be done with more than two grid points as well. The difference between the value obtained with the mesh of interest and the extrapolated value is a good approximation of the spatial convergence error. This analysis was done using the standard model described above with mesh sizes in the beam volume changed from 100 μm to 200μm and the parameter used was the asymmetry RMS width. The temporal discretization could not be used with the raster pattern UDF because it would also include other changes to the model such as beam spot size and the time-domain resolution in the asymmetry calculation. For this reason, the temporal error was determined using the average density in the entire raster volume of LH2 through the target. The procedure involved first getting a steady state solution and then running the models for one second of flow time with timesteps varying between 1 ms and 100 ms. The Richardson Extrapolation was done to these values under the assumption that the smaller the time step, the more precise the solution. The difference between this and the value for the time-step size used to simulate the raster pattern is the temporal error.

ρ error source	value $[\text{kg/m}^3]$
Spatial Convergence	0.010
Temporal Convergence	0.009
Coding	0.002
Total	0.021

TABLE 10: CFD errors for density in the Fluent simulation results

Several unit test models were run when the investigation began and whenever new UDF's were tested to verify Fluent's consistency. The first tests were simple models that had experimental and simulated results to compare with the output from Fluent. The first of these can be found online at Ansys in the tutorial section. The later models generally took the form of a parallelepiped the same size as the total raster pattern in the Qweak target. In these the inlet was one long side (upstream

Pattern Frequency [Hz]	RMS Error [ppm]
480	0.02
240	0.06
120	0.3
96	0.5
80	0.7
60	1.3
48	1.5
40	1.5
30	2.2
15	4.3

TABLE 11: Histogram RMS errors reported by ROOT for the nominal case

from the interaction region) and the outlet was the opposite side (see Figure 37). These were used to verify that Fluent is able to reproduce the raster pattern and
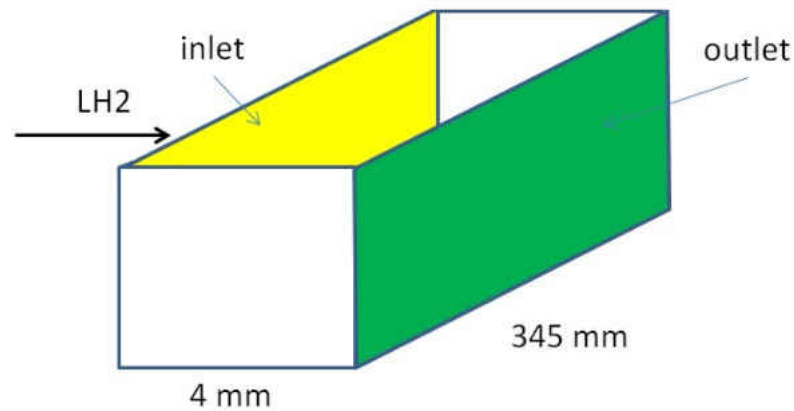
FIG. 37: Diagram of the unit test model used to test raster motion and beam interaction volume. The LH2 moves from left to right.

heat deposition successfully. These models were also important for checking the beam spot size and total volume of the interaction region. The volumes were very close to the calculated value, but there was some discrepancy in the final model and is listed in Table 10 along with round-off error in the code as "coding error". These errors are added to the histogram fitting error reported by ROOT. An example can be seen in Table 11.

4.10 ONE-TENTH SCALE MODEL

The full size model proved too slow to search effectively for a comparison to the Qweak data and the simulation results. One full size model ran for two months and returned only enough density values to fill histograms for the highest two frequencies. One method of speeding up the simulation time was to down-scale the spatial size of the model to one tenth it's original size ("One Ten" model). The spatial dimensions of the model were scaled to one tenth the original size. This decreased the time Fluent required for each time step from minutes to seconds and allowed many models to be run in the time it would have taken to run one full-size model. All the other parameters were left as they were in the full size model. All of the following results in Section 5.2 are from the One Ten model.

Parameter	Full-size	One Ten
Target Length	34.5 cm	3.45 cm
Beam radius	0.01 cm	0.001 cm
Raster area	4×4 mm	0.4×0.4 mm
Al window thickness-beam in	0.1 mm	0.01 mm
Al window thickness-beam out	0.127 mm	0.0127 mm
$\dot{m}$	1 kg/s	.001 kg/s
Power deposited in LH2	2140 W	214 W
Power deposited in Al	25 W	2.5 W

TABLE 12: Parameters scaled by a factor of 1/10 for the One Ten model. The values for power deposition are calculated from Equation 11 with $l' = l/10$.

CHAPTER 5

RESULTS AND INTERPRETATION

5.1 QWEAK RESULTS

The σ_{tgt} values from the production runs (at close to nominal parameters) of the Qweak experiment that were analyzed can be seen in Figures 38 to 42 and a table of the important values in Table 13. σ_{tgt} was found using the method in Chapter 3 and includes counting statistics calculated with the GEANT simulated detector rate. The values for σ_{tgt} at the pattern frequency of 480 Hz are relatively consistent, but the fit parameters, a, b, and c, are not. The fit parameters are for the equation

$$\sigma_{tgt} = \sqrt{\frac{a^2}{f_p^b} + c} \tag{61}$$

where σ_{tgt} is in ppm, and f_p is the pattern frequency in Hz. This is based on the pink noise spectrum $(1/f^a)$ found widely in nature [35] and used to characterize the boiling spectrum of the Qweak target from different orderings of helicity states in 2014 [23]. The parameter c was included to define any constant offset between the values of σ_{tgt} from the Qweak experiment and σ_ρ from simulations.

Run number	I_{beam} [μA]	f_{pump} [Hz]	$\sigma_{tgt}[ppm](480Hz)$	a	b	c
11740	166	28	56.84	891	0.166	-476
12160	177	29	44.95	961	0.188	-491
12080	179	30	52.77	1378	0.103	-949
18440	176	30	34.01	1440	0.109	-996
17245	176	30	33.30	913	0.300	-329

TABLE 13: Data from Qweak σ_{tgt} analysis for runs at close to nominal values. The parameters a, b, and c are for the fit to Equation 61.

The ROOT files for the target boiling study at the end of Run 1 were also analyzed. These files contained runs with three parameters varied: Beam current, LH2
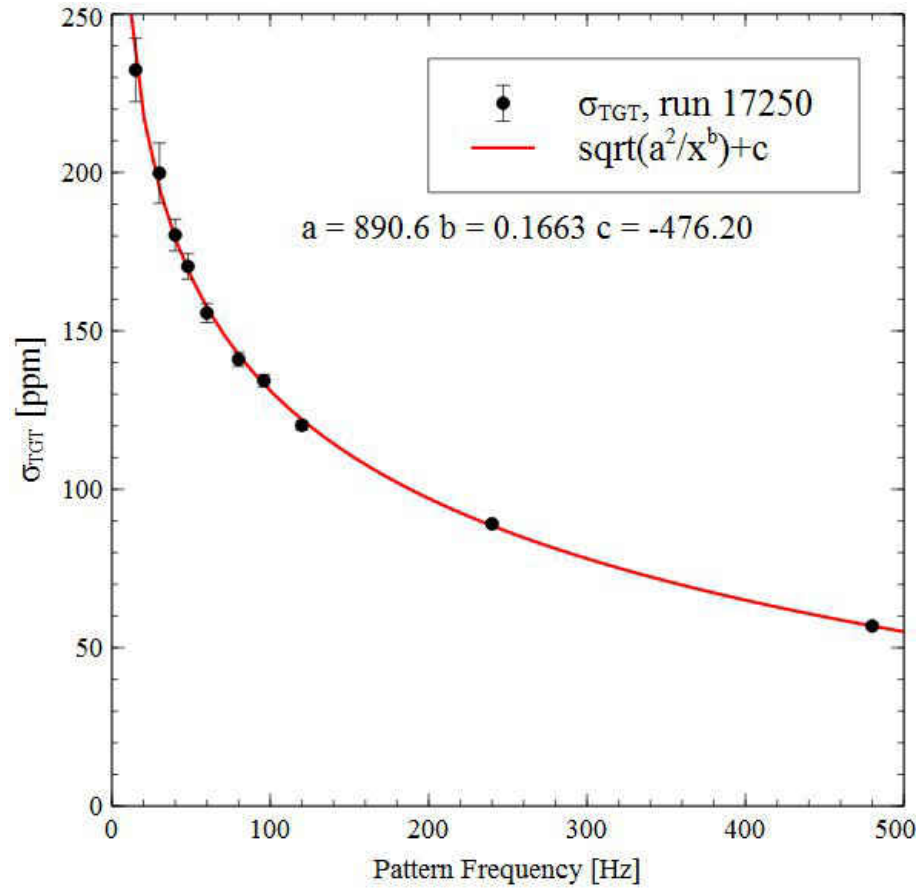
FIG. 38: σ_{tgt} for run 11740. Beam current= 166 μA, LH2 pump frequency =28 Hz.
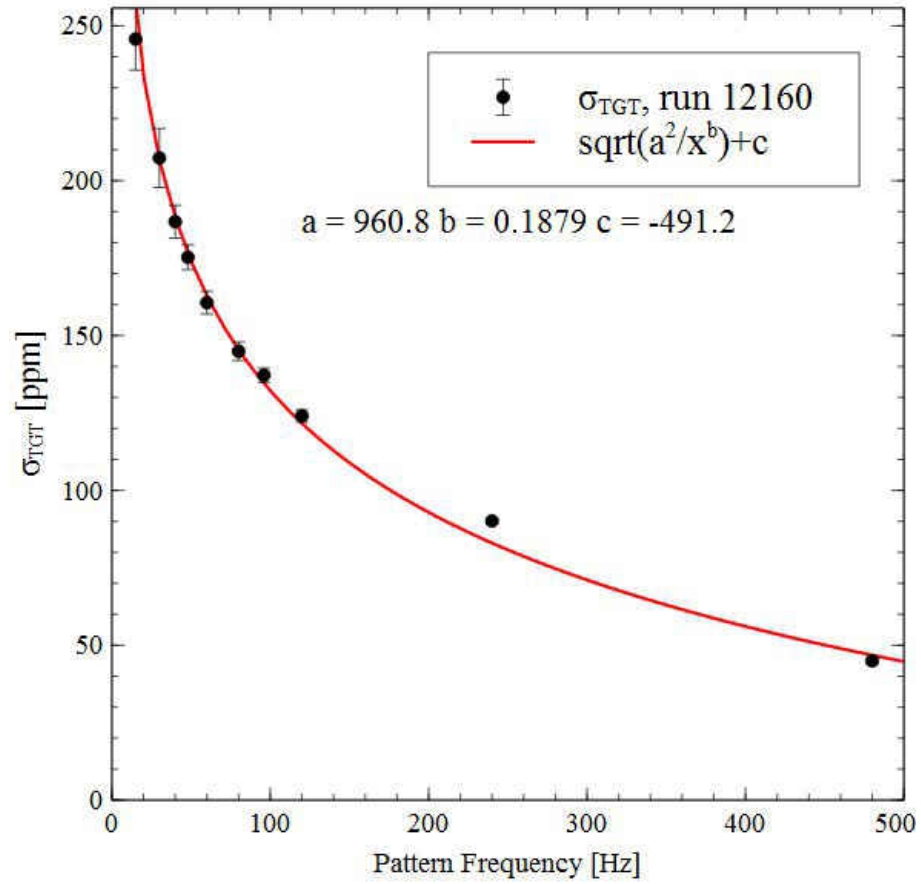
FIG. 39: σ_{tgt} for run 12160. Beam current= 177 μA, LH2 pump frequency =29 Hz.
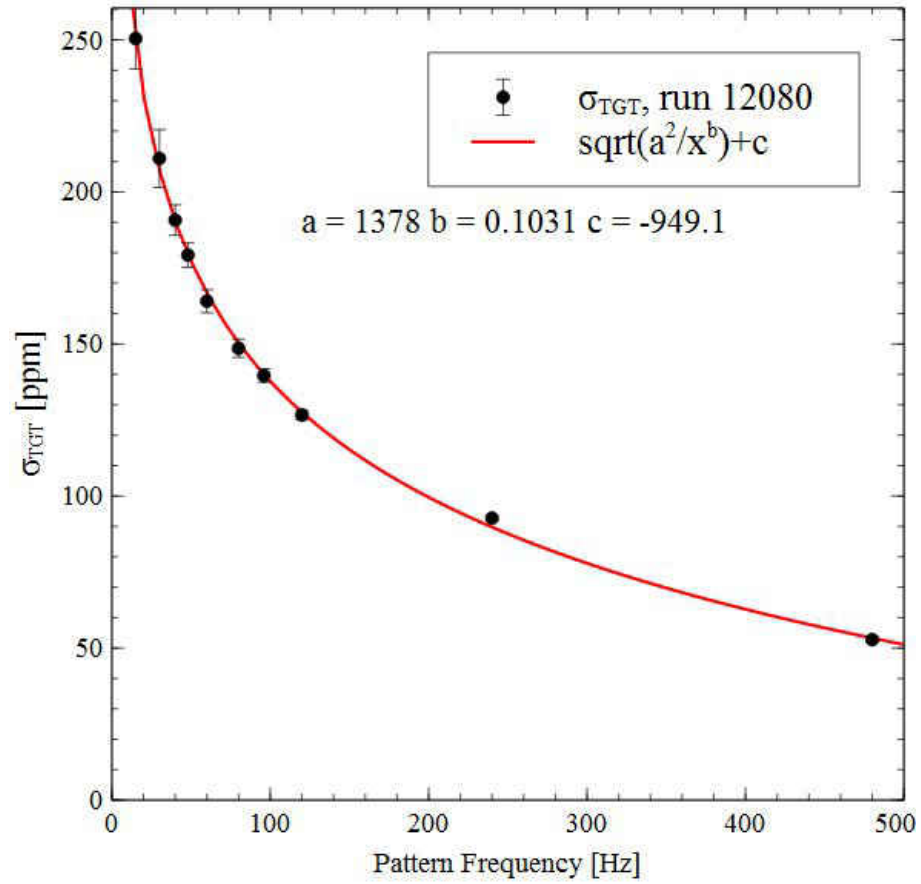
FIG. 40: σ_{tgt} for run 12080. Beam current= 179 μA, LH2 pump frequency =30 Hz.
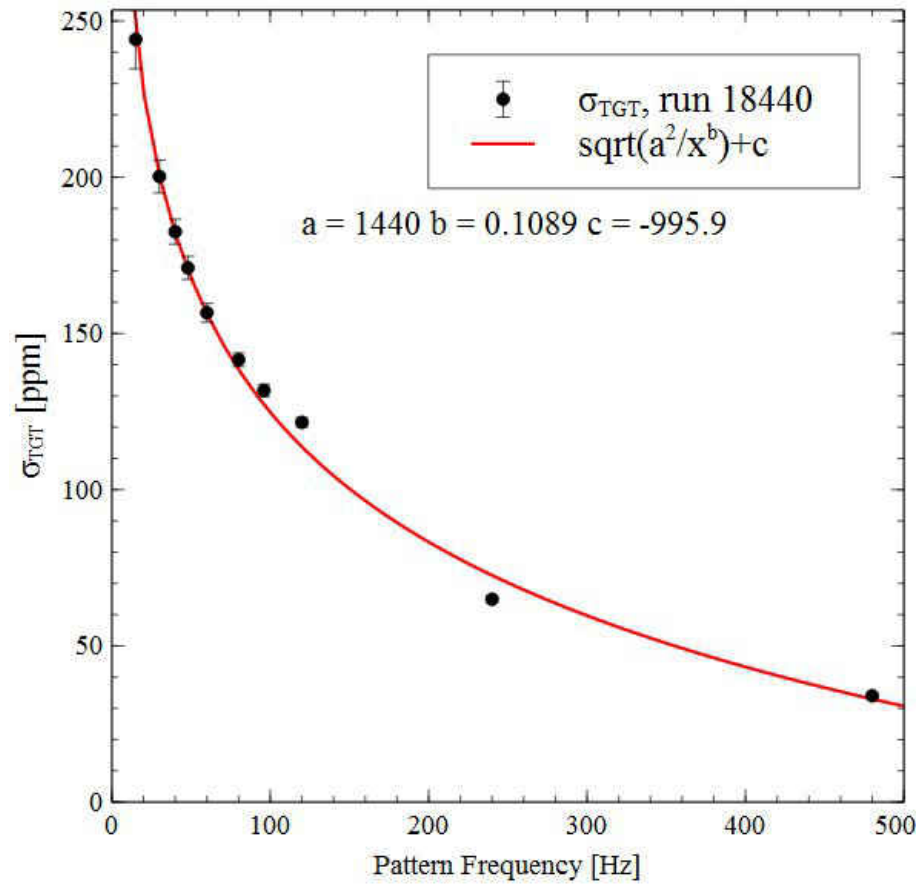
FIG. 41: σ_{tgt} for run 18440. Beam current= 176 μA, LH2 pump frequency =30 Hz.
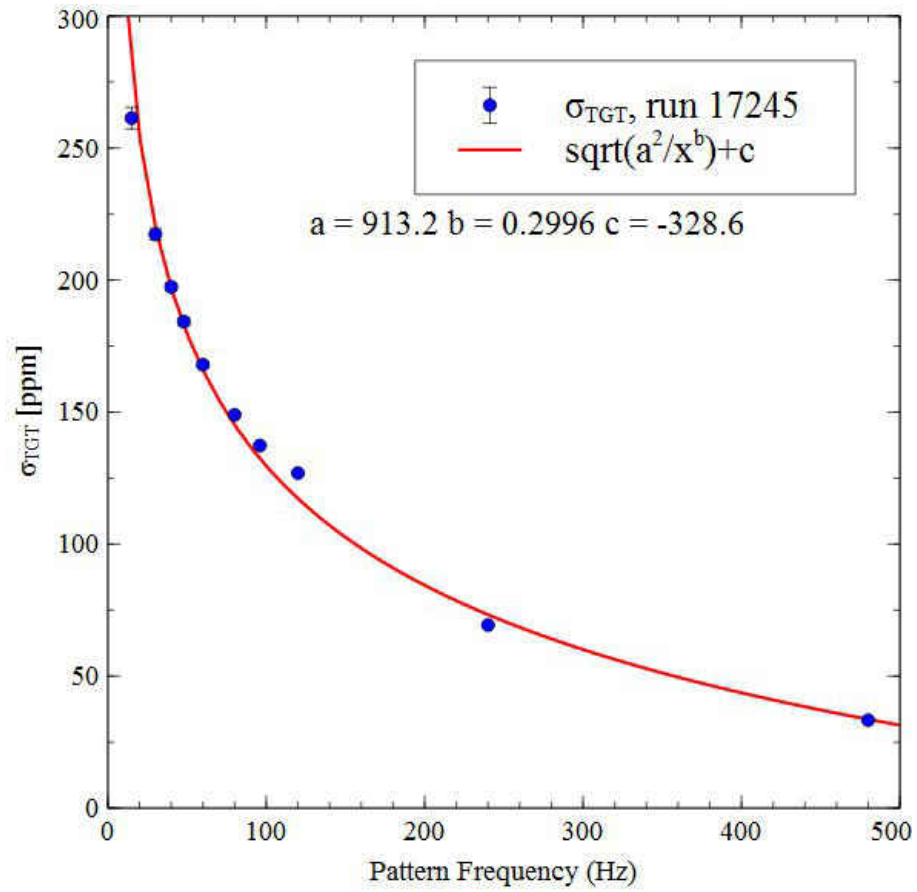
FIG. 42: σ_{tgt} for run 17245. Beam current= 176 μA, LH2 pump frequency =30 Hz.

pump frequency, and raster size. Only the runs with varying beam current and pump speed were to be simulated with CFD so the runs with varying raster size were ignored. The only runs that were easily available with varying current with pump speed and raster size constant were at f_{pump}=30 Hz and raster size of 3×5 mm. These results with varying currents can be seen in Figure 43. The lines connecting the data points are there to guide the eye to the anomaly at 240 Hz pattern frequency. The values at 480 Hz, the nominal quartet frequency, are higher than expected but they increase with increasing current as expected. Many attempts were made to fit the individual data sets, including cutting all the data points from 80-240 Hz. The fits were poor (reduced $\chi^2 > 50$) and the fit parameters were not consistent. The Qweak log books [28] for one of these runs mention that there were some issues with the BCM's during these runs.

The data from varying the LH2 pump frequency is shown in Figure 44. The anomaly at 240 Hz is not there for these runs but the fits to Equation 61 were very poor. The values at the lowest pattern frequency, 15 Hz, at 12 Hz LH2 pump frequency are more than twice the value for the nominal case.

5.2 CFD RESULTS

All of the following results were simulated on the One Ten scale model (See Section 4.10). The conditions of the simulated target are given in the values of the corresponding full size model, ie 30 Hz pump in the simulation means $\dot{m} = 0.001$ kg/s.

The temperature profile of the solution in the xz-plane can be seen in Figure 45. This is at nominal conditions; 30 Hz fan, 180 μA beam current. The simulation had run for 2 seconds of flow time ($\approx$ 2000 MPS or 56,000 timesteps). The temperature scale on the left has been reduced to $20 < T < 22$ K. This scale captures everything but a small area directly adjacent to the windows. A beam axis view of the wall temperature of the target can be seen in Figure 46. The temperature scale in this plot is also $20 < T < 22$ K. The area of the beam spot which is > 22 K is removed. A closeup of the LH2 at the beam out window can be seen in Figure 47. The hot
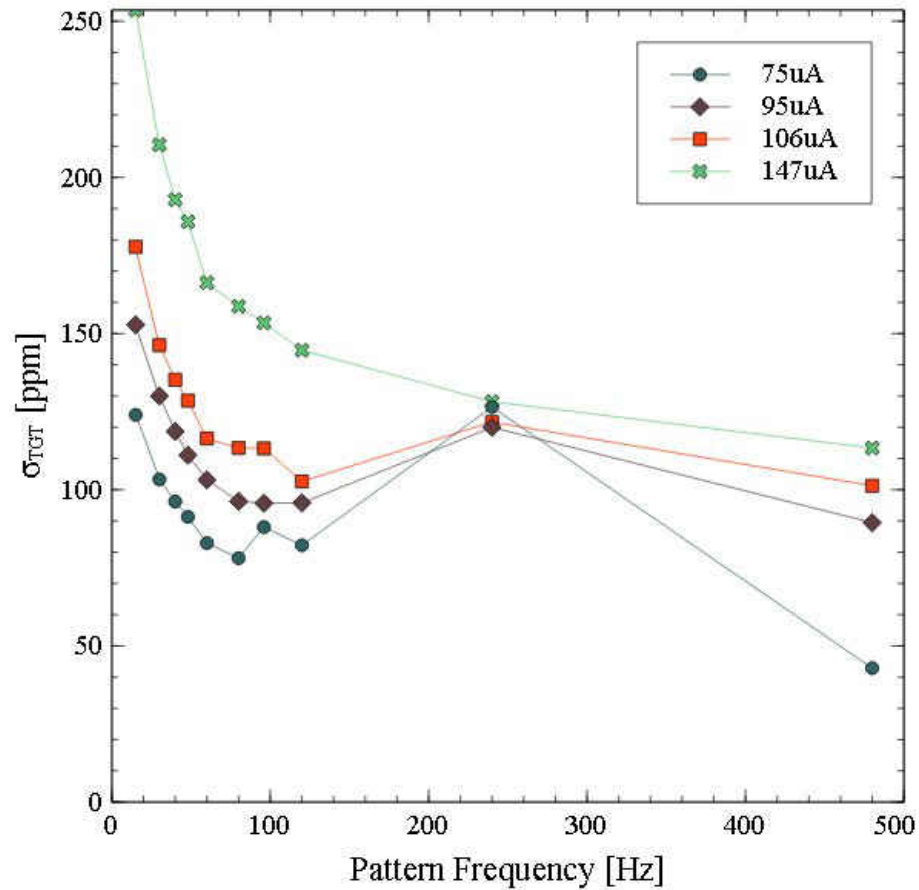
FIG. 43: σ_{tgt} results for the target boiling runs that varied beam current with LH2 pump frequency= 30 Hz and raster dimensions of 3×5 mm at the end of Run 1. The lines are just to aid in viewing. Note the anomaly at 240 Hz pattern frequency. Error bars have been suppressed.
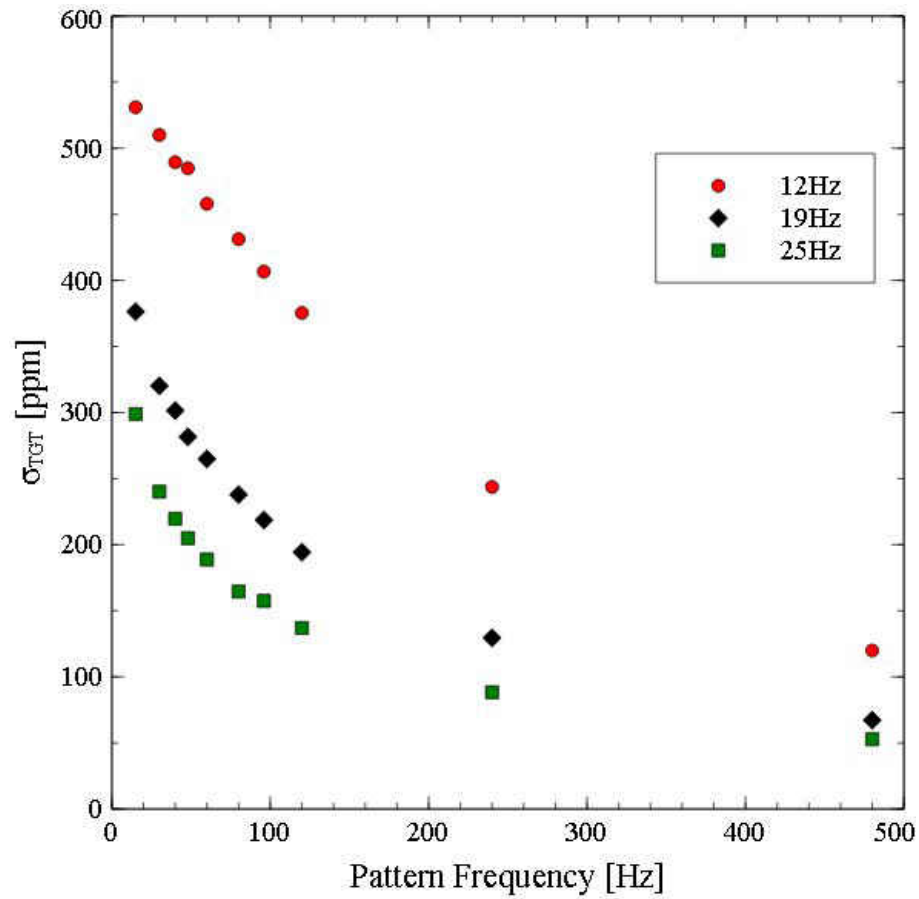
FIG. 44: σ_{tgt} results for the target boiling runs that varied LH2 pump frequency with beam current= 170 μA and raster dimensions of 3×5 mm at the end of Run 1. Note the high value of σ_{tgt} at $f_{pump} = 12$ Hz. Error bars have been suppressed.

square in the center of the figure is the aluminum beam out window and it is bisected by the fluid in the xz-plane.

The beam nipple temperature in Figure 47 shows a tilted hourglass pattern in the aluminum window from the raster motion. This was seen many times in investigating the raster motion. Four times every MPS, the beam spot motion would result in two successive turns close to the corner of the 4×4 mm^2 square. This meant that the beam lingered in the corner for a slightly longer time and the resulting heat increase in adjacent corners produced this hourglass shape. The hourglass was mirrored in the x-plane halfway through one MPS. This can be seen in Figure 48.
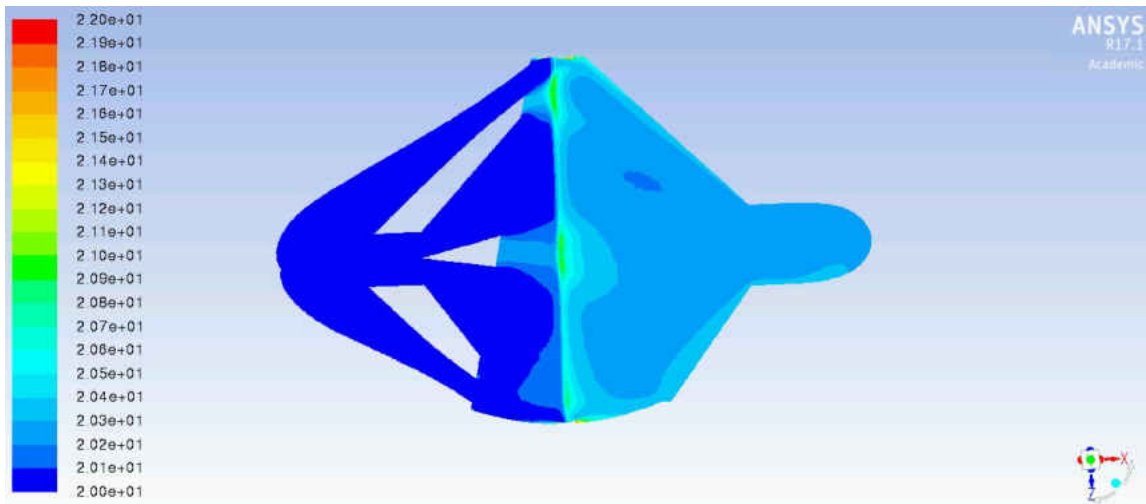
FIG. 45: Temperature in the xz-plane through the center of the cylindrical cell as simulated by Fluent. The fluid flow is from left to right.

The asymmetry width versus frequency plot made from the Fluent simulation results can be seen in Figure 49. This situation is the default stated above, 180 μA and 30 Hz pump. These are the same parameters in the case shown in Chapter 2 and the behavior of the asymmetry widths as a function of pattern frequency should show the same dependence on frequency.

Similarly in Figures 50 to 52 the asymmetry widths can be seen for four different beam current values. Four separate currents were investigated. In addition to the nominal 180 μA, 160 μA, 200 μA and 360 μA were simulated with the pump speed set at 30 Hz. Figure 49 is the simulation with nominal parameters.
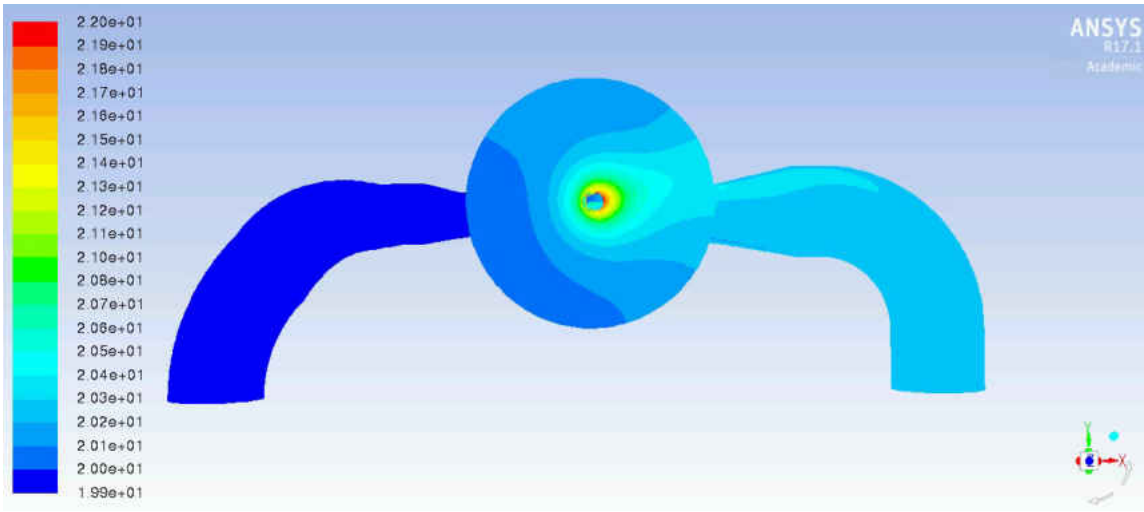
FIG. 46: Wall temperature on the beam exit side of the Qweak cell from the simulation results. Fluid flow is from left to right. The dark blue represents ≈ 20 K and beam spot has been removed by setting the scale to exclude anything over 22 K.
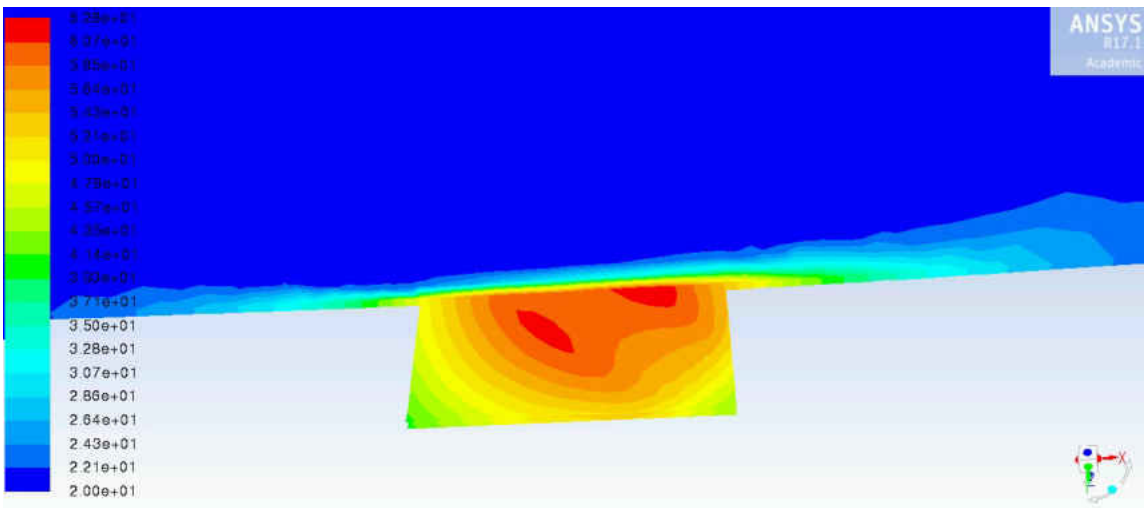
FIG. 47: The temperature in the xz plane up to the beam out wall of the cylindrical cell. The square is one half of the 0.4×0.4 mm beam out window. The scale is from 20 to 62.8 K.
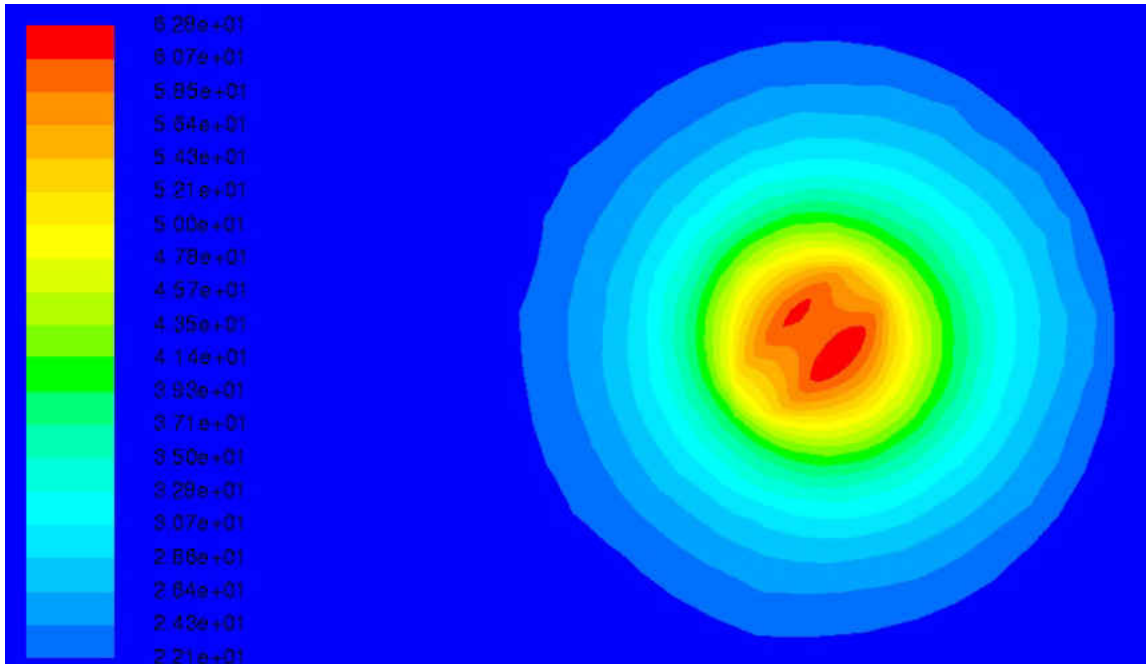
FIG. 48: Close up of the beam out window showing the temperature half way through a Lissajous pattern. The temperature scale is 22.1 to 62.8 K.

In Figures 53 to 54 the asymmetry widths for two different LH2 pump speeds can be seen. The beam current is 180 μA for all these results. The case with a pump speed of 30 Hz is the same as Figure 49 since it is the nominal case.

Two heating sources were separated to examine their contribution to the overall target noise. The first source was called bulk heating. This is defined as the power deposition in the LH2 through the beam interaction volume with no power deposition in the aluminum windows. The power deposition in the windows accounts for the other and is called wall heating. In the Figures 56 to 57, three heating situations are shown at each current setting. In addition to only the heating at the windows ("No Bulk") and only the heating in the bulk ("No Wall"), the full case with both is also shown. The vertical axis is logarithmic because the "Full" and "No Wall" results were almost identical. From these plots it appears that the majority of the density fluctuations are coming from the "Bulk" and the boiling at the windows accounts for a small fraction of the total asymmetry widths.

Figures 58 through 62 show the temperature, density and LH2 velocity in the entire raster volume as a function of z[m], the distance through the target from entrance to exit window. The temperature and density are shown for both the diffuse beam (no raster motion) and the rastered beam. The velocity is the same for both situations. It is clear that the only place a phase transition occurred was at the windows since the temperature of the fluid between them never reached the saturation point of 23.7 K (Figures 58 and 61). The velocity of the fluid (Figure 60) is the same in both the rastered and nonrastered cases. It is largest at the windows and lowest between the two central manifold inlets to the cylindrical cell. Where the velocity is lowest, the density is also low.

Over twenty simulations with different input parameters were run and the values of the fit parameters and the values of the asymmetry RMS can be seen in Table 14. All the simulations returned asymmetry widths which were roughly a factor of a hundred less than the Qweak results. Over fifty simulations were run with short flow times (1 second) looking for a factor of ten (at least) raising of the σ values at 480 Hz pattern frequency. Only a couple of times was this possible and the parameters led to a target that did not have the same behavior as Qweak; the temperature difference was far too high or low, the flow patterns were not physical, ect.

There was some consistency with the value of the σ's for varying current. The values increased with increasing current, but the fit parameters (an indication of the behavior at different time scales) were not. From Figures 53 and 54 it is clear that varying the LH2 pump speed below the nominal value of 30 Hz also led to inconsistent results. As a comparison, the values for σ from the CFD simulations was multiplied by a constant so that the value at 480 Hz matched the value for $sigma$ from the Qweak data. The multiplier was 98 and the comparison plot can be seen in Figure 63. It is clear that the noise in the CFD model grows much faster than the Qweak data as the pattern frequency decreases.

5.3 SUMMARY

This study was meant to provide a path to better target design in future parity
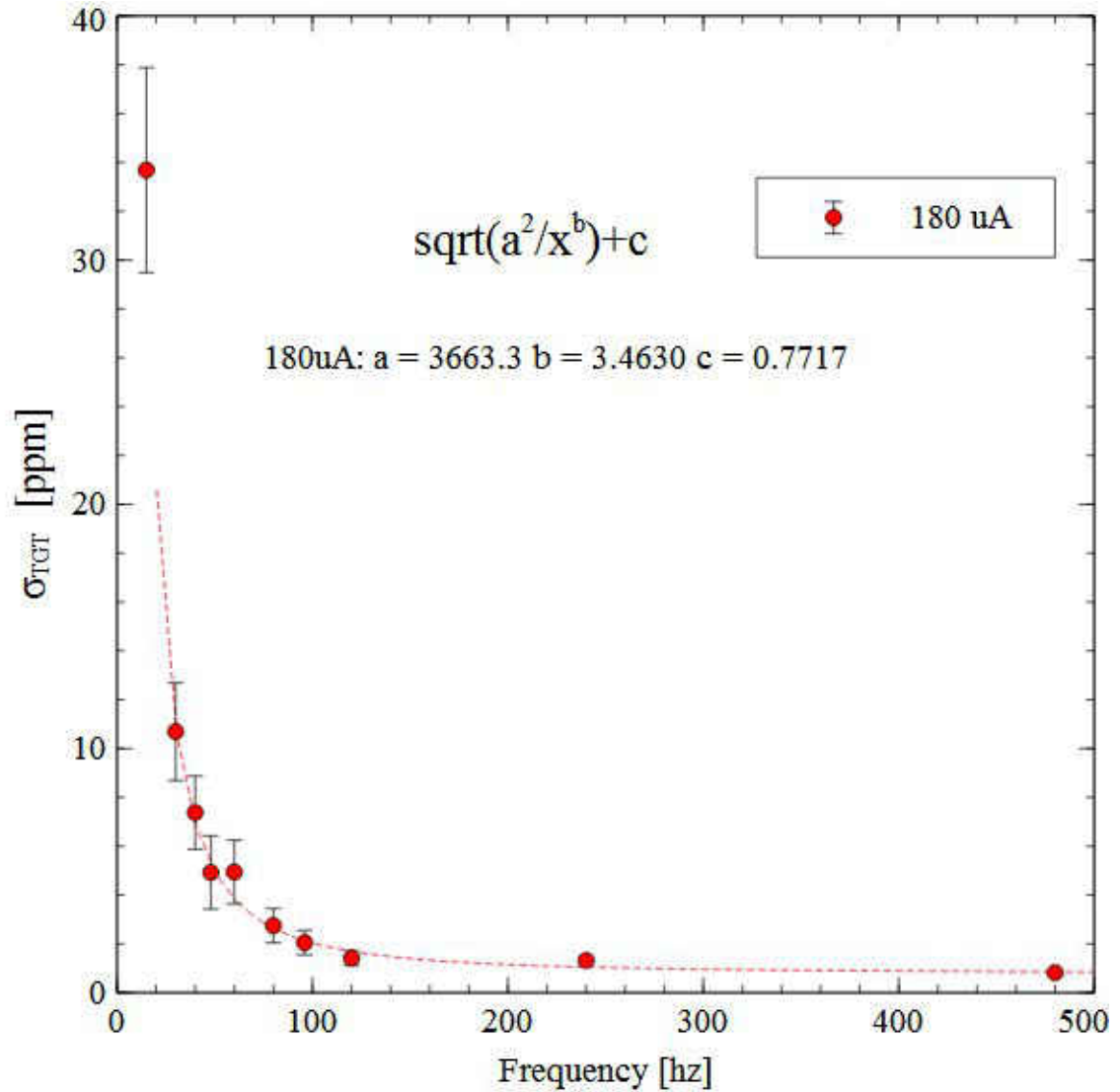
FIG. 49: Beam current=180 μA, Pump frequency=30 Hz. Density asymmetry width versus frequency for the mock helicity patterns in the Fluent density simulation results. Each data point is the statistical width of a histogram filled with the value of the asymmetry for patterns corresponding to the frequency.
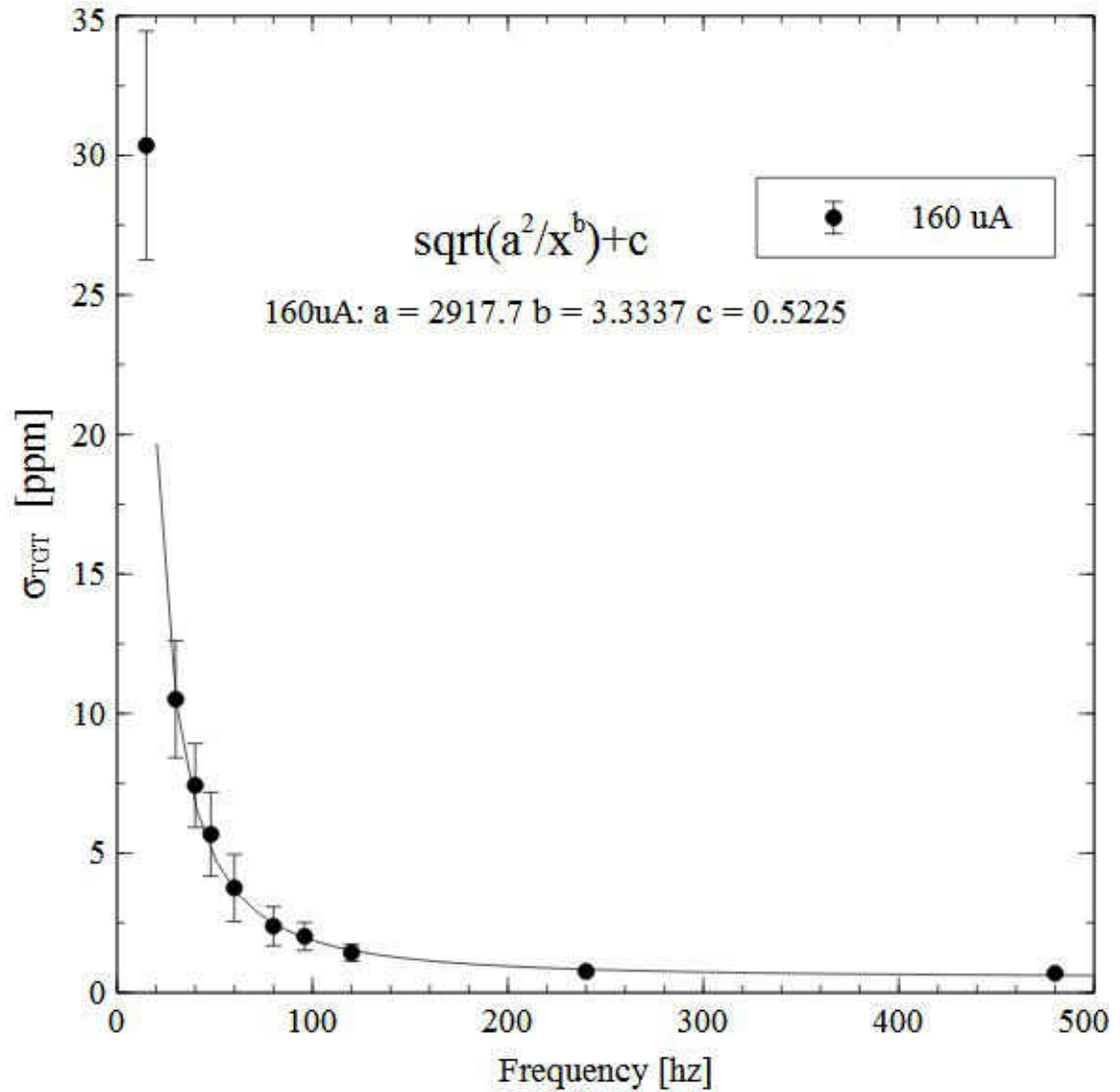
FIG. 50: Beam current=160 μA, Pump frequency=30 Hz. Density asymmetry width versus frequency for the mock helicity patterns in the Fluent density simulation results. Each data point is the statistical width of a histogram filled with the value of the asymmetry for patterns corresponding to the frequency.
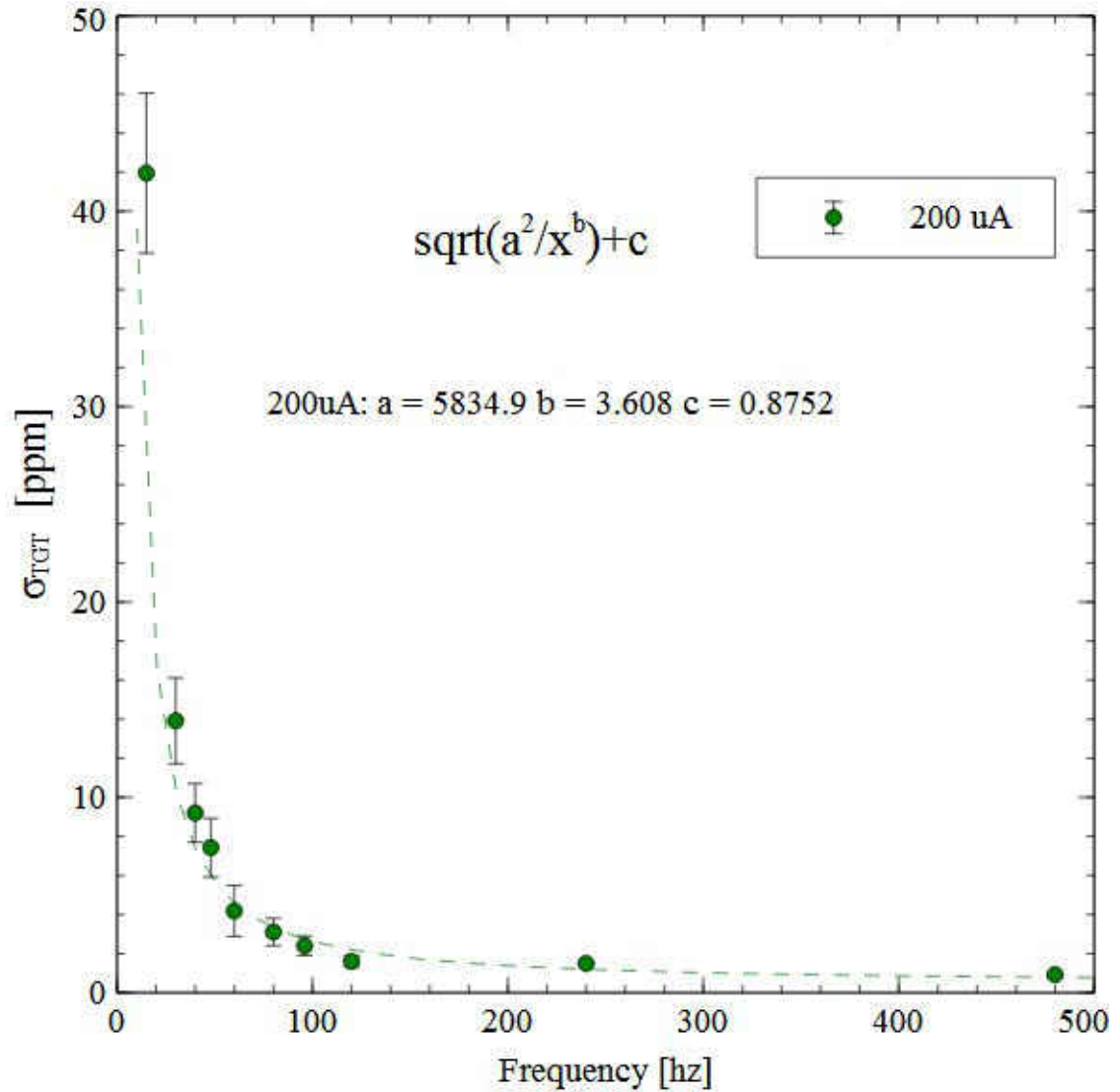
FIG. 51: Beam current=200 μA, Pump frequency=30 Hz. Density asymmetry width versus frequency for the mock helicity patterns in the Fluent density simulation results. Each data point is the statistical width of a histogram filled with the value of the asymmetry for patterns corresponding to the frequency.
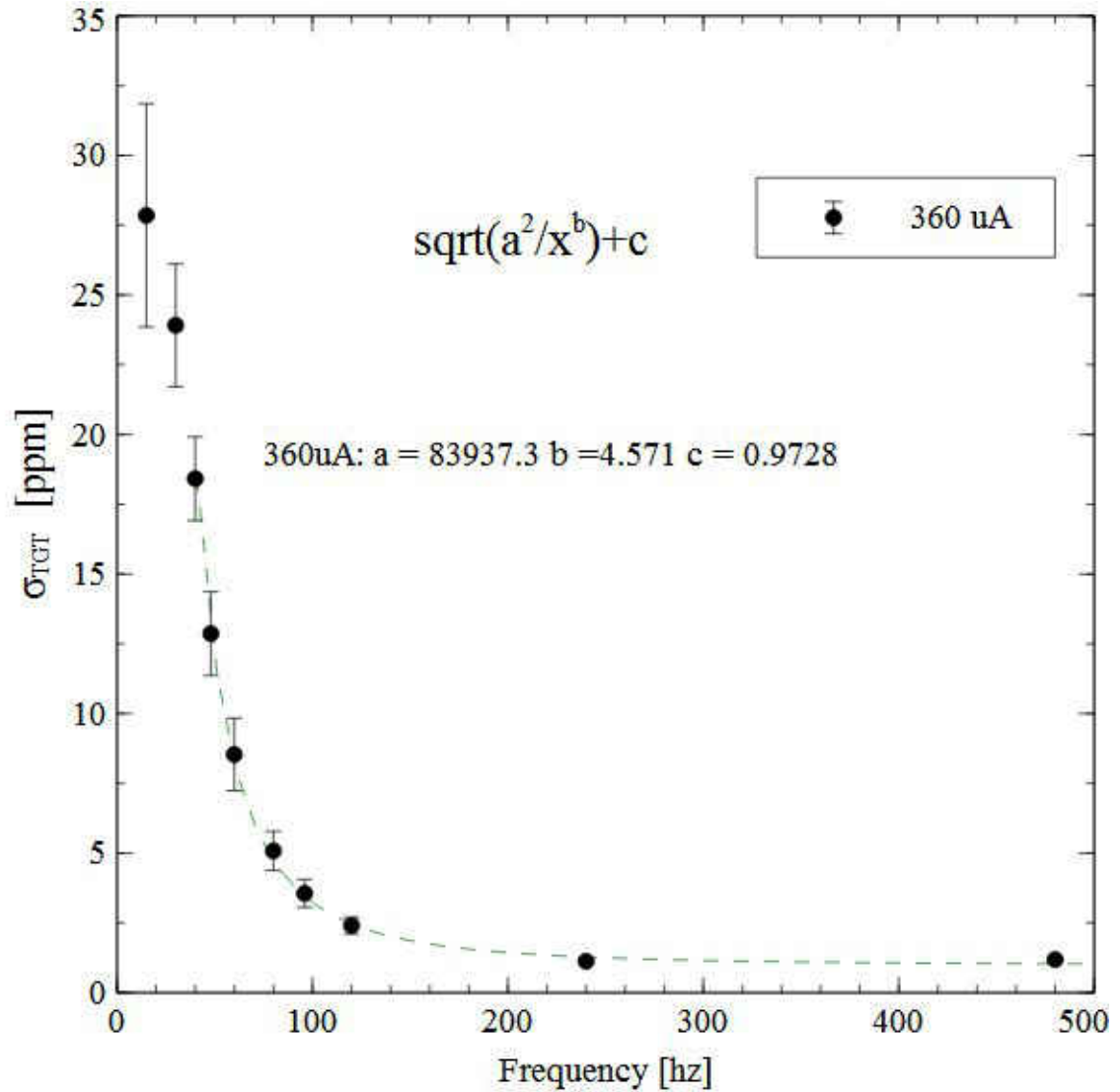
FIG. 52: Beam current=360 μA, Pump frequency=30 Hz. Density asymmetry width versus frequency for the mock helicity patterns in the Fluent density simulation results. Each data point is the statistical width of a histogram filled with the value of the asymmetry for patterns corresponding to the frequency.
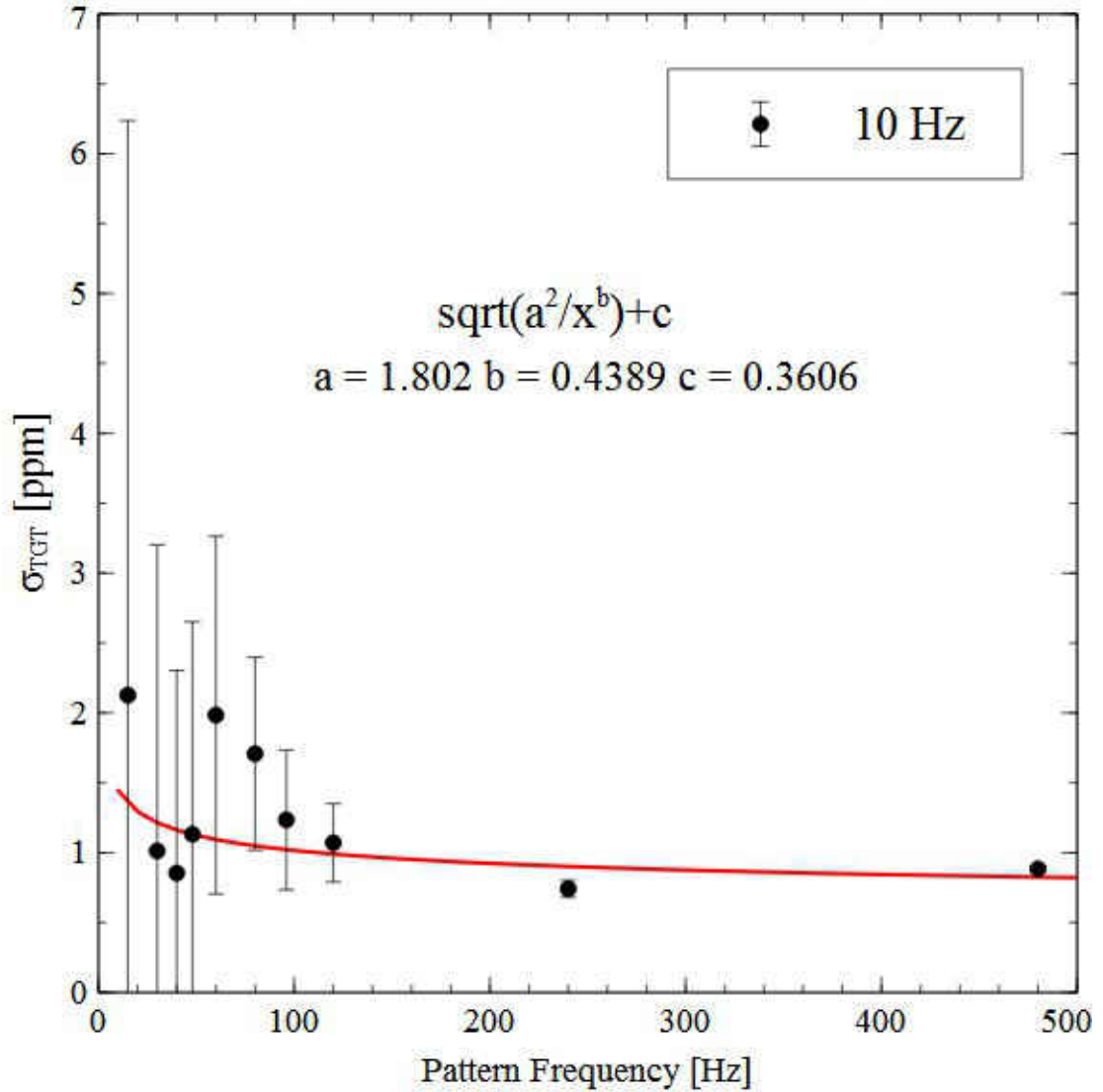
FIG. 53: Pump frequency=10 Hz, Beam current=180 μA. Density asymmetry width versus frequency for the mock helicity patterns in the Fluent density simulation results. Each data point is the statistical width of a histogram filled with the value of the asymmetry for patterns corresponding to the frequency.
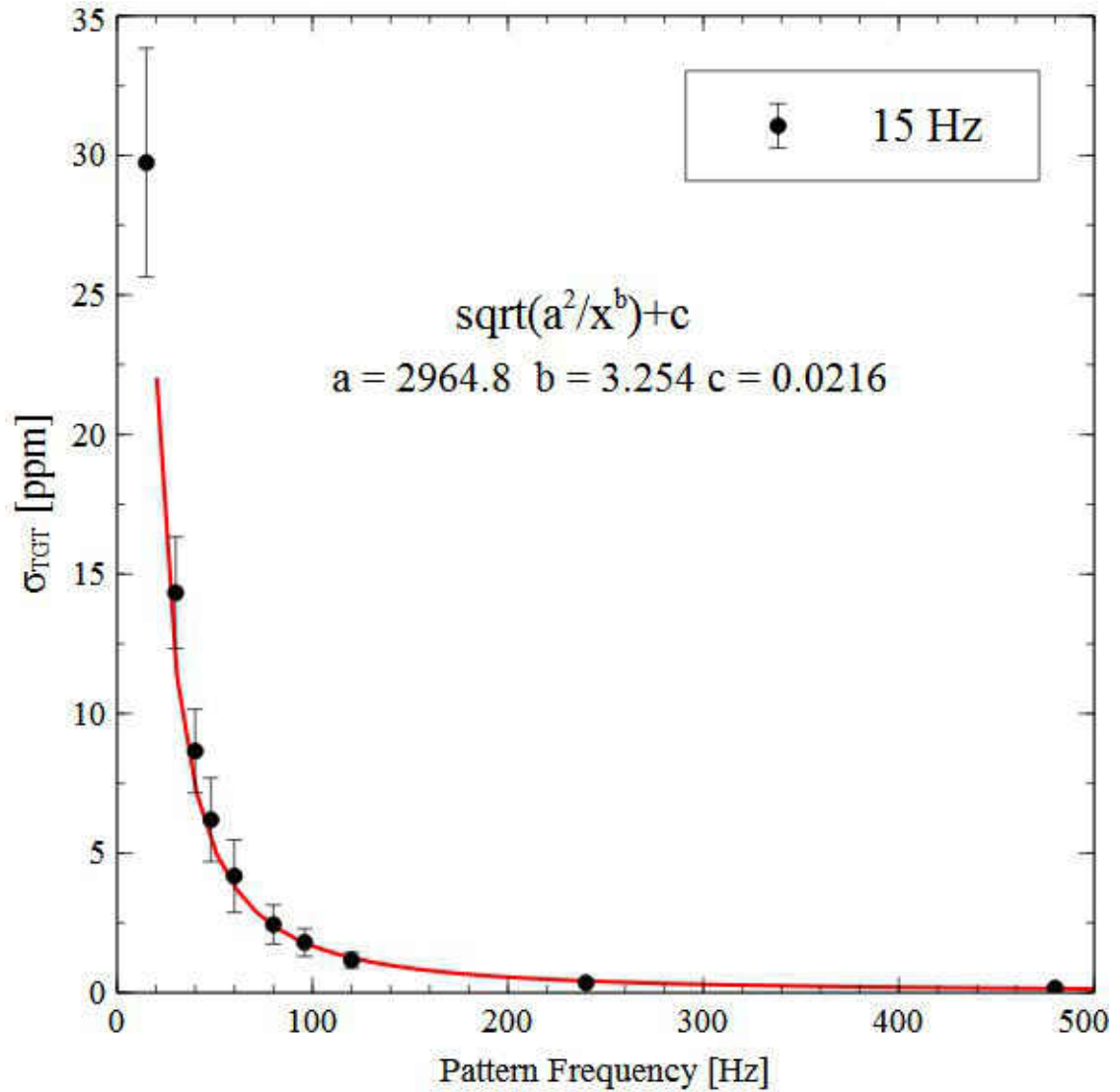
FIG. 54: Pump frequency=15 Hz, Beam current=180 μA. Density asymmetry width versus frequency for the mock helicity patterns in the Fluent density simulation results. Each data point is the statistical width of a histogram filled with the value of the asymmetry for patterns corresponding to the frequency.
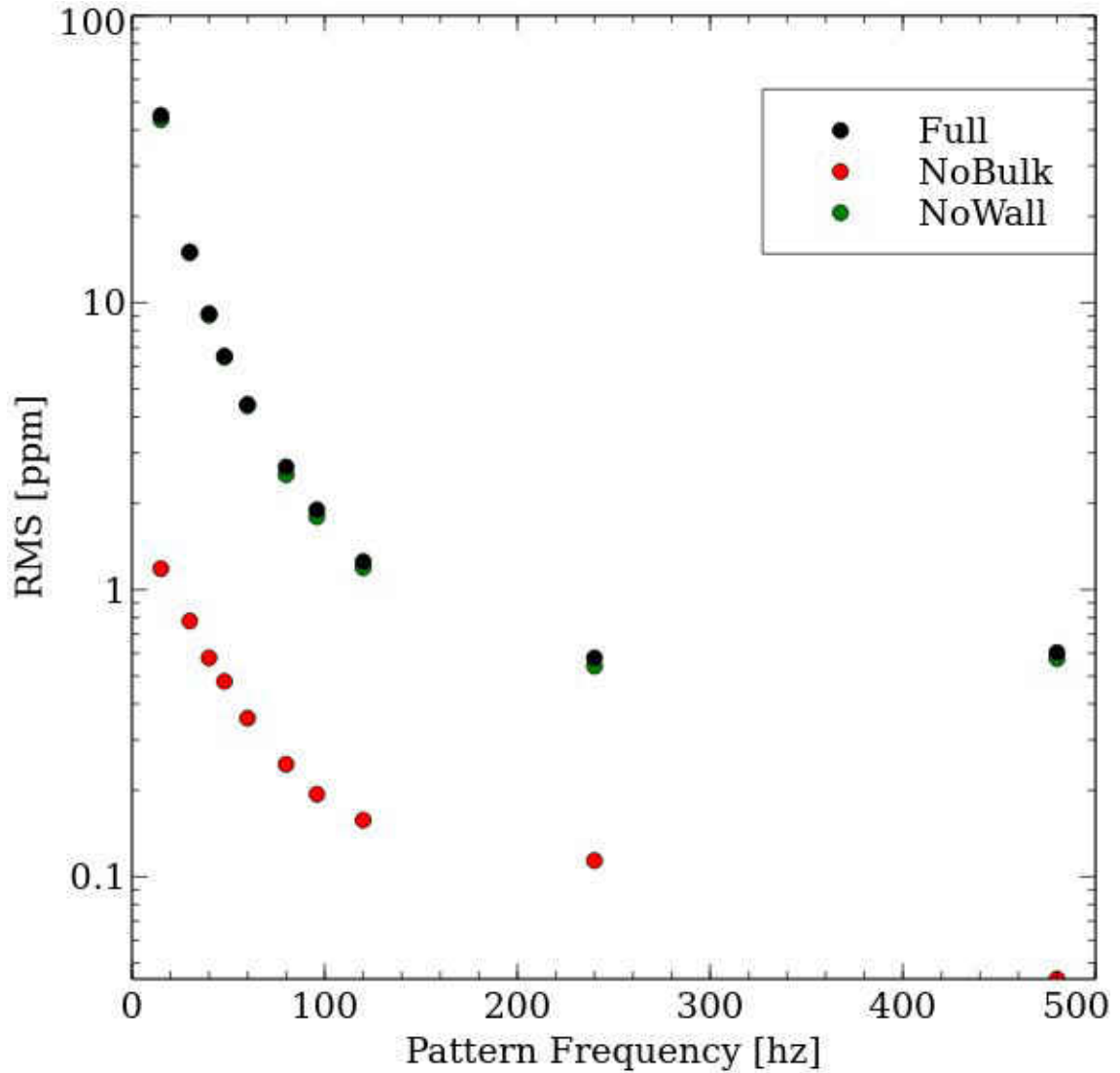
FIG. 55: Beam current= 180 μA, Pump frequency=30 Hz. Density asymmetry width versus frequency for the mock helicity patterns in the Fluent density simulation results separated into only window heating (No Bulk) and only bulk heating (No Wall). Each data point is the statistical width of a histogram filled with the value of the asymmetry for patterns corresponding to the frequency.
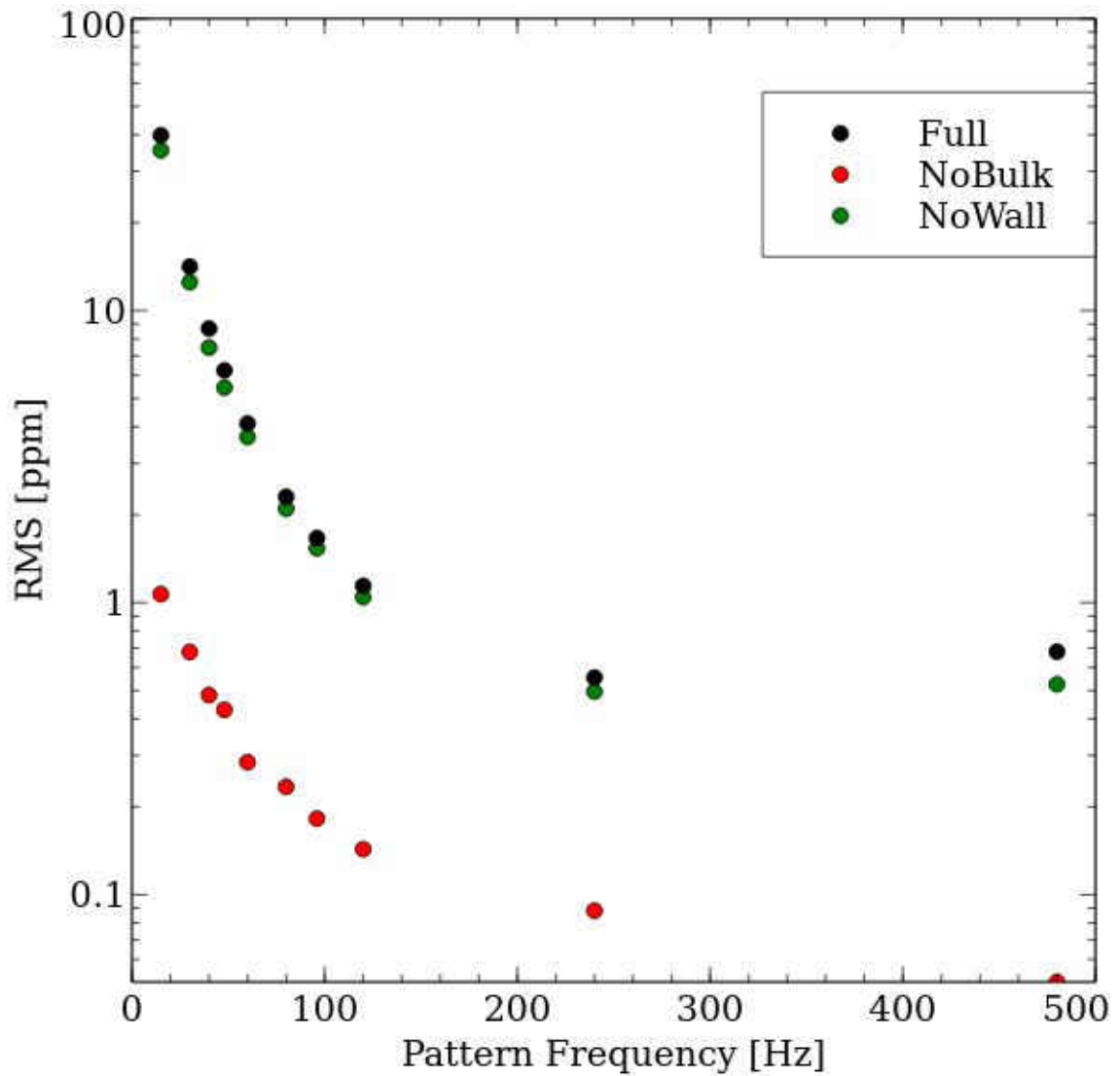
FIG. 56: Beam current= 160 μA, Pump frequency=30 Hz. Density asymmetry width versus frequency for the mock helicity patterns in the Fluent density simulation results separated into only window heating (No Bulk) and only bulk heating (No Wall). Each data point is the statistical width of a histogram filled with the value of the asymmetry for patterns corresponding to the frequency. Error bars are suppressed for clarity.
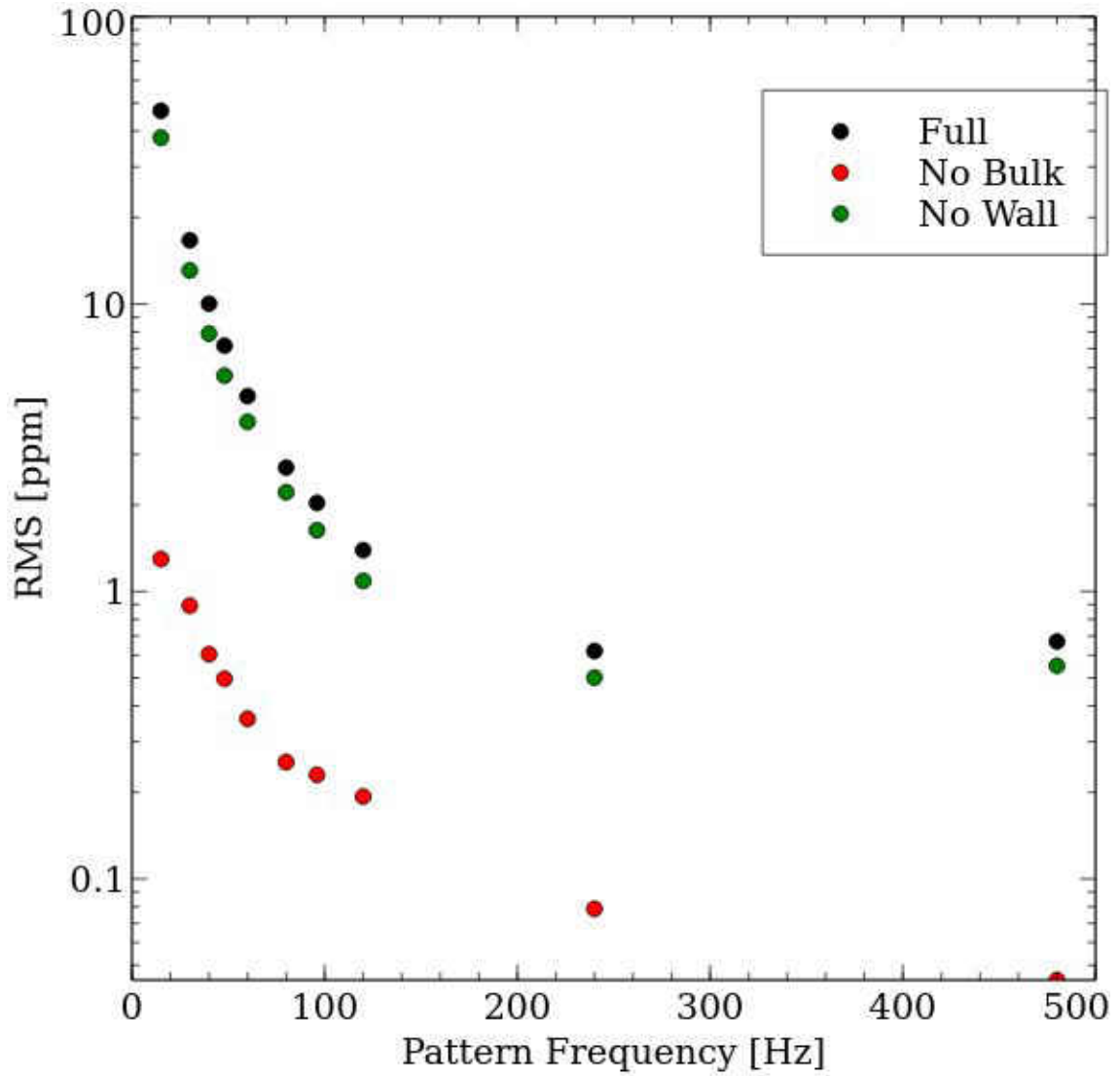
FIG. 57: Beam current= 200 μA, Pump frequency=30 Hz. Density asymmetry width versus frequency for the mock helicity patterns in the Fluent density simulation results separated into only window heating (No Bulk) and only bulk heating (No Wall). Each data point is the statistical width of a histogram filled with the value of the asymmetry for patterns corresponding to the frequency.Error bars are suppressed for clarity.
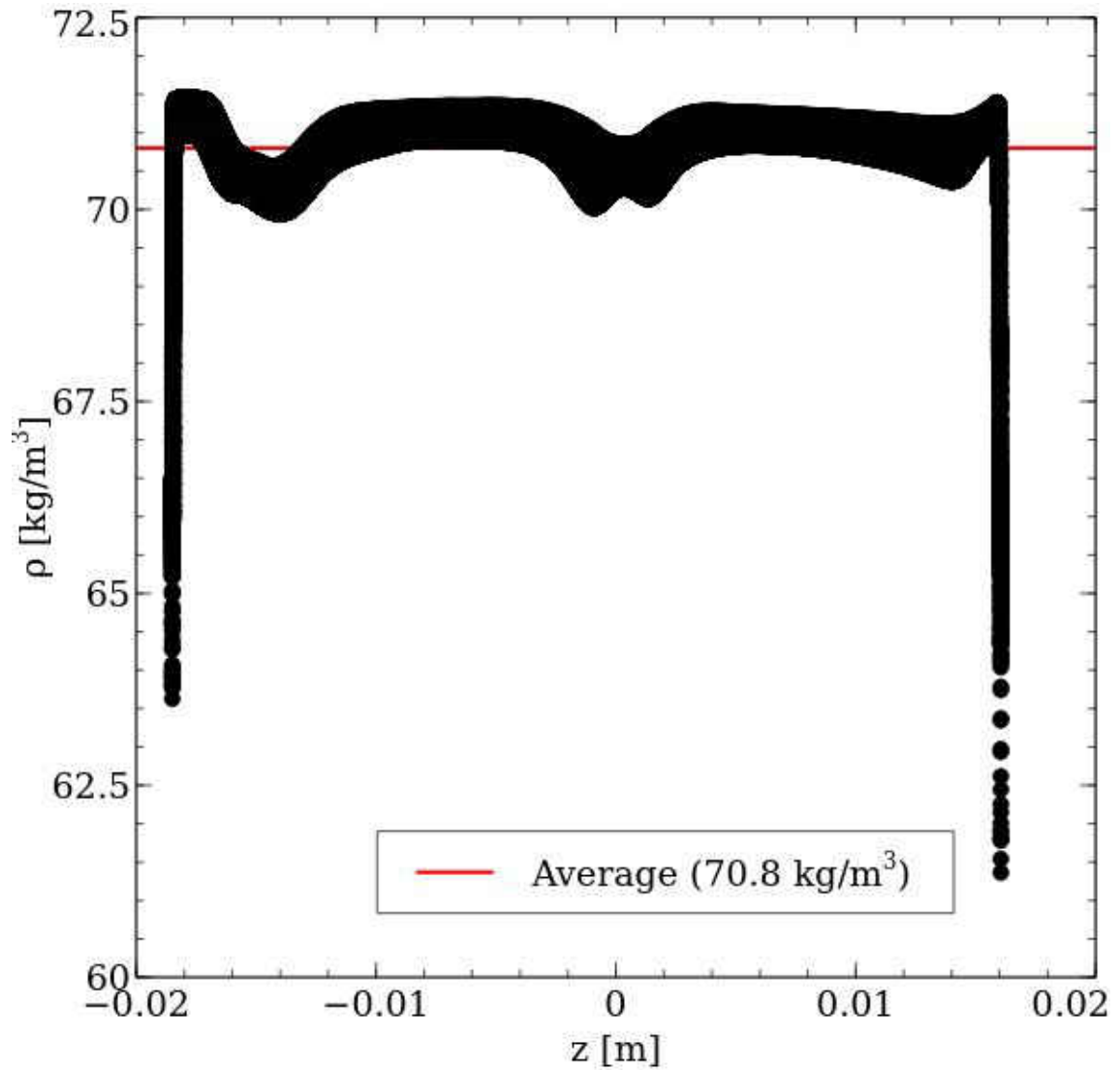
FIG. 58: Beam current=180 μA diffused, Pump frequency=30 Hz. ρ versus z, the distance along the beamline through the target. All the ρ values at each z are from all the grid points in the raster volume in the xy-plane at that z. This is with no raster and the total deposited power diffused through the raster volume. The average is shown in red. The simulation results are collected over the entire raster volume not the beam volume.
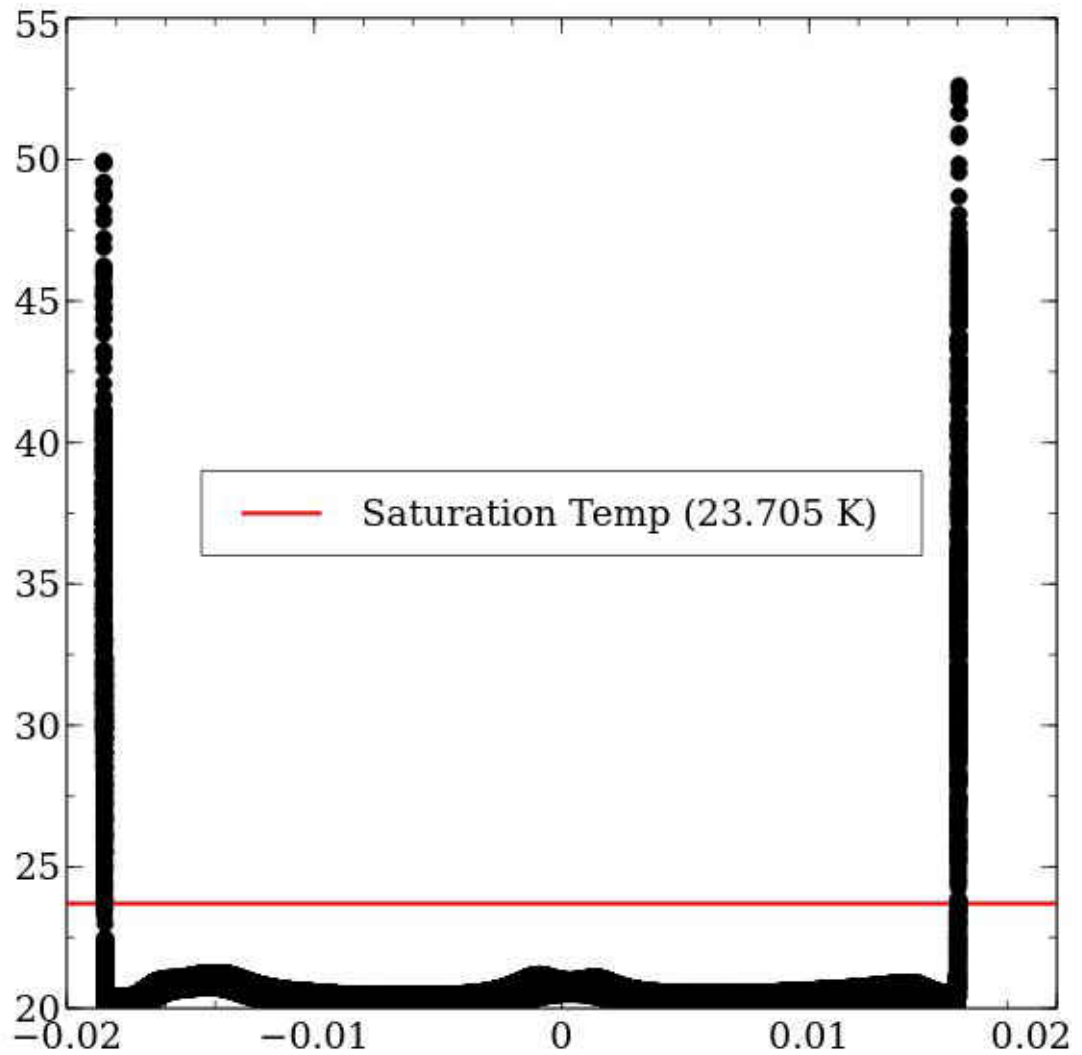
FIG. 59: Beam current=180 μA diffused, Pump frequency=30 Hz. Temperature versus z, the distance along the beamline through the target. All the Temperature values at each z are from all the grid points in the raster volume in the xy-plane at that z. This is with no raster and the total deposited power diffused through the raster volume. The simulation results are collected over the entire raster volume not the beam volume.
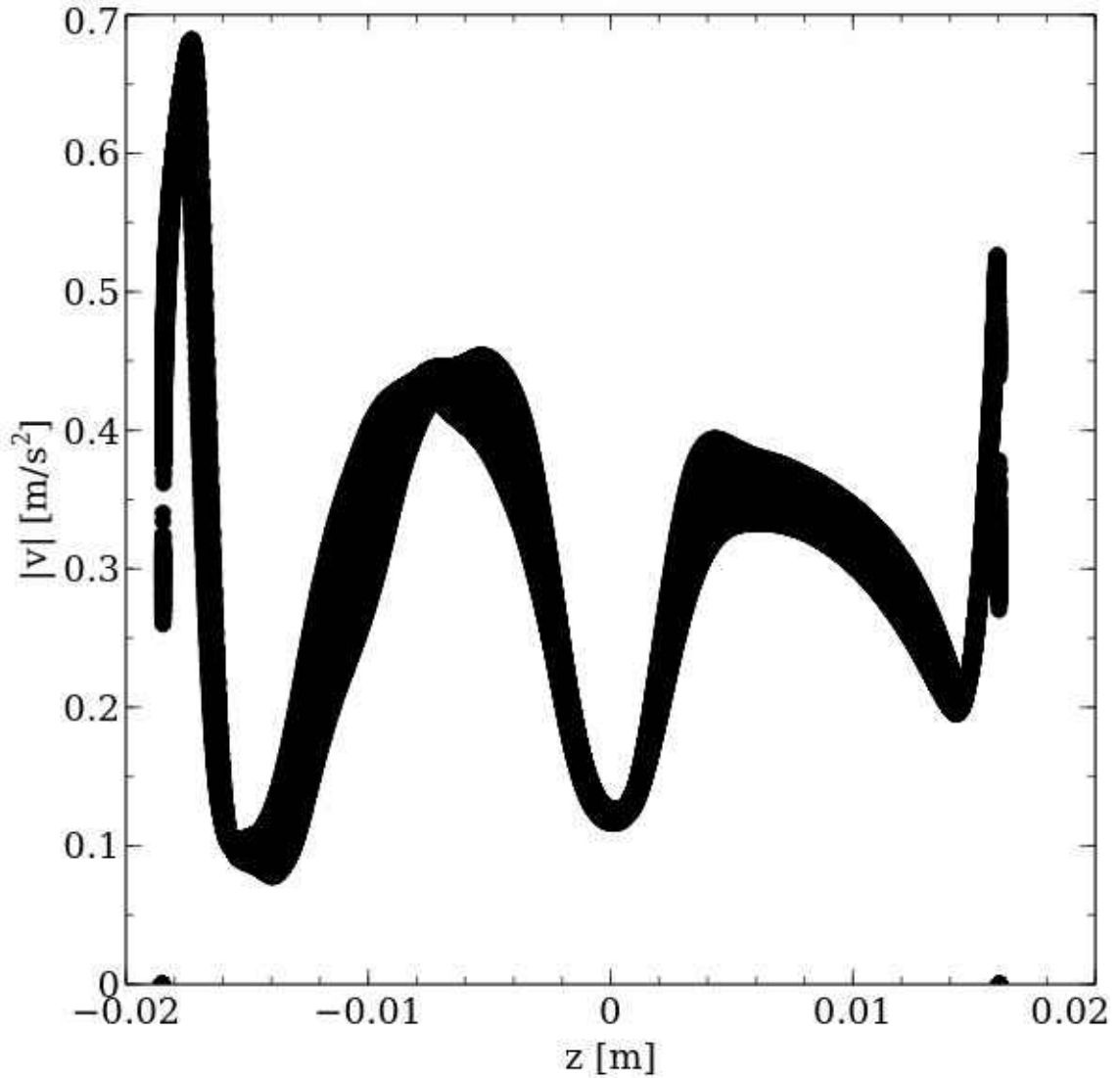
FIG. 60: Beam current=180 μA, Pump frequency=30 Hz. Magnitude of fluid velocity versus z, the distance along the beamline through the target. All the velocity values at each z are from all the grid points in the raster volume in the xy-plane at that z. The simulation results are collected over the entire raster volume not just the beam volume.
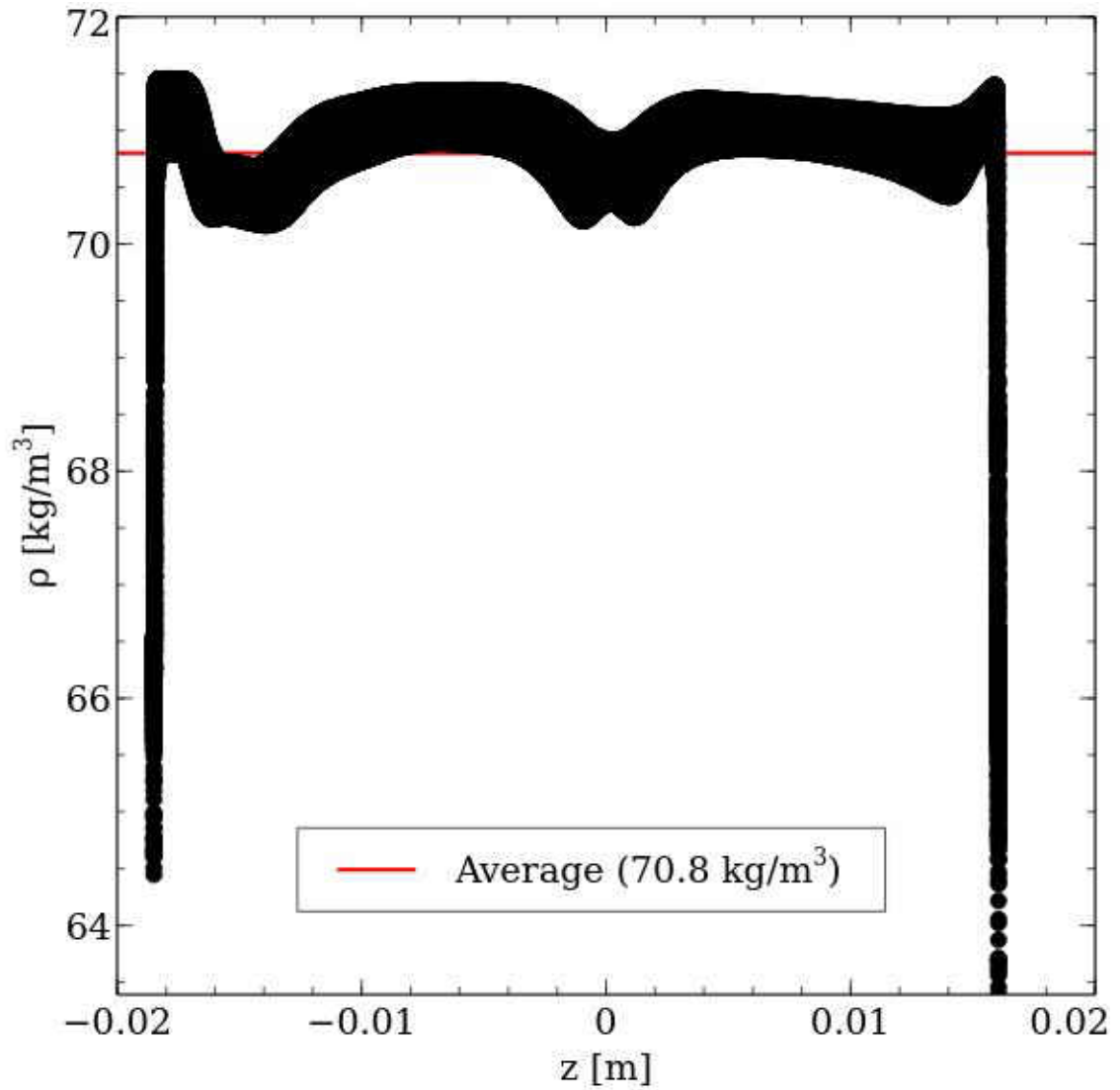
FIG. 61: Beam current=180 μA rastered, Pump frequency=30 Hz. ρ versus z, the distance along the beamline through the target. All the ρ values at each z are from all the grid points in the raster volume in the xy-plane at that z. This is with the beam following the raster motion and the the ρ values collected halfway through one Lissajous pattern. The simulation results are collected over the entire raster volume not just the beam volume.
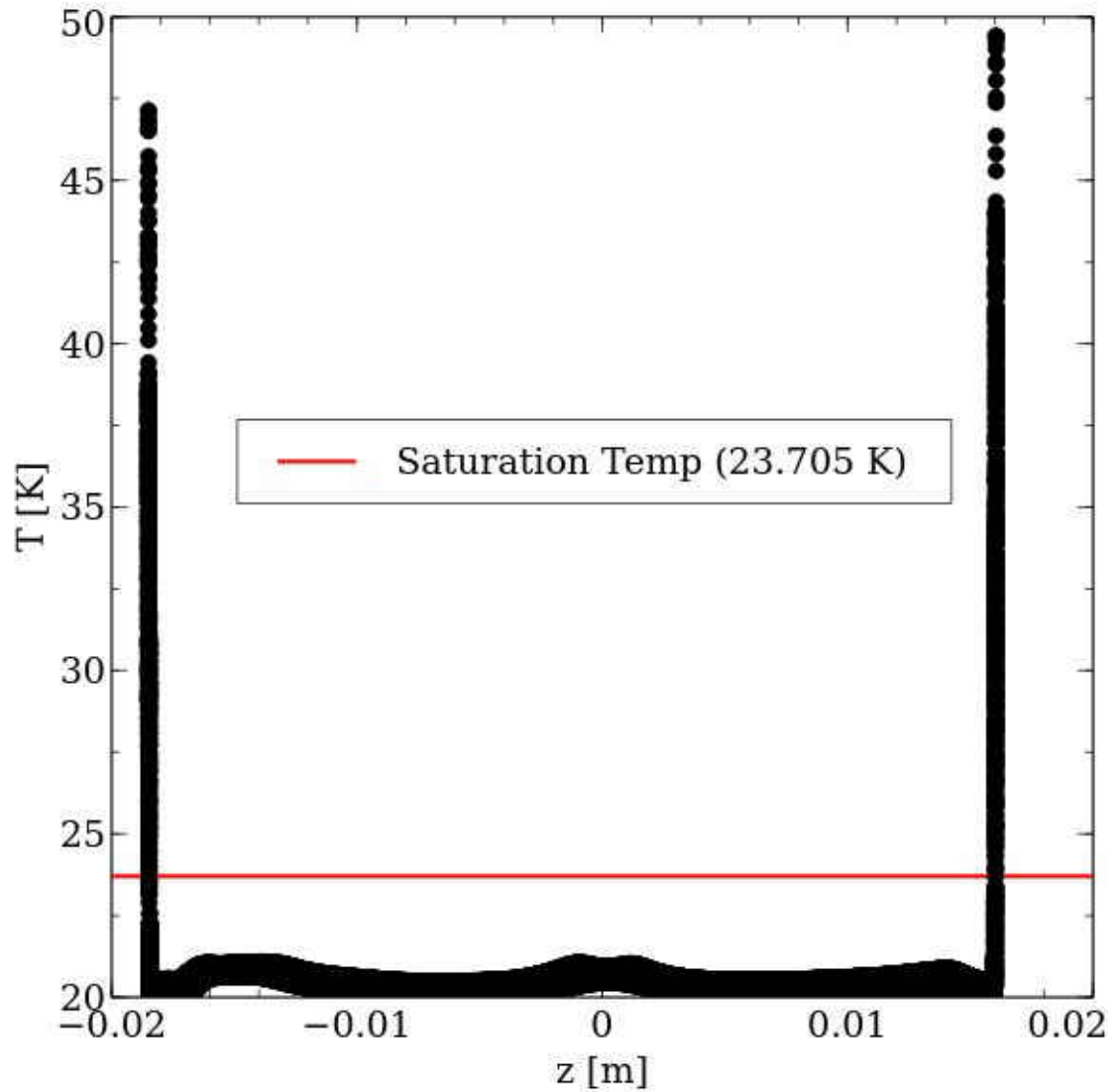
FIG. 62: Beam current=180 μA rastered, Pump frequency=30 Hz. Temperature versus z, the distance along the beamline through the target. All the temperature values at each z are from all the grid points in the raster volume in the xy-plane at that z. This is with the beam following the raster motion and the ρ values collected halfway through one Lissajous pattern. The simulation results are collected over the entire raster volume not just the beam volume. The saturation temperature for LH2 under the conditions of the Qweak target is shown in red.
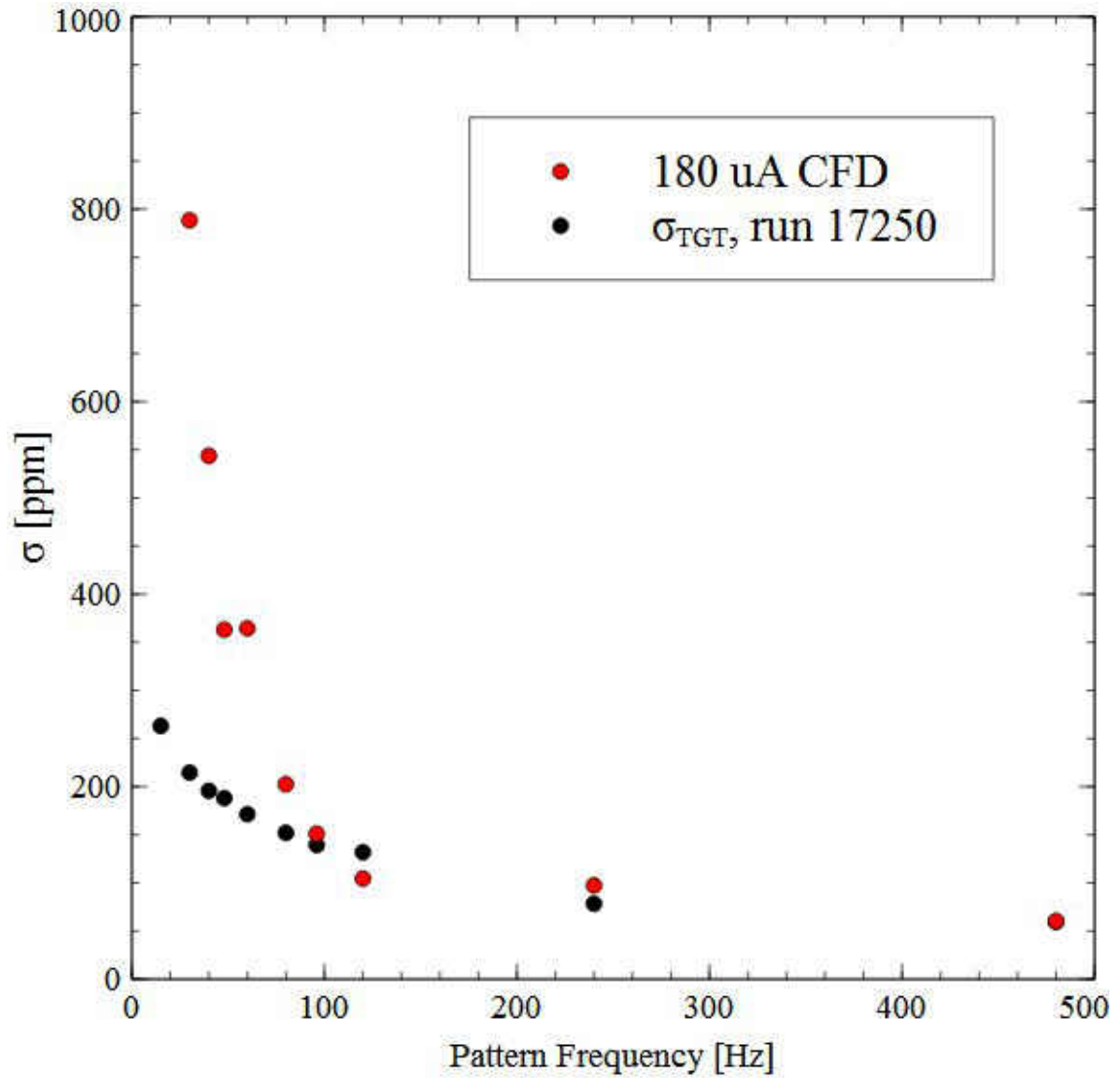
FIG. 63: By multiplying the CFD results by 98, they may be plotted with the extracted Qweak target results. The error bars have been suppressed for clarity

I_{beam} [μA]	f_{pump} [Hz]	σ at 480 Hz [ppm]	a	b	c
160	30	0.596	2917.7	3.3337	0.5225
*180	30	0.603	3663.3	3.4630	0.7717
200	30	0.810	5834.9	3.608	0.8752
360	30	1.27	83937.3	4.571	0.9728
180	10	0.884	1.802	0.4389	0.3606
180	15	0.710	2964.8	3.254	0.0216
Qweak Run 17250 Results					
179	30	59.5	757.0	0.4454	-135.34

TABLE 14: Results for the asymmetry widths from the One Ten model for 480 Hz and the fit parameters (a,b and c) from $y = \sqrt{a^2/x^b} + c$. For varying beam current the RMS increased with increasing current as expected, but the values were a factor of 50 to 100 too low. The LH2 pump speed results were inconsistent as well as the fit parameters for most of the results. * indicates the nominal case and the RMS value at 480 Hz reported from Qweak was$\approx$ 53 ppm.

violation type experiments where the beam helicity is flipped at a certain frequency. The first objective was to gain some insight into target density fluctuations by simulating the target and comparing the results to Qweak data. The main insight acquired may be the limitations of this kind of analysis. The σ values at the quartet mock helicity frequency (480 Hz) from the CFD simulations were 50-100 times lower than the values extracted from the Qweak data. The comparison plot Figure 63 shows that the CFD model reported much higher σ values at low frequencies. The CFD values in this figure have been scaled by a multiplier of 98 to make the 480 Hz data point match that of the Qweak data.

For 4.1 seconds of fluid flow time in the CFD simulation 500 values for the asymmetry calculation fill the 480 Hz histogram (500 pattern*4 MPS/pattern *28 Timesteps/MPS*37μs flow time/timestep. This takes between 5 days and a week to simulate with all 512 processors. For this amount of flow time, only 15 counts go into the 15 Hz pattern frequency histograms. In order to investigate the density fluctuations at 15 Hz pattern frequency, 500 values would take 66 seconds of flow time or 80 to 113 days of simulation time. This speed of simulation is with the quadrilateral approximation of the beam raster motion and the One Ten model.

Without the quadrilateral approximation, 66 seconds of flow time would take years since it takes 28 timesteps at 1 μs per timestep for every one timestep with the approximation ($\sim 37\mu$s per timestep). For comparison, one runlet in the Qweak data was 5 minutes. That corresponds to 300 s of flow time and 2,249 counts in the 15 Hz histogram. The lack of counts in the lower frequencies in the Fluent data may explain some of the discrepancy in Figure 63.

There were a limited number of Qweak runs that were dedicated to taking data pertaining to target boiling. The runs with varying current had an anomaly at 240 Hz pattern frequency and higher than average values at 480 Hz. From the Qweak logs it appears that something was wrong with BCM's during these runs. Fitting the data and comparing to the CFD values was not possible. Fitting to Equation 61 also did not work for the varying LH2 pump frequency runs. Despite this, the behavior of the asymmetry calculations may prove useful for future work in density fluctuations. There didn't seem to be any problems with these runs, so this could mean that a different fitting function is needed at lower pump frequencies. The ability of Fluent to reproduce the time dependence of density fluctuations is still unclear. The time it takes to simulate the models combined with the number of knobs left to turn in Fluent mean much more work is possible to benchmark the program's ability to reproduce the fluctuations. Some of the important parameters left to investigate are turbulence models and multiphase method. There are plenty of options in both that may have relevance to this simulation, including UDF's for mass transfer, slip and drift velocity, etc.

In conclusion, using CFD to simulate density fluctuations in a model of a cryogenic target at the precision required to estimate noise in parity violation type scattering experiments is not verified. A mathematically effective way of predicting the effect of a design on density fluctuations at different timescales is dependent upon bench marking the CFD program with a well controlled experiment without the complexity of Qweak. The σ_{tgt} for timescales other than the quartet frequency was not of interest in Qweak, and since the value was calculated by subtracting all other known sources of noise, it is possible that some noise at timescales other than the quartet frequency

is being included with it.

5.3.1 DISCUSSION

There are several possibilities to explain the inconsistency in the analysis. Three of those possibility's will be discussed: user error, an unaccounted noise source, and an inability of the simulation to reproduce the density fluctuations.

The first explanation is that the simulation input parameters and/or the model itself were flawed in someway. It would be preferable to rule out human error and every possible attempt was made to check all the steps along the way, but it must remain. In this thesis an effort has been made to catalog all these checks so in the future if someone finds an error in execution or assumption they will not have to start from scratch. There are definitely more possibilities that may be explored in the modeling and simulation of the Qweak target with Fluent. The One Ten scale model can be considered a trial model meant more for speed than accuracy. Any future work should use the full size model.

The second is that the simulations are providing the actual asymmetry width contribution from the boiling in the target and some other source of noise is responsible for the noise term in the Qweak experiment that is attributed to target boiling. This is more likely than it sounds. What the boiling term represents is really everything left over after the known terms are removed. This is a convoluted way to gather information about what's happening inside the target. The Qweak experiment was only interested in noise at a pattern frequency of 480 Hz. If there was noise at other frequencies it could change the values and fit parameters in this work, and gone unnoticed during the experiment.

The third possibility is that CFD is not a precise enough tool to carry out this type of analysis. This is coupled with the first conclusion in that any code is only as accurate and precise as the inputs it receives. This third conclusion is meant to say that even with the best input parameters, there is some mechanism that is not taken into account in the solution process. The most obvious problem in this regard would be bubble formation at the windows during the time-dependent part of the

simulation.

When reading up on the previous work on the density fluctuations it was troubling to find that is known about bubble sizes, frequency and location were from the extraneous data (noise terms) from complicated experiments which were designed to search for other physics. The behavior of cryogenic liquid targets interacting with electron beams deserves it's own experiment that has the capturing of density and boiling data as the main design goal. This does not necessarily have to be preformed using a large accelerator facility like CEBAF. It could be done almost at tabletop size. Coupling this type of an experiment with bench marking procedures in CFD would unravel the confusion as to what is actually happening to a cryogenic liquid when exposed to beam and lead to the best way of either ruling out or confirming the other two conclusions. Early on in this study an attempt was made to find video and/or acoustic transducer data on LH2 boiling. None could be found and it was heard several times that the extra data taking hardware for this purpose were requested and denied for this and other experiments at JLab. The radiation in the experimental halls, especially in the target itself, make such data very difficult to record. A smaller experiment using heating elements to avoid radiation would allow a detailed comparison to the density fluctuations reported in other experiments and provide benchmarking for the simulations.

CFD has proven itself robust in many different applications with the right setup, so the likelihood that it is unable to solve the problem is small. That being said, the ppm scale of the simulated results that this type of analysis is looking for would be taxing for any simulation code. Fluid dynamics is more complicated than other types of simulations (electromagnetic, mechanical, etc.) and thre is a chance that, regardless of input parameters, this is just asking too much of an iterative process. Within the time scale of this analysis ANSYS released two major updates to Fluent along with several smaller ones. The latest release, Fluent 18.1 was released this year and has not been tried yet. It is always possible that one of these updates will provide the necessary adjustments to change the results of these simulations. To determine if CFD can do a simulation like this with millions of time-steps and still

remain accurate to a ppm level would require the elimination of all input parameters as problems. When all of the basic solution types and options have been exhausted there is still the addition of UDF codes to simulate things like turbulence, mass-transfer, and energy sources. This work focused mainly on the energy source UDF and did not attempt UDF's for turbulence and mass-transfer.

The turbulence models in FLUENT are many and well-documented. In a steady state situation the simulated flow inside the target agrees with what is known about the target from the experimental data, but in the time-stepping realm without benchmarks there is no way to know how well the flow patterns are reproducing reality. The turbulence in the target is essential for noise analysis as it has direct bearing on the mixture of the heated fluid inside the full raster interaction volume with the colder fluid upstream and warmer fluid downstream. A small variation is this mixing over time can lead to much different results in the mock helicity asymmetry equations.

In conclusion, using CFD to simulate density fluctuations in a model of a cryogenic target at the precision required to estimate noise in parity violation type scattering experiments must wait until a bench marking experiment for bubble formation is done. As in most of the history of cryogenic fluid target design, a design can end up being very effective just from a study of older designs that have and have not worked. A mathematically effective way of predicting the effect of a design on density fluctuations at different timescales is dependent upon knowledge of how the bubbles at the windows form and burst. Once the parameters for the situation at the windows is understood better, CDF should be able to carry out this kind of simulation well enough to make conclusions about the noise from density fluctuations.

CHAPTER 6

SUPER HIGH MOMENTUM SPECTROMETER(SHMS)

PRIMARY BEAM DISPLACEMENT ANALYSIS

During the 6 GeV era there were two standard spectrometers for Hall C, the High Momentum Spectrometer (HMS) and the Short Orbit Spectrometer (SOS). In September 2008 JLab received approval from the Department of Energy (DOE) to upgrade the maximum electron beam energy from 6 GeV to 12 GeV. This doubling of electron beam energy allows for a substantial increase in measurement capabilities for Hadron structure experiments. Of particular importance in the DOE's decision to fund the $310 million upgrade is the study of quark confinement. Understanding why quarks are only found together and never alone is one the great unsolved mysteries of particle physics. As part of the upgrade Hall C requisitioned the Super High Momentum Spectrometer (SHMS) to complement the existing HMS, and the SOS was retired.

Both the HMS and SHMS have focusing elements consisting of quadrupole triplets (Q1, Q2, Q3) [36] followed by vertically bending dipole magnets. Both the HMS and the new SHMS are connected to a central pivot located underneath the target chamber (see Figure 64). Large wheels rolling on rails around the target allow these spectrometers to accommodate a wide range of scattering angles. The HMS has an angular range of 12.5° to 90° and the SHMS has a range of 5.5° to 40°. The quadrupole coils are fully enclosed by the yokes and the minimum detectable scattering angle is limited by the proximity of the magnets to the exit beam pipe containing the remaining unscattered electron beam. One of the primary differences between the HMS and the newly designed SHMS is a 3° horizontal bending magnet (HB) placed between the target and the first quadrupole magnet. When positioned at the smallest scattering angle, the SHMS makes an angle of 8.5° with respect to

the beam line. The HB allows particles scattered at an angle of 5.5° to be steered into the optics of the SHMS by bending the trajectory of the scattered particles 3° horizontally away the primary beam line. Figure 65 shows the elements of the SHMS used in this analysis. Standard equipment in Hall C includes a fixed liquid hydrogen (LH2) target and two magnetic spectrometers. After collision with the target, the remaining unscattered electron beam then travels past the spectrometer to a high power beam dump (51.8 m from the target) where it can be safely absorbed [37]. Recent simulations have shown that the magnetic field leakage from the SHMS magnets would steer the unscattered primary beam away from the center of the beam dump [38]. The acceptable region of the beam dump for high current operation is a relatively small area in the center of the larger water tank which comprises the beam dump. If unmitigated, SHMS operations would be restricted to low electron-beam currents for small spectrometer angles. Presented here are the first 3D magnetic field simulations of the four leading magnets of the SHMS with emphasis placed on the fields along the beam line and the position of the beam at the beam dump due to these fields. A passive solution using optimal placement of extra iron along the beam line is presented.

6.1 GEOMETRY OF THE SHMS

In order to simulate the magnetic fields from the SHMS, the yokes and coils of the magnets were modeled with the Opera-3D software [39] as shown in Figure 66. Opera serves as the modeler and post processor for a suite of finite element simulation tools. TOSCA is the static electromagnetic field simulator used with Opera to find the magnetic fields in this study. The coordinate system of the simulation was chosen with the z-axis pointing downstream along the optics line of the SHMS (through the center of the quads) and the origin placed at the vertex of the 3° bend in the HB (see the left diagram in Figure 67). The spectrometers can be set to accept either positive or negative particles by reversing the polarity of the magnets. TOSCA simulations of fields for positive and negative spectrometer settings result in equal and opposite
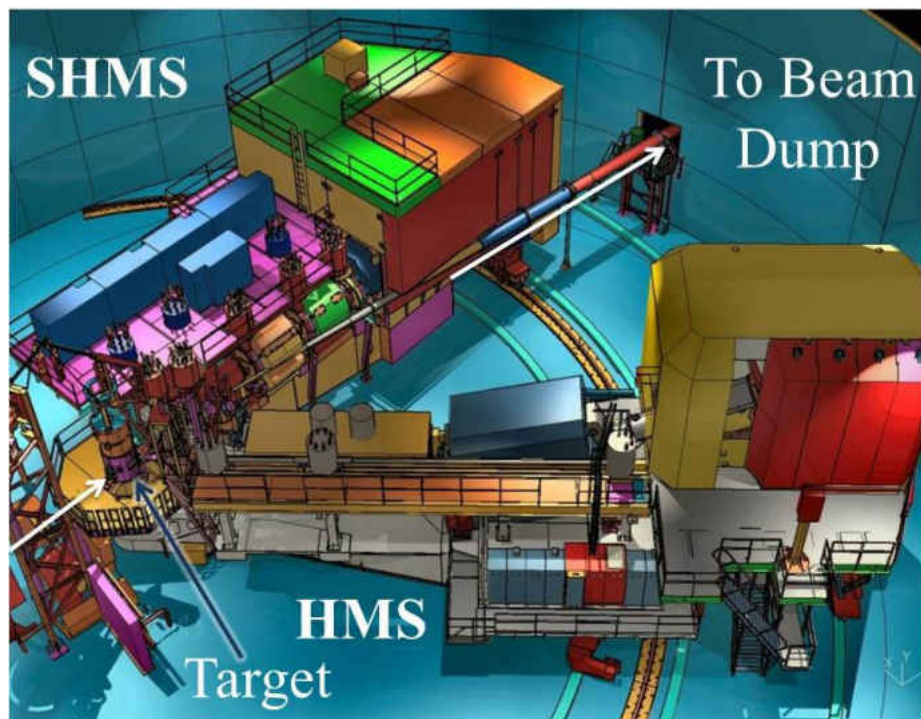
FIG. 64: Hall C at JLab showing the two spectrometers and the primary beam line. The primary beam line is indicated by white arrows.
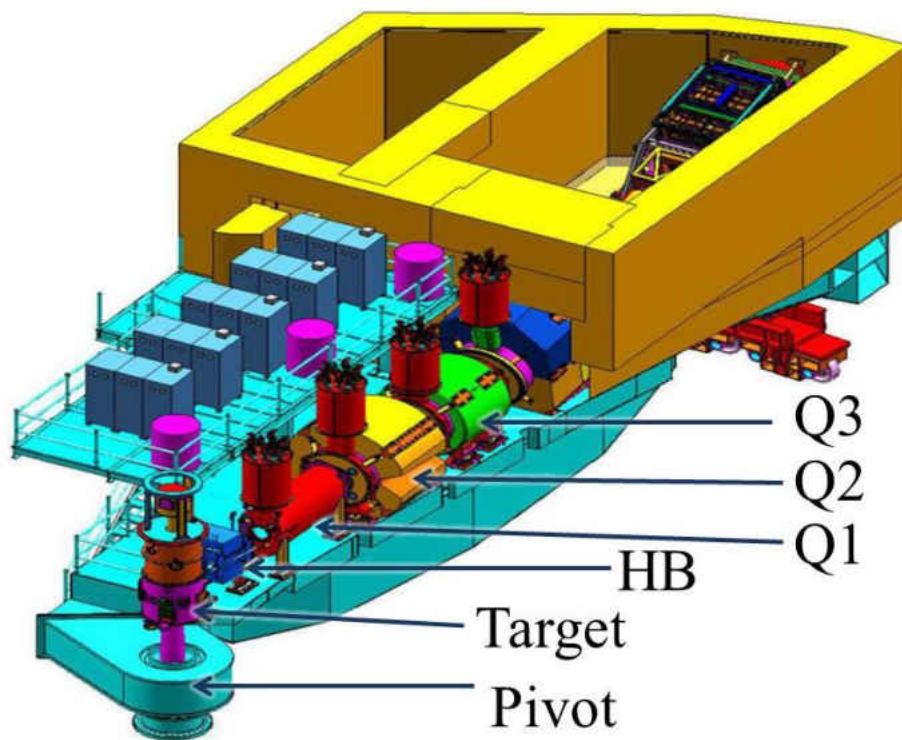
FIG. 65: Main elements of the SHMS. See text for explanation.

magnetic fields along the beam line. To avoid complication only negative spectrometer settings are reported. Once the fields are found using TOSCA, to determine

HB-Horizontal Bender
- Warm iron "C" yoke
- Current Density $= 21.2$ A/cm^2
- Dipole field producing $3°$ bend

Q1-Quadrupole
- JLab cold iron quad design
- Current Density $= 14.9$ A/cm^2
- Vertical focusing

Q2- Cosine 2θ Quadrupole
- Warm yoke
- Current Density $= 4.9$ A/cm^2
- Horizontal focusing

Q3- Cosine 2θ Quadrupole
- Warm yoke
- Current Density $= 3.3$ A/cm^2
- Vertical focusing
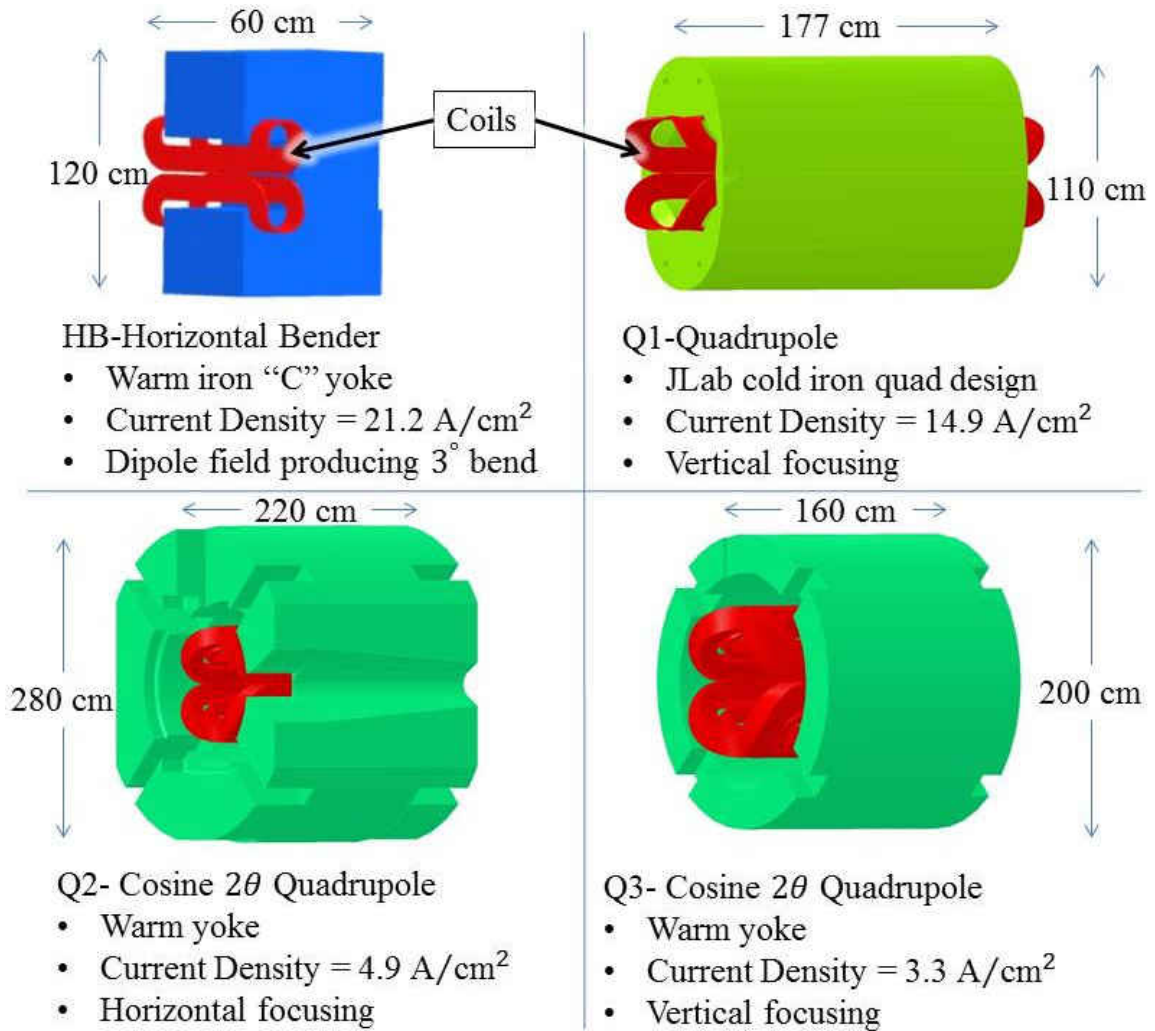
FIG. 66: SHMS magnets as built in Opera. The current densities are for the maximum central momentum setting of the spectrometer.

the beam displacement at the dump, a single electron trajectory was calculated using Opera's post-processor. Given the electron's initial position (the target), beam energy (11 GeV), and direction (along the beam line), Opera calculates the Lorentz force in 1 cm steps along the trajectory and returns the electron's position, velocity and time at every step. Using this information and the geometry from Figure 67, the beam displacement at the beam dump can be estimated as follows. In the simulation coordinate system the target and the center of the beam dump window are located
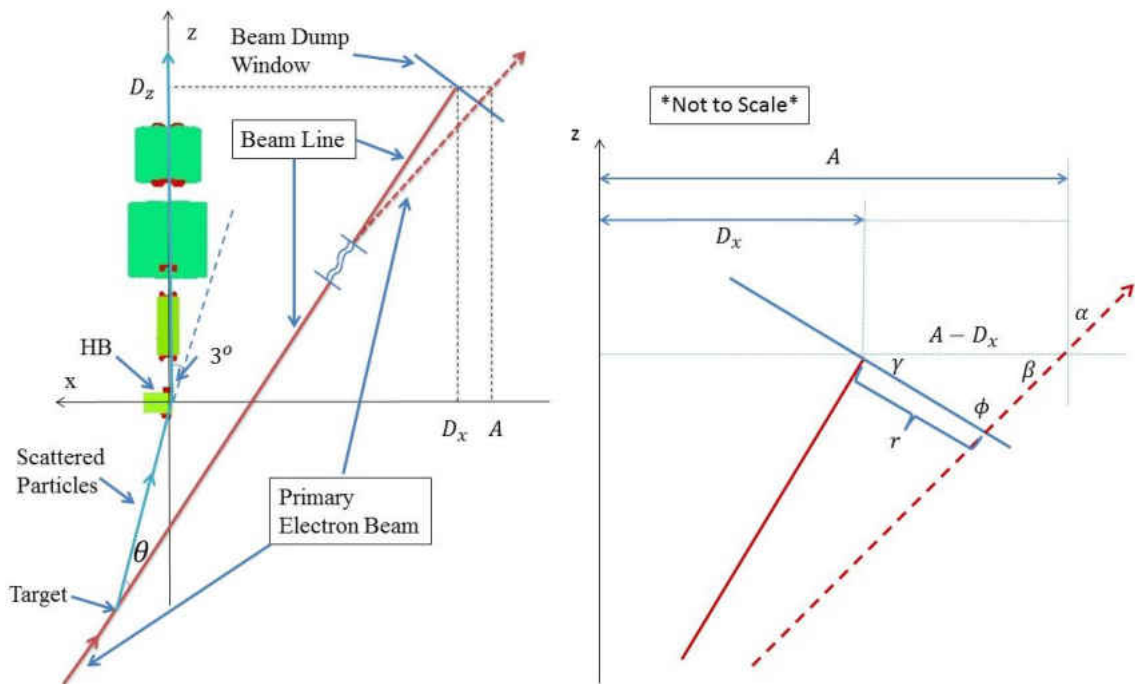
FIG. 67: *Left*:The geometry of the beam line on the coordinate system with the origin at the HB and the z-axis along the optics line. The primary beam trajectory follows the beam line to the beam dump window with no field leakage (solid line). With field leakage (dashed line) it misses the center. *Right*: Close up of the intersection between the beam line and the beam dump window showing the beam displacement, r. See text for explanation.

in the (x, z) plane. With the center of the target fixed at $(x = 9.21, z = -175.76)\,\mathrm{cm}$, the center of the beam dump window is found as a function of the scattering angle, θ,

$$D_x(\theta) = -(D\sin(\theta + 3) - 9.21), \tag{62}$$

$$D_z(\theta) = D\cos(\theta + 3) - 175.76, \tag{63}$$

where $D = 5180$ cm is the distance from the target to the center of the beam dump window. Since the beam dump window is always perpendicular to the beam line, the angle of the window also changes with θ in this model. The diagram on the right side of Figure 67 shows the geometry used for this correction. The law of sines for the triangle in the diagram states

$$\frac{A - D_x}{\sin\phi} = \frac{r}{\sin\beta}. \tag{64}$$

Then using the relations $\beta = 90 - \alpha$ and $\phi = 90 - (\gamma - \alpha)$, the displacement r at the dump is

$$r(A, \alpha) = (A - D_x)\frac{\cos(\alpha)}{\cos(\gamma - \alpha)}, \tag{65}$$

where D_x and γ are determined from the spectrometer angle. By assuming that the magnetic fields at the beam dump window are negligible, it is possible to calculate A and α from the Opera trajectory file. Note that a negative displacement means beam right and positive is beam left. For the maximum displacement $(r_{\max})$ of a single electron at the beam dump window, allowances must be made for the growth in the size of the beam due to square rastering before the target and scattering at the beam diffuser and several vacuum windows. For safe operations of the beam dump, the radiation control group at Jefferson Lab suggests the beam size at the dump window should be set to a $4 \times 4\,\mathrm{cm}^2$ square around the center of the beam [40]. This limits $|r_{\max}|$ to 2.25 cm so that the $4 \times 4\,\mathrm{cm}^2$ rastered beam profile fits within the 5.08 cm radius high current acceptance region of the beam dump window.

6.2 TOSCA FOR MAGNETIC FIELD ANALYSIS

TOSCA is an analysis module of the Opera-3d (an OPerating environment for Electromagnetic Research and Analysis) suite of finite element software made by the English company Vector Fields Limited. TOSCA has been used for over twenty years and is well known for its speed and accuracy. TOSCA solves non-linear magnetostatic or elctrostatic field and current flow problems. It formulates problems based on total and reduced scalar potentials. In a region of space Ω

$$H = H_m + H_s \tag{66}$$

where H_s is the field from any currents within Ω and H_m is the field produced by any currents outside. H_m is described as the gradient of the reduced scalar potential ϕ

$$H_m = -\nabla\phi \tag{67}$$

H_s is found directly using

$$H_s = \frac{1}{4\pi} \int_\Omega J \times \nabla \left(\frac{1}{R} \right) d\Omega \tag{68}$$

where J is the current density and $R = |r' - r|$ is the distance between the source and field points. By combining Equations 66 and 67

$$-\nabla\mu\nabla\phi + \nabla\mu\nabla H_s = 0 \tag{69}$$

where μ is the magnetic permeability in Ω. FEM is then used to solve these equations for ϕ in each cell. The cells are produced by discretization [41].

6.3 DISCRETIZATION AND THE FINITE ELEMENT METHOD

The discretization method is the same for FEM as it is for FVM. Opera-3d integrates the geometric modeller and the meshing application into the pre-processor part of the program. Setting up the mesh is a little more complicated for magnetic

fields than it is for fluid flow. The flow space in Fluent is bounded, while the magnetic fields from electromagnets are solved in free space where the only boundary conditions are the magnetic field measured at an infinite distance from the source ($B_{d=\infty} = 0$). More mesh elements mean more processing time for the solver. This leads to three levels of mesh cell size. The iron yokes of the magnets and a tube around both the primary beam line and the spectrometer aperture were meshed with cell sizes on the order of one centimeter. A cylinder surrounding all the magnets and the primary beam line were meshed with cell sizes of approximately five centimeters. Surrounding all of this with a radius equal to ten times the length of the SHMS were cells that could grow as large as one meter.

6.4 RESULTS FOR SHMS AS DESIGNED

From the fields simulated by TOSCA, it was immediately evident that the only field component of interest was the vertical component along the beam line. Figure 69 shows the variation of the vertical component of the field along the beam line for several spectrometer angles at 11 GeV. For a spectrometer angle of 5.5° at 11 GeV the magnetic field integral, $\int B_y dl$, of the HB field leakage along the beam line ($z = \{-100, 100\}$ cm) is responsible for 78% of the total field leakage.

The displacement of the beam calculated from Equation 65 for the angles and energies of interest are plotted in Figures 70 and 71 . With the as-designed SHMS, the primary beam has a displacement at the beam dump window of -18.2 cm when operated at 5.5° and 11 GeV, and misses the window at all angles below 13°. The displacement vs beam energy in Figure 71 has the central momentum of the spectrometer set to match the incident beam energy. The displacements were more than $r_{\max}$ for all the energies studied, $E = \{2, 4, 6, 8, 10, 11\}$ GeV. These displacements would inhibit beam operations in Hall C, therefore a solution needed to be found that would bring the displacements below $|r_{\max}| = 2.25$ cm for all angles and energies.

6.5 PASSIVE SOLUTION
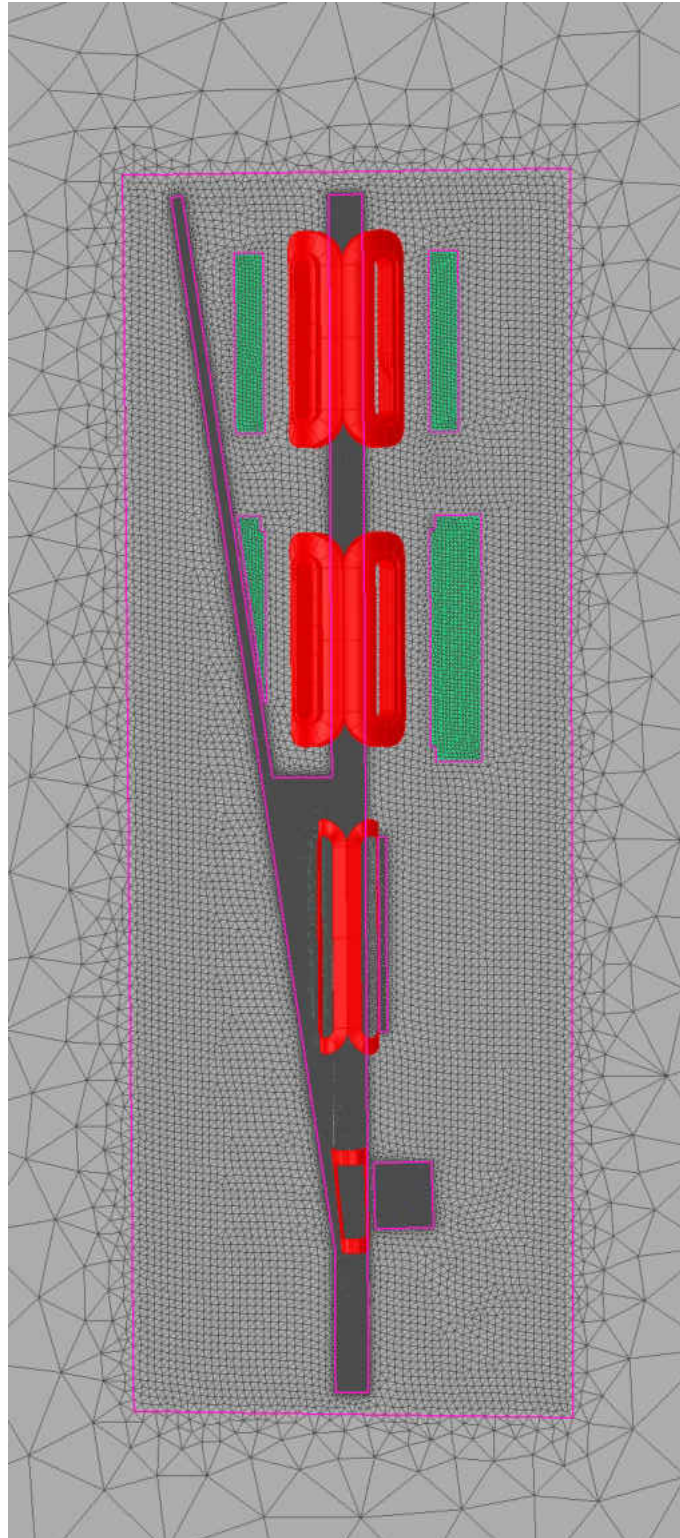
FIG. 68: Mesh zones in Opera to simulate the magnetic fields of the SHMS in the xz plane. The coils of the magnets are seen in red and the the yokes in green. The HB yoke can as a dark grey square below the first coil (from left to right). The smallest size mesh is in the yokes and the dark grey area through the center of the coils and the upwards to the left representing the beam line.
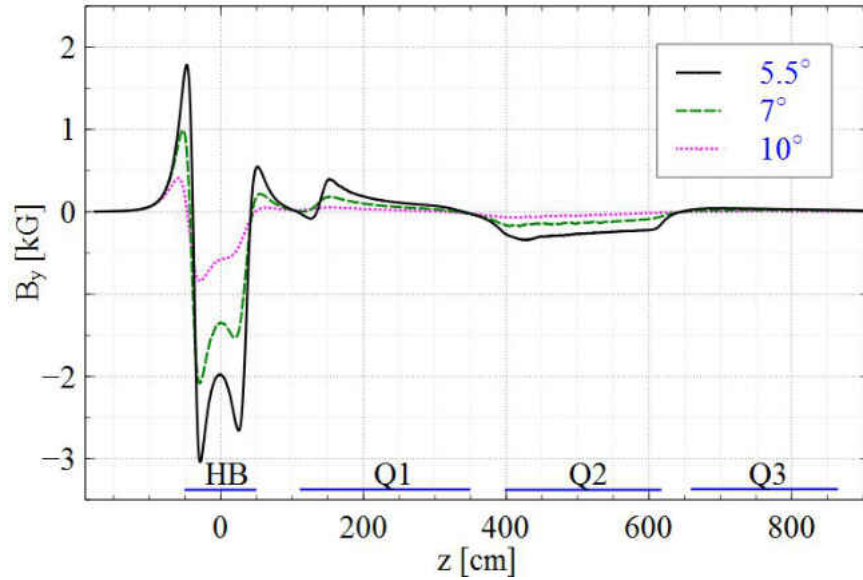
FIG. 69: Variation of the vertical component, B_y, of the simulated field along the beam line with the "as-designed" SHMS. Three spectrometer angles are shown with the spectrometer central momentum set to a beam energy of 11 Gev. The horizontal axis gives the z-component of the distance from the target along the beam pipe. The edges of the four magnet yokes are marked along the horizontal axis.
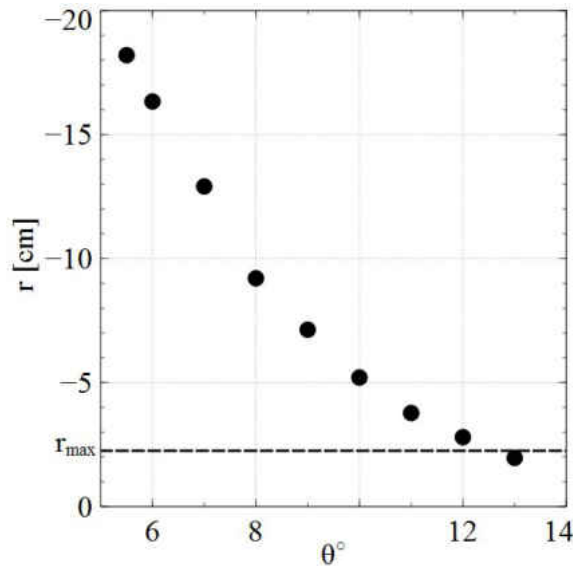
FIG. 70: Beam displacement, r, from the center of the beam dump window vs spectrometer angle. All displacements are taken with a beam energy of $E = 11$ GeV and the spectrometer central momentum set to the beam momentum. The dashed line indicates the maximum allowed displacement, $r_{max} = 2.25$ cm. Everything above this line will miss the acceptable region of the beam dump window. Negative r values correspond to beam right displacements.
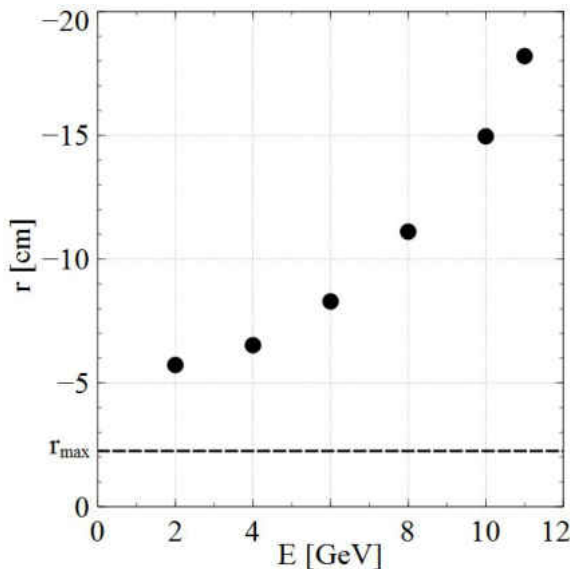
FIG. 71: Beam displacement, r, from the center of the beam dump window vs beam energy with the spectrometer central momentum set to the beam momentum. The displacements are taken with $\theta = 5.5°$. The dashed line indicates the maximum allowed displacement, $r_{max} = 2.25$ cm. Everything above this line will miss the acceptable region of the beam dump window. Negative r values correspond to beam right displacements.

Redesigning and rebuilding of the SHMS magnets to overcome the beam steering issue was not practical due to schedule and cost constraints. At the beginning of this analysis the magnets were already being manufactured. The first beam in Hall C was scheduled for 2016. Two possible solutions remained: (1) Use steering magnets, accompanied by beam position monitors (BPMs), to actively steer the beam back to the center of the beam dump window or (2) add extra iron to the existing magnet yokes and primary beam pipe to reduce the field leakage along the beam line as a passive solution. Steering magnets and BPMs located downstream of the target would have to be radiation hardened and operate continuously making this the more expensive solution. A steering magnet could be placed before the target but this would affect the optics. Any active solution would have to be re-tuned with every change of scattering angle or energy. The passive solution has several advantages over steering magnets, most importantly it is intrinsically fail-safe. The fields in the

beam pipe region will be attenuated regardless of spectrometer setting. However, extra material downstream of the target presents an activation hazard and steps must be taken to minimize activation. These steps include minimizing the amount of material and modeling the activation using GEANT4 [42]. As a first step in simulating the fields for the passive solution, extra iron of various shapes and sizes were added to the HB yoke. The most advantageous was clearly an iron pipe around the beam pipe but such a large amount of material so close to the beam line was undesirable due to activation. The iron additions that were most successful are shown in Figure 72 and the corresponding reduction in field integrals are given in Table 15. The field integrals are along the beam line from $z = \{-176, 900\}$ with a $5.5°$ scattering angle and the maximum central momentum setting of the spectrometer. The wedges are the most successful at attenuating the fields and are far enough away from the beam line to not become an activation problem. For comparison, the
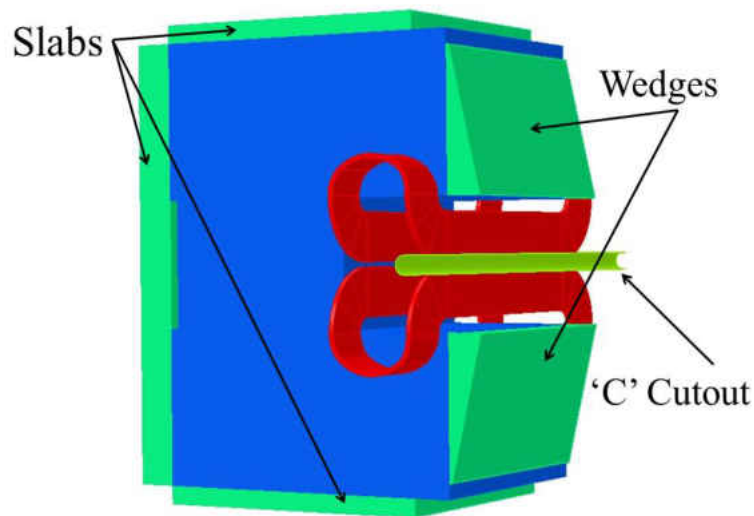
FIG. 72: Extra iron pieces added to the HB yoke to reduce field leakage. The slabs and wedges are attached directly to the yoke. The 'C' cutout is permanently attached to the cryostat which houses the coils.

displacements of 30 different combinations of extra iron pieces and pipes are plotted versus their magnetic field integrals in Figure 73. All these simulations are for a $5.5°$ scattering angle, $11\,\text{GeV}$ electron beam and maximum central momentum setting of

Additions	Field Integral (kG cm)	% Reduction
None	-110.49	0
Slabs	-108.76	1.57
Wedges	-58.82	46.77
'c' cutout	-89.20	19.27
All	-35.80	67.6

TABLE 15: Field integral reductions from adding extra iron to the HB yoke.

the spectrometer. The linear fit determines the maximum absolute value of the field integral that constrains the displacement at the the beam dump to $r_{max} = \pm 2.25$ cm. Under these conditions, the absolute value of the field integral must be less than $19.25\,\text{kG} \cdot \text{cm}$. Unfortunately, all the extra iron pieces on the HB yoke are unable to constrain the absolute value of the field integral to below 19.25 kG·cm. To further reduce the field integral, an iron pipe around the beam line at the HB was then studied as the next step of the simulation. Several thicknesses, lengths and positions of pipes were studied in Opera. It was found that when used in conjunction with the wedges on the HB, the thinnest pipe wall that provides effective shielding of the field was 0.476 cm (3/16"). Initially, short pipes around the HB were studied to balance the total field integral. Although the displacement for 5.5° could be minimized to below r_{max}, the behavior at larger angles and smaller energies was erratic mainly due to saturation effects and changing locations of field maximums at different angles. To make the pipe solution robust at all angles and energies, a 2 m long pipe at HB and a 1.5 m pipe at Q2 were designed (see Figure 74). The HB pipe has an inner radius (IR) of 2.37 cm through the entire length. To minimize activation, the Q2 pipe is tapered from IR=5.53 cm on the upstream end to IR=7.46 cm on the downstream end. The simulated magnetic field along the beam line with the iron wedges and pipes is shown in Figure 75. These simulations are for a 5.5° scattering angle and maximum central momentum setting of the spectrometer. The as-designed SHMS field is shown for comparison. The magnetic field integral along the beam line with the iron pipes and wedges is −6.8 kG·cm, meeting the criteria of an absolute value less than 19.25 kG·cm found above. The high attenuation of the entire HB external field makes this
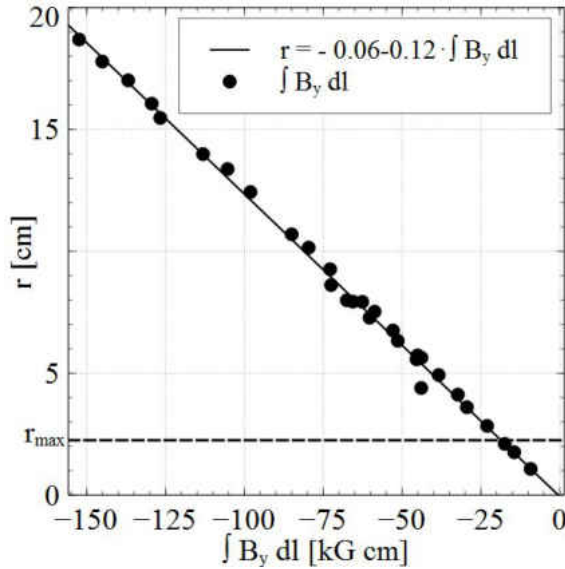
FIG. 73: Beam displacement, r, vs field integral for 30 different combinations of extra iron pieces on the HB yoke and pipes along the beam line. The linear fit determines the maximum field integral for a displacement, $r < r_{max}$. All the simulation results are taken for a 5.5° scattering angle, 11 GeV electron beam and maximum central momentum setting of the spectrometer.

solution robust and fail-safe. If there is any problem with the magnets (power supply trip-off, quench, etc.), the primary beam will still have a displacement at the beam dump window which is less than r_{max}. The beam displacements at the beam dump window from this solution are less than $|r_{max}| = 2.25$ cm at all energies and angles (see Figures 76 and 77).

6.6 SUMMARY

The Opera models and TOSCA solutions presented here have shown themselves to be valuable for simulating the fields of the optics system in the SHMS. The SHMS, as it is being built, has an operational minimum scattering angle of 13° at 11 GeV due to field leakage from the first four magnets. This is 7.5° more than the designed minimum scattering angle of 5.5°. The stray fields steer the unscattered primary beam by as much as 18.2 cm from the center of the beam dump window. This is 15.95 cm farther than the suggested maximum for safe beam operations in Hall C.
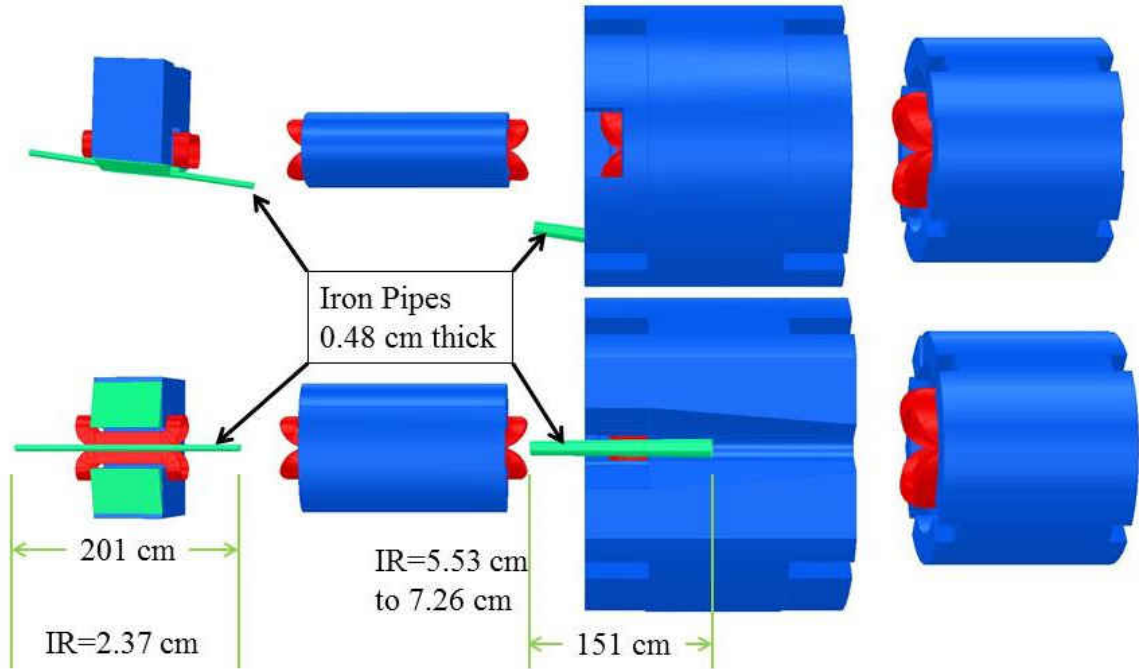
FIG. 74: Top *(top)* and side view (*bottom*) of the first four SHMS magnets showing the iron wedges on the HB yoke and iron pipes around the beam line at HB and Q2.
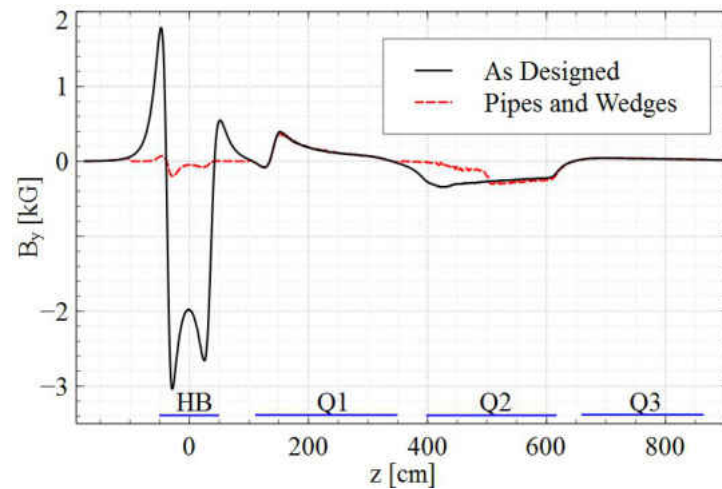
FIG. 75: Vertical component B_y of the simulated field along the beam line from the as-designed SHMS and the SHMS with pipes and wedges at $\theta = 5.5°$ and $11\,\mathrm{GeV}$.
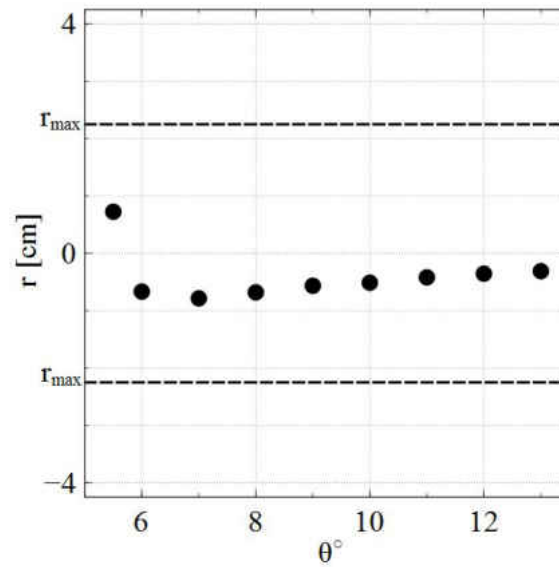
FIG. 76: Beam displacement, r, from the center of the beam dump window vs spectrometer angle when using iron wedges and pipes. All displacements are taken with a beam energy of $E = 11$ GeV and the spectrometer central momentum set to the beam momentum. The dashed lines indicates the maximum allowed displacements, $r_{max} = \pm 2.25$ cm. Everything outside these lines will miss the acceptable region of the beam dump window. Positive r values correspond to beam left displacements. This solution works at all angles studied.
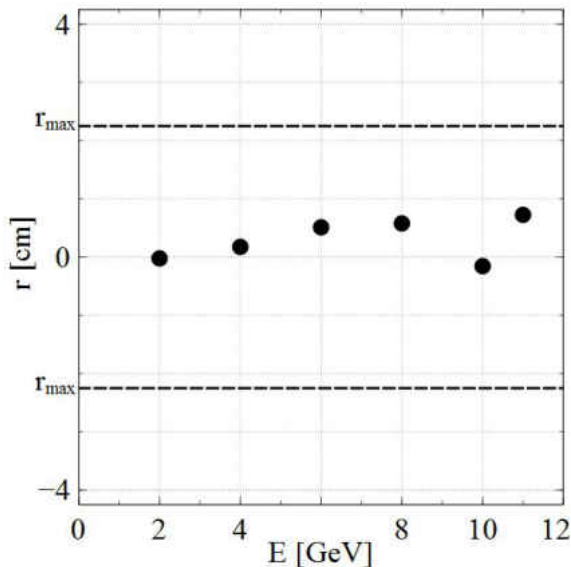
FIG. 77: Beam displacement, r, from the center of the beam dump window vs beam energy with the spectrometer central momentum set to the beam momentum. The displacements are taken with $\theta = 5.5°$. The dashed lines indicate the maximum allowed displacements, $r_{max} = \pm 2.25$ cm. Everything outside these lines will miss the acceptable region of the beam dump window. Positive r values correspond to beam left displacements. This solution works at all energies studied.

The passive solution consisting of pipes and wedges suggested here is a robust and fail-safe solution that works at all angles and energies. For scattering angles of $5.5°$ to $10°$ and a beam energy of 11 GeV, the beam always hits the beam dump window within 1 cm of the center. The same can be said for beam energies with matching spectrometer central momentum from 2 to 11 GeV when the spectrometer is operated at a $5.5°$ scattering angle. At larger spectrometer angles (greater than $13°$) the iron pipes can be removed. Using clam-shell style sheaths instead of pipes would allow for easy removal and replacement.

APPENDIX A

FLUENT UDF CODES

It was important that both the result reporting UDF and the energy deposition UDF shared the exact same raster motion. As discussed in Section 2.2 the raster motion of the beam was due to two air-core magnets that were driven by two triangular waves with frequencies $f_x = 24.96$ kHz and $f_y = 25.92$ kHz. The difference between them is the entire raster pattern frequency and the helicity flip rate, $f_y - f_x = 960$ Hz. To facilitate this, the position of the beam spot was determined through the use of a two parameters, Txfrac and Tyfrac. At any flow time ($tabs$) in the simulation these parameters represent what fraction of a cycle each of the triangular waves have completed.

```
Txfrac = fx*tabs−floor(fx*tabs);
Tyfrac = fy*tabs−floor(fy*tabs);
```

In addition, f was used to store 960 Hz, the frequency of MPS's in the experiment. For the model with 1 μs timesteps, the loop to accomplish the raster motion was

```
if(Tfrac<=0.5) {
    xc = 2.*(a−2.*fwhm)*fx*(tabs−floor(fx*tabs)/fx);
}
else  xc = 2.*(a−2.*fwhm)*fx*((floor(fx*tabs)+1.)/fx−tabs);

if(Tyfrac<=0.5) {
    yc = 2.*(a−2.*fwhm)*fy*(tabs−floor(fy*tabs)/fy);
}
else  yc = 2.*(a−2.*fwhm)*fy*((floor(fy*tabs)+1.)/fy−tabs);
```

Where $fwhm$ is the beam radius of 100 μm. In Fluent UDF's, spatial variables are called with $xx[i]$, where i is 0,1, or 2 representing x, y, z respectively. The above

loop specifies xc and yc, the x and y positions of the center of the beam spot at each timestep. This code worked throughout the length of the model including the aluminum windows. To deposit the energy into the right cells, the following loop was used.

```
if (xc−xx[0]<=fwhm && xx[0]−xc<=fwhm &&
    yc−xx[1]<=fwhm && xx[1]−yc<=fwhm)
    {
            if (C_R(c,t)<75.) {
        source = C_R(c,t)*qvpLH2;
        dS[eqn] = 0;
    }
else{
        source = C_R(c,t)*qvpAl;
        dS[eqn] = 0;
    }
```

Where $qvpLH2$ and $qvpAL$ were the power divided by density in Equation 11, and $C_R(c,t)$ is the density in each cell as reported by Fluent. In this way the power was dependent on density as it would be in the actual target. The "if" statement is meant to separate the aluminum cells from the LH2 cells. In Section 5.2 the power deposition in the target was separated into bulk and window heating. This was accomplished by setting the source term to zero in the above loop for either the LH2 (the "if" statement) or the aluminum (the "else" statement). The data writing UDF worked in exactly the same way except the last loop (power deposition) is replaced by

```
if (xc−x[0]<=fwhm && x[0]−xc<=fwhm &&
    yc−x[1]<=fwhm && x[1]−yc<=fwhm && C_R(c,t)<75.)
                {
                den += C_R(c,t));
                cvol += C_VOLUME(c,t);
```

```
            cnt++;
        }
```

This is from the first code written for this analysis and only includes the most important two values, density and volume. This was later expanded to include velocities of the fluid, pressure, turbulent kinetic energy, turbulent kinetic dissipation, ect. At certain points in the project the Tfrac variables were also written to test the repeatability of the code over many timesteps.

A.0.1 QUADRILATERAL RASTER APPROXIMATION

As in section 4.8, each MPS was approximated by a quadrilateral every 1/28th of an MPS. While the code in the previous section was choosing cells that laid within the radius of the beam from the center of the beam spot, this code worked with a structured mesh, and the number of cells was the same every timestep. The size of each cell was also larger. The first attempt at this used a similar technique to the one above, but the volume reported by Fluent of the area that was of interest in each timestep varied a great deal. In order to tame the erratic behavior, the loop was removed and each timestep was calculated separately. This was done after the model was scaled down by a factor of 10, so the lengths are also scaled down.

```
real  j=.0357142857,l=0.25e-4,  a=4e-4;
if(Tfrac > 0 && Tfrac <= j)
                {           b1=l;
                            b2=a-l;
                            r=4e-6;
                }
if((Tfrac > j && Tfrac <= 2*j) || (Tfrac>1-j))
                {           b1=2*l;
                            b2=a-2*l;
                            r=2e-6;
                }
```

```
if (( Tfrac >
2*j && Tfrac <= 3*j ) || ( Tfrac <= 1-j && Tfrac > 1-2*j ))
                    {           b1=3*l;
                                b2=a-3*l;
                                r=2e-6;
                    }
if (( Tfrac >
3*j && Tfrac <= 4*j ) || ( Tfrac <= 1-2*j && Tfrac >= 1-3*j ))
                    {           b1=4*l;
                                b2=a-4*l;
                                r=5e-6;
                    }
if (( Tfrac >
4*j && Tfrac <= 5*j ) || ( Tfrac <= 1-3*j && Tfrac >= 1-4*j ))
                    {           b1=5*l;
                                b2=a-5*l;
                                r=2e-6;
                    }
if (( Tfrac >
5*j && Tfrac <= 6*j ) || ( Tfrac <= 1-4*j && Tfrac >= 1-5*j ))
                    {           b1=6*l;
                                b2=a-6*l;
                                r=2e-6;
                    }
if (( Tfrac >
6*j && Tfrac <= 7*j ) || ( Tfrac <= 1-5*j && Tfrac >= 1-6*j ))
                    {           b1=7*l;
                                b2=a-7*l;
                                r=2e-6;
```

```
                }
/*****************************/
if ((Tfrac >
7*j && Tfrac <= 8*j) || (Tfrac <= 1-6*j && Tfrac >= 1-7*j))
                {        b1=8*l;
                         b2=a-8*l;
                         r=2e-6;
                }
if ((Tfrac >
8*j && Tfrac <= 9*j) || (Tfrac <= 1-7*j && Tfrac >= 1-8*j))
                {        b1=9*l;
                         b2=a-9*l;
                         r=1e-6;
                }
if ((Tfrac >
9*j && Tfrac <= 10*j) || (Tfrac <= 1-8*j && Tfrac >= 1-9*j))
                {        b1=10*l;
                         b2=a-10*l;
                         r=2e-6;
                }
if ((Tfrac >
10*j && Tfrac <= 11*j) || (Tfrac <= 1-9*j && Tfrac >= 1-10*j))
                {        b1=11*l;
                         b2=a-11*l;
                         r=2e-6;
                }
if ((Tfrac >
11*j && Tfrac <= 12*j) || (Tfrac <= 1-10*j && Tfrac >= 1-11*j))
                {        b1=12*l;
```

```
                                   b2=a−12∗l ;
                                   r=9e −6;

                        }
if ( ( Tfrac >
12∗j && Tfrac <= 13∗j )  ||  ( Tfrac <= 1−11∗j && Tfrac >= 1−12∗j ) )
                        {            b1=13∗l ;
                                     b2=a−13∗l ;
                                     r=5e −6;

                        }
if ( ( Tfrac >
13∗j && Tfrac <= 14∗j )  ||  ( Tfrac <= 1−12∗j && Tfrac >= 1−13∗j ) )
                        {            b1=14∗l ;
                                     b2=a−14∗l ;
                                     r=1e −6;

                        }
if ( Tfrac >   14∗j && Tfrac <= 15∗j )
                        {            b1=15∗l ;
                                     b2=a−15∗l ;
                                     r=2e −6;

                        }
```

First, $j = 1/28$ defines the Tfrac interval in each timestep, and l is the distance between each cell node in the x direction. a is the full raster pattern width (in x). As can be seen in the diagram, this was chosen to facilitate the code to define an x intercept of the lines with negative slope. Since the quadrilaterals run backward halfway through the MPS, each loop is defined for two cases: the first and second halves of the MPS. A better approximation would have been to move the quadrilateral over one beam spot radius during the second half of the MPS in order to more closely mimic the Lissajous pattern. Because of the relatively large structured mesh, this was very difficult to accomplish and after running a few attempts, the asymmetry

changed by much less than one percent, so the motion of the quadrilaterals was made to just reverse halfway through the MPS. At the beginning and end of the MPS the loops were not shared with the reversed motion making it $28/2 + 1 = 15$ loops. Had the beginning and end loops been combined, the beam would have stayed in the same place for two consecutive timesteps, which would have been unacceptable. The
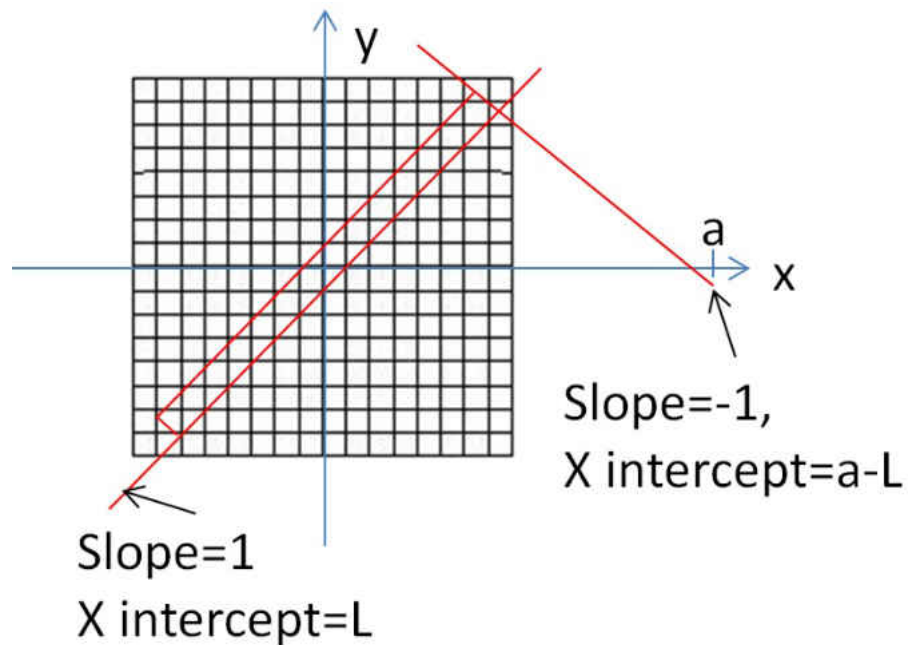
FIG. 78: Definition of lines in the quadrilateral approximation. Please refer to the code. The red lines are the center of the quadrilateral for the first timestep, $0 < Tfrac <= j$. Two of the lines have been extended to show the x-intercepts as a function of a and l.

quadrilaterals are composed of four lines, all with slopes of either ± 1. The lines are defined by this slope and the x-intercept. Luckily, the UDF was hooked to the raster volume cell zone, so any overflowing from the 4×4 mm square was impossible. The r variable represents the beam spot radius, but was fine tuned for each timestep to assure that it was only catching the cells of interest. This was done by having Fluent report both the number of cells and the volume for each timestep.

APPENDIX B

ASYMMETRY WIDTH CODE

The same basic structure was used to find the asymmetry widths for the simulation results and the Qweak data. For the Qweak data, some of the runs needed to be replayed from tape. This was accomplished by a script written with the help of Paul King. After the ROOT files were created, the following ROOT code was run. This will be a condensed and annotated version of the full code only showing the key elements. The branch of the ROOT file that contains the detector data was read with

```
ttree->Add(path.str().c_str());
TBranch *branch=((TChain*)ttree)->GetBranch("qwk_mdallbars");
```

In this example, the branch is called mdallbars, which stands for "all of the main detectors." After this the number of entries, N, was found and the data stored in a vector called *Dvector*

```
N=(Int_t)ttree->GetEntries();
 for  (Int_t  a=0;a<=N;a++)
        {
        ttree->GetEntry(a);
        D =  branch->GetLeaf("hw_sum")->GetValue();
        Dvector.push_back(D);
        }
```

Now that the data is stored in a vector the asymmetry calculations can be made. Since the asymmetries will be calculated for ten different pattern sizes, a loop was preferable to ten different functionals. To make this "pattern loop", first a vector was initialized with ten entries representing the number of MPS's in a pattern.

Fvector [0]=4;

Fvector [1]=8;

Fvector [2]=16;

Fvector [3]=20;

Fvector [4]=24;

Fvector [5]=32;

Fvector [6]=40;

Fvector [7]=48;

Fvector [8]=64;

Fvector [9]=128;

The quartet pattern used in the Qweak experiment has 4 MPS's for each asymmetry calculation. Using the same nomenclature from above, this means that 960 Hz has 4 MPS's and 15 Hz has 64 MPS's per pattern. The complete set of frequencies can be seen in Table 6 in Chapter 3. The value of the calculated asymmetries are stored in a ten entry vector call $ASYM$ The asymmetry equation is

$$A = \frac{\sigma_+ - \sigma_-}{\sigma_+ + \sigma_-} \tag{70}$$

In terms of detector data which is recorded once every MPS and is now stored in the vector Dv, this translates to

$$A = \frac{(Dv[0] + Dv[4]) - (Dv[2] + Dv[3])}{\sum_{i=0}^{3} Dv[i]} \tag{71}$$

for the 960 Hz quartet pattern (Fvector[0]). For the next lower frequency, 480 Hz (Fvector[1]),

$$A = \frac{(Dv[0] + Dv[1] + Dv[6] + Dv[7]) - (Dv[2] + Dv[3] + Dv[4] + Dv[5])}{\sum_{i=0}^{7} Dv[i]} \tag{72}$$

By noticing that A for every frequency breaks down the pattern into two groups, the
"+" entries and the "-" entries, the equation for the loop becomes

$$A = \frac{dp - dm}{dp + dm} \tag{73}$$

where dp and dm are the sum of all the plus entries and sum of all the minus entries,
respectively, in the detector data for one pattern. At 960 Hz, (Fvector[0]=4), both
of the sums dm and dp will have two terms each. At 480 Hz, (Fvector[1]=8), each
one will have 4 terms, ect. dm and dp are then broken down into sums of pairs. For
quartets, $dp = D[0] + D[4]$, for 480 Hz, $dp = (D[0] + D[7]) + (D[1] + D[6])$. By adding
up entries this way a loop could be constructed by index in the following manner.

```
for (m=Fvector[i]; m<=N m=m+Fvector[i])
                    {


Double_t Dp1 = 0;
Double_t Dm1 = 0;
for(k=0; k<Fvector[i] /4; k++)
                             {
Dp1 += MPS[m-Fvector[i]/4+k] + MPS[m-Fvector[i]+k];
Dm1 += MPS[m-Fvector[i]/2-1-k] + MPS[m-Fvector[i]/2+k];
                             }
A1=((Dp1-Dm1)/(Dp1+Dm1))*1e6;
ASYM1.push_back(A1);
                    }
```

This loop fills the vector ASYM with the value the asymmetry calculation for each
pattern. The first loop moves the index, j, to the end of the first pattern, and once
the inside loop is completed, it adds one value to the ASYM vector and moves j to
the end of the next pattern. This continues until j reaches N, the size of the D vector.
Notice that dm and dp are initialized before the inside loop starts and that the "+="
equality statement in the inside loop continues to sum the pairs of D entries until the

entire pattern has been used ($k < Fvector[i]/2$), at which point the loop is exited and dm and dp are initialized for the next pattern. This results in a ASYM vector that has $N/Fvector[i]$ entries. These values are then used to fill a histogram and the RMS extracted

```
RMS=h1->GetRMS();
```

The version of the two asymmetry loops above is the one used before the additional nesting inside a loop over the number of MPS's per pattern, Fvector[i]. Once that loop was written the code would return back ten histograms and a plot of the RMS of the histograms (in ppm) as a function of frequency. This vector was formed at the end of the i loop as

```
RMSvector.push_back(RMS);
```

These ten value were plotted against $960 * 2/Fvector[i]$. The only difference between the code used on the Qweak data and the code used on the simulation results is MPS averaging. The simulation produced density twenty eight times every MPS. It would seem straight forward to average every twenty eight entries and call that an average MPS value. Since replicating the raster motion was so important, great care was taken to make sure that the Lissajous pattern was completed every MPS and that there was no drift in what point in time the averaging was taking place. The beginning and end of each MPS were therefore marked by reading the variable from Appendix A. Because the result reporting UDF and the heat deposition UDF both operated together, this was assurance that each MPS contained one full Lissajous pattern and allowed the code to report an error if there were more or less than twenty eight time steps for each one. By filling the vector D with the MPS averaged density simulation results the loops above are the same for both Qweak and Fluent. The double difference asymmetries for the BCM's were found in much the same way. The calculation had to be run separately to two different BCM's and then subtracted. The loop follows.

```
for(m=Fvector[i]; m<=N; m=m+Fvector[i])
  {
```

```
Float_t DpS = 0;  Float_t DmS = 0;
Float_t DpE = 0;  Float_t DmE = 0;
 for (n=0; n<Fvector[i]  /4; n++)
  {
   DpS += DSvector[m-Fvector[i]/4+n] +
          DSvector[m-Fvector[i]+n];
   DmS += DSvector[m-Fvector[i]/2-1-n] +
          DSvector[m-Fvector[i]/2+n];


   DpE += DEvector[m-Fvector[i]/4+n] +
          DEvector[m-Fvector[i]+n];
   DmE += DEvector[m-Fvector[i]/2-1-n] +
          DEvector[m-Fvector[i]/2+n];
  }
      A=(DpS-DmS)/(DpS+DmS);
      A1=(DpE-DmE)/(DpE+DmE);
      A2=A-A1;
      ASYMs.push_back(A);
      ASYMe.push_back(A1);
      ASYMdd.push_back(A2);
  }
```

The first BCM asymmetry uses DpS for the "+" entries, and DmS for the "-" entries. The second BCM entries are likewise called, DpE and DmE. A and $A1$ are the asymmetry calculations for each BCM and $A2$ is the double difference value. For completeness, the asymmetries from both BCM's was plotted separately and as the double difference. See Figure B. The contribution due to counting statistics was found by using Equation 7 in Chapter 3.
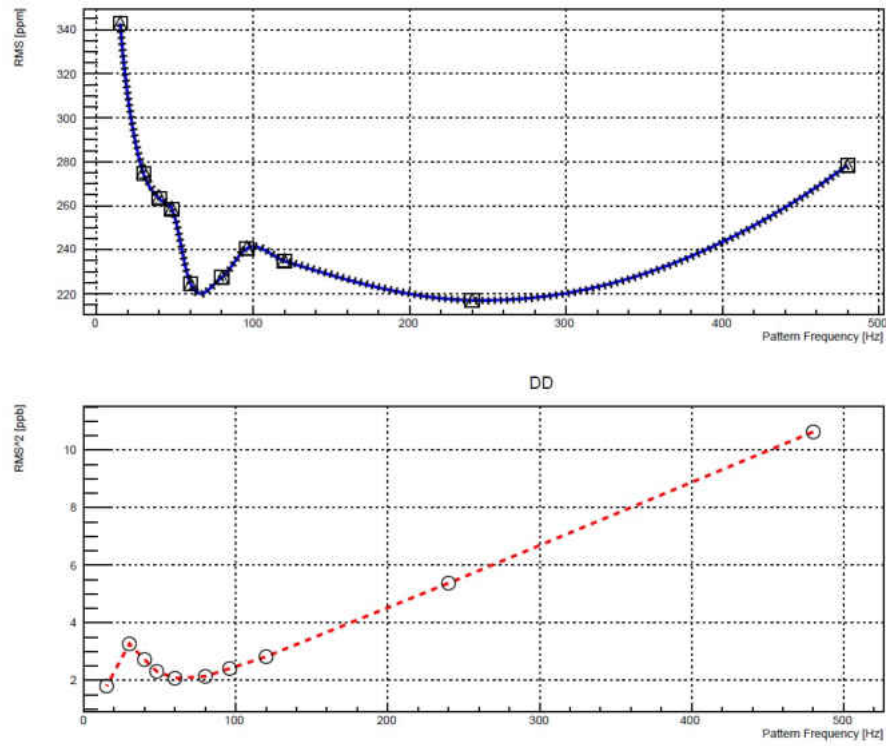
```
for ( i =0; i <10; i++)
    {
```

FIG. 79: Double difference frequency plots for BCM's one and two for run 11740. The top plot is both asymmetries separately and the bottom plot is the difference between the two(double difference)

$$\text{CS=Current} * \text{Fvector} [\,i\,]/3.3842929355197\,e-5;$$

$$\text{CSvector.push\_back}(1/\text{sqrt}(\text{CS}));$$

$$\}$$

Here, CS is σ_0^{-2}. While filling the vector $CSvector$ the square root was taken and the reciprocal value, σ_0 (ppm) was pushed into the vector, $CSvector$. These three values, σ_0, σ_{bcm} and σ_m were first found through separate codes, and later combined into one combination file. This code uses

```
for  (c=0;c<10;c++)
  {
    x[c]  =  960*2/Fvector[c];
    y[c]=  sqrt(RMSvector1[c]*RMSvector1[c]-
           CSvector[c]*CSvector[c]-ASYMdd[c]*ASYMdd[c]/2)*1e6;
  }
```

to find the frequency values from the pattern size, $x[c]$ and σ_{tgt} which is defined as

$$\sigma_{tgt} = \sqrt{\sigma_m^2 - \sigma_0^2 - \sigma_{bcm}^2} \qquad (74)$$

σ_{tgt} here is the vector $y[c]$. The resulting plot of boiling noise is in parts per million.

APPENDIX C

QWEAK RUNS USED

Run #	date	raster[cm] xXy	current[uA]	energy[MeV]	Target	Pump frequency[Hz]	#segments	Notes
11740	4/29/2011	4X4	166	1162.06	H2	28	9	
11750	4/30/2011	4X4	169	1162.06	H2	30	3	only 1 good segment
11805	5/2/2011	4X4	168	1162.06	H2	29.5	1	Boiling studies 11805 to 11822
11810	5/2/2011	4X4	166	1162.06	H2	29.5	1	Boiling studies 11805 to 11822
11811	5/2/2011	4X4	166	1162.06	H2	29.5	1	Boiling studies 11805 to 11822
11815	5/2/2011	5X3	168.5	1162.06	H2	29.5	1	15.3 hz- In analysis it lists raster as 3X3
11816	5/2/2011	4X4	168.3	1162.06	H2	29.5	1	
11817	5/2/2011	4X4	168.8	1162.06	H2	29.5	1	
11820	5/2/2011	3X5	169	1162.06	H2	29.5	1	
11822	5/2/2011	4X4	168.9	1163.06	H2	29.5	1	
11990	5/7/2011	4.5X4.5	165	1162.06	H2	28	10	
12080	5/11/2011	4X4	179.4	1162.06	H2	30	9	
12095	5/11/2011	4X4	168.1	1162.06	H2	30	3	Pump speed study
12160	5/13/2011	4X4	177.3	1162.06	H2	29	11	
6894	11/12/2010	3X3	5	1162.06	HOME=OutOfBeam	30.5	8	
7160	11/16/2010	3X3	0	1162.06	H2	?	10	Pedestal
8370	12/20/2010	4X4	0	1162.06	HOME=OutOfBeam	?	16	BCM calibration
8870	1/12/2011	3.5X3.5	0	1162.06	H2	18-27	1	MD Pedestal Test
9273	1/20/2011	3.5X3.5	0	1162.06	H2	29	7	BCM calibration
17245	3/30/2012	4X4	176.3	1162.06	H2	29-30	14	
17250	3/31/2012	4X4	179	1162.06	H2	29	14	
18435	5/3/2012	4X4	175.8	1162.06	H2	30	1	
18440	5/4/2012	4X4	176.9	1162.06	H2	29	14	
18640	5/8/2012	4X4	58.9	1157.58	DS-4%-Aluminum	29.5	1	
18790	5/13/2012	4X4	110.3	1157.53	US-2%-Aluminum	30	14	
6846	40492	3X3	0	1162.06	H2	28.5	13	BCM calibration
6894	11/12/2010	3X3	0	1162.06	HOME=OutOfBeam	30.5	2	

FIG. 80: List of Qweak runs studied.

REFERENCES

[1] E. Rutherford. ""The Scattering of α and β rays by Matter and the Structure of the Atom"". In: *Philos. Mag.* 6 (1911).

[2] Jefferson Lab Visitor's Center. *History and Photos.* [Online; `http://www.jlab.org/visitors/history/`; accessed 04-27-2014].

[3] Erdogan Madenci and Ibrahim Guven. *The Finite Element Method and Applications in Engineering Using ANSYS.* Springer, 2015.

[4] Erwin Stein. *The History of Theoretical, Material and Computational Mechanics - Mathematics Meets Mechanics and Engineering.* Springer-Verlag Berlin Heidelberg, 2014.

[5] Lewis Fry Richardson. *Weather Prediction by Numerical Process.* Cambridge University Press, 2007.

[6] R. Courant et al. "On the Partial Difference Equations of Mathematical Physics ". In: *IBM Journal of Research and Development* 11 (2 1967), pp. 215–234.

[7] D. N. DE G. Allen and R. V.Southwell. "Relaxation Methods Applied to Determine the Motion, in Two Dimensions, of a Viscous Fluid Past a Fixed Cylinder". In: *The Quarterly Journal of Mechanics and Applied Mathematics* 8.2 (1955), pp. 129–145. DOI: `10.1093/qjmam/8.2.129`. eprint: `/oup/backfile/content_public/journal/qjmam/8/2/10.1093/qjmam/8.2.129/2/8-2-129.pdf`. URL: `+http://dx.doi.org/10.1093/qjmam/8.2.129`.

[8] M. Kumar and P. Philominathan. "Bringing out Fluids Experiments from Laboratory to In Silico – A Journey of Hundred Years". In: *American Journal of Computational Mathematics* 1.4 (2011), pp. 271–280. DOI: `10.4236/ajcm.2011.14033`.

[9] Joel H. Ferziger. *Computational methods for fluid dynamics.* Springer, 1996.

[10] Pradip Niyogi. *Introduction to Computational Fluid Dynamics.* Pearson Education India, 2005.

[11] ANSYS, Inc. *Acquisition History*. [Online; `http://www.http://investors.ansys.com/company-information/acquisition-history`; accessed 03-11-2015].

[12] Roland W. Lewis, Perumal Nithiarasu, and Kankanhalli N. Seetharamur. *Fundamentals of the Finite Element Method for Heat and Fluid Flow*. Wiley, 2004.

[13] Frederic Magoules. *Computational Fluid Dynamics*. Chapman and Hall/CRC, 2011.

[14] D. Androic and Armstrong et al. "First Determination of the Weak Charge of the Proton". In: *Phys. Rev. Lett.* 111 (14 2013), p. 141803. DOI: `10.1103/PhysRevLett.111.141803`. URL: `https://link.aps.org/doi/10.1103/PhysRevLett.111.141803`.

[15] et al. R.D. Carlini. "The Qweak Experiment: A Search for New Physics at the TeV Scale via a Measurement of the Proton's Weak Charge". In: *JLAB-PHY-12-1478* (2007). arXiv:1202.1255.

[16] T. Allison and M. Anderson et al. "The Qweak experimental apparatus". In: *Nuclear Instruments and Methods in Physics Research Section A: Accelerators, Spectrometers, Detectors and Associated Equipment* 781 (2015), pp. 105 –133. ISSN: 0168-9002. DOI: `http://dx.doi.org/10.1016/j.nima.2015.01.023`. URL: `http://www.sciencedirect.com/science/article/pii/S0168900215000509`.

[17] Silviu Covrig Dusa. "High Density Targets for External Beams". Intense Electron Beams Workshop. 2015. URL: `https://indico.classe.cornell.edu/event/38/session/0/contribution/6/material/slides/1.pdf`.

[18] Christoph W. Leemann, David R. Douglas, and Geoffrey A. Krafft. "The Continuous Electron Beam Accelerator Facility: CEBAF at the Jefferson Laboratory". In: *Annu. Rev. Nucl. Part. Sci.* 51 (2001), pp. 413–450.

[19]   J. C. Denard, A. Saha, and G. Laveissiere. "High accuracy beam current monitor system for CEBAF'S experimental Hall A". In: *PACS2001. Proceedings of the 2001 Particle Accelerator Conference (Cat. No.01CH37268)*. Vol. 3. 2001, 2326–2328 vol.3. DOI: 10.1109/PAC.2001.987367.

[20]   Katherine E. Myers. "The First Determination of the Proton's Weak Charge Through Parity-Violating Asymmetry Measurements in Elastic e + p and e + Al Scattering". PhD thesis. The George Washington University, 2012.

[21]   C. Yan, N. Sinkine, and R. Wojcikt. "Linear beam raster for cryogenic targets". In: *Nuclear Instruments and Methods in Physics Research A.* 539 (2005), pp. 1–15.

[22]   Greg Smith, Silviu Covrig, and Jim Dunne. "Qweak Liquid Hydrogen Target: Preliminary Design & Safety Document". Internal Document. 2009.

[23]   Adesh Subedi. "Determination of the weak charge of the proton through parity violating asymmetry measurements in the elastic e+p scattering". PhD thesis. Mississippi State University, 2014.

[24]   National Institute of Standards and Technology (NIST). *estar*. [https://physics.nist.gov/PhysRefData/Star/Text/ESTAR.html; accessed 10-27-2014].

[25]   Silviu Covrig Dusa. "High Power Cryogenic Targets for PVES". pavi14. 2014. URL: http://pavi14.syr.edu/Talks/Tuesday/covrig_pavi14.pdf.

[26]   Massoud Kaviany. *Principles of Heat Transfer*. Wiley, 2002.

[27]   CERN. *ROOT Data Analysis Framework*. [https://root.cern.ch/; accessed 7-01-2017].

[28]   JLAB. *Hall C Logbook*. [https://hallcweb.jlab.org/hclog/; accessed 11-3-2015].

[29]   ANSYS Inc. *ANSYS-Fluent*. [http://www.ansys.com/Products/Fluids/ANSYS-Fluent/; accessed 7-10-2017].

[30]   ANSYS Inc. "ANSYS Fluent Theory Guide". Release 15.0. 2013.

[31] ANSYS Customer Support. *private communication*. June 2016.

[32] Mikko Manninen and Veikko Taivassalo. "On the mixture model for multiphase flow". In: *VTT Publications* 288 (1996).

[33] ODU. *High-Performance-Computing.* [https://www.odu.edu/facultystaff/research/resources/computing/high-performance-computing/; accessed 7-13-2017].

[34] American Institute of Aeronautics and Astronautics. "Guide for the Verification and Validation of Computational Fluid Dynamics Simulations". https://arc.aiaa.org/doi/book/10.2514/4.472855. 2013.

[35] L. M. Ward and P. E Greenwood. "1/f noise". In: *Scholarpedia* 2.12 (2007). revision #90924, p. 1537. DOI: `10.4249/scholarpedia.1537`.

[36] P.D. Brindza et al. "Design of the Super Conducting Super High Momentum Spectrometer (SHMS) for the JLAB 12 GeV Upgrade". In: *Applied Superconductivity, IEEE Transactions on* 19 (3 2009), pp. 1294–1297.

[37] C.K. Sinclair et al. "High Power Electron Beam Dumps At CEBAF". In: *Proceedings of the 1997 Particle Accelerator Conference, (Vancouver, 1997) IEEE* (1997), p. 3761.

[38] Roger Carlini. "SHMS Fringe Fields". In: *Hall C Summer Workshop* (August 2013). [Online; `http://www.jlab.org/Hall-C/talks/08_15_13/carlini.pdf`; accessed 05-05-2014].

[39] Cobham Antenna Systems Vector Fields Simulation Software. *Opera Simulation Software*. [Online; `http://www.vectorfields.com`; accessed 04-27-2014].

[40] Jay Benesch. *private communication*. March 2014.

[41] J. Simkin and C.W. Trowbridge. "Three-dimensional Nonlinear Electromagnetic Field Computations Using Scalar Potentials". In: *IEE Proc.* 127 Pt. B.6 (1980), pp. 368–374.

[42] Buddhini P. Waidyawansa et al. "GEANT4 Simulations of the Hall C Super High Momentum Spectrometer Fringe Field Effects". In: (to be published).

VITA

Michael H. Moore

Department of physics

Old Dominion University

Norfolk, VA 23529

EXPERIENCE

- *Graduate Research Assistant. Center for Accelerator Science, Old Dominion University* (2010-2013)- Simulated niobium superconducting radio frequency cavities for the proposed high-intensity proton accelerator at Fermi Lab with Microwave Studio.

- *Lab Assistant, Experimental Nuclear and Particle Physics Group, Old Dominion University* (2007-2010)- Constructed two clean rooms, fabricated and tested prototype drift chambers.

- *Intern. Superconducting Magnet Group, Lawrence Berkeley National Lab* (2004)- Developed simulations for radiation shielding for a human mission to Mars. Shielding consisted of a confined magnetic field generated by superconducting magnets.

SELECTED PUBLICATIONS

- M.H. Moore, B.P. Waidyawansa, S. Covrig, R. Carlini and J. Benesch. Primary beam steering due to field leakage from superconducting SHMS magnets. Journal of Instrumentation, Volume 9, November 2014.

- Senior Thesis at Old Dominion University: Michael Moore, Lawrence Weinstein. Relationship Between Magnetic Flux Geometry and Levitation Properties of Field Cooled YBCO, December 2009.

Typeset using LaTeX.